NMR-based structural biology of microtubules and of microtubule-associated proteins

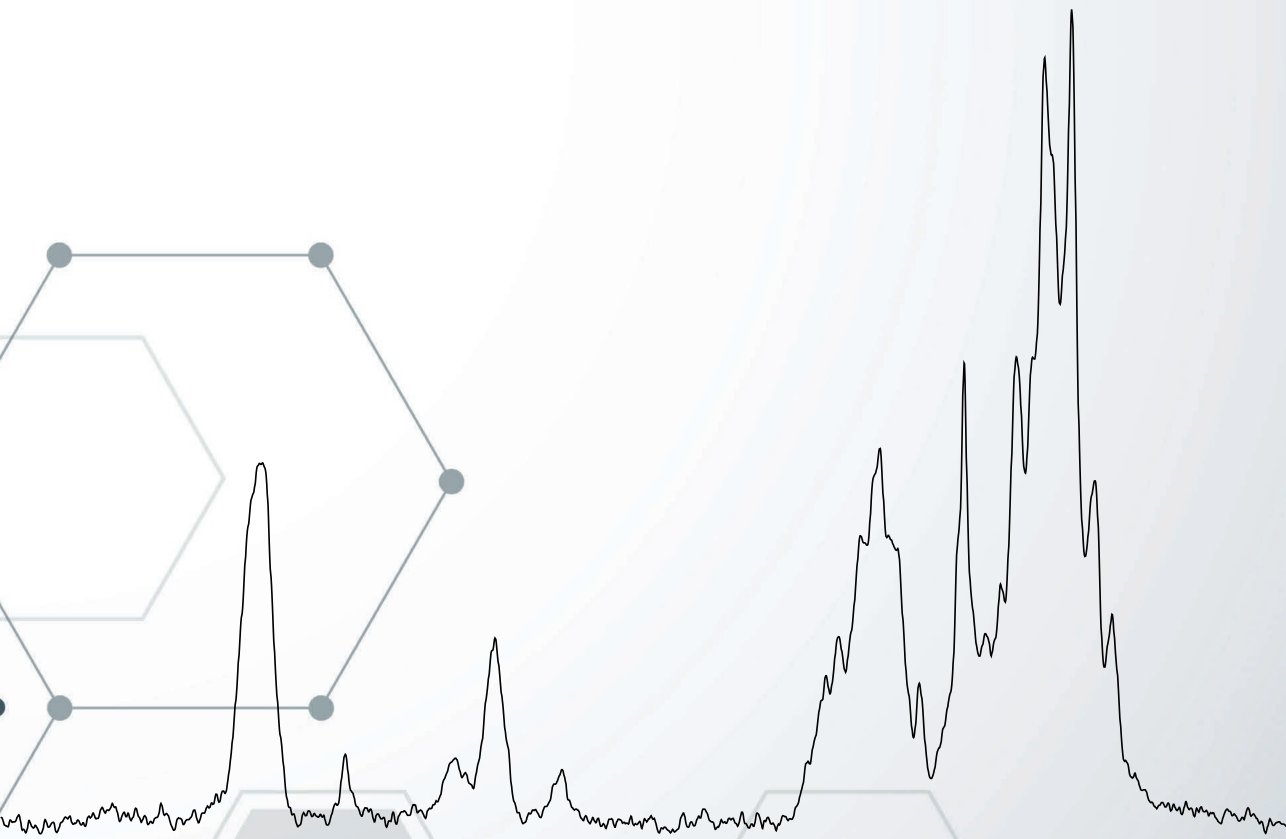

Yanzhang Luo

NMR-based structural biology of microtubules and of microtubule-associated proteins

Yanzhang Luo

ISBN 978-94-6380-502-5

Doctoral Thesis
NMR-based structural biology of microtubules and of microtubule-associated proteins

Yanzhang Luo
NMR Spectroscopy
Bijvoet Center for Biomolecular Research, Faculty of Chemistry,
Utrecht University, the Netherlands
October 2019

Cover and lay-out design: Yanzhang Luo and ProefschriftMaken
Printed in the Netherlands by ProefschriftMaken | www.proefschriftmaken.nl

NMR-based structural biology of microtubules and of microtubule-associated proteins

NMR-gebaseerde structurele biologie van microtubuli en microtubulus-geassocieerde eiwitten

(met een samenvatting in het Nederlands)

Proefschrift

ter verkrijging van de graad van doctor aan de Universiteit Utrecht op gezag van de rector magnificus, prof.dr. H.R.B.M. Kummeling, ingevolge het besluit van het college voor promoties in het openbaar te verdedigen op maandag 14 oktober 2019 des middags te 4.15 uur

door

Yanzhang Luo

geboren op 30 oktober 1990 te Guangdong, China

Promotor:
Prof. dr. M. Baldus
Copromotor:
Dr. G.E. Folkers

Table of Contents

CHAPTER 1

1

General Introduction

Nuclear magnetic resonance (NMR) and solid-state NMR (ssNMR)

For several decades, NMR has developed into one of the major analytical and structural tools in chemistry, structural biology as well as medical and material science. NMR is a spectroscopic technique that allows to detect the local chemical environments of nuclei, provided that these nuclei have a magnetic spin. While nuclei that contain an even number of protons and an even number of neutrons are NMR inactive (for example, ^{12}C, ^{16}O and ^{32}S), many isotopes of chemical elements can be used for NMR analysis. For example, ^{1}H, ^{2}H, ^{13}C, ^{15}N, ^{31}P, ^{19}F are commonly used in biological NMR. Importantly, NMR can provide atomic information of molecules and is widely used in studying molecular structures, dynamics and molecular interactions at atomic level. In the case of proteins, solution-state NMR can be employed to study relatively small proteins (up to ~35 kDa) that undergo rapid Brownian motion in solution. The fast tumbling averages out anisotropic NMR effects and results in high-resolution NMR spectra. Recent developments in tailored isotope labeling schemes allow extending solution-state NMR to capture information of flexible side chains from certain residues in larger biomolecules and complexes[1], while the remaining segments of such systems remain largely invisible. Solid-state NMR (ssNMR), on the other hand, can overcome this size limitation and is a suitable method to study large systems that do not tumble fast or are largely immobile on the NMR time scale. For example, ssNMR has been intensively used to conduct structural and dynamics studies on complex protein aggregates such as amyloid fibrils[2], as well as membrane protein (complexes) in lipid bilayers and even in the native membranes[3] at atomic resolution. In addition, ssNMR has been employed to study protein-nucleosome interactions[4], protein-cytoskeleton interactions[5] and dynamic protein assemblies [6].

In spite of these advancements, a major challenge in ssNMR remains the low spectroscopic sensitivity, which in the case of spin ½ nuclei is determined by the energy gap between the two (up and down) spin states in an external magnetic field according to the Boltzmann's equation:

$$\frac{N_{upper}}{N_{lower}} = e^{-\Delta E/kT} \qquad \text{eq. 1}$$

In eq. 1, ΔE represents the energy difference between the spin up and spin down states of spin ½ nuclei. It is proportional to the gyromagnetic ratio that is given by the ratio of the magnetic moment to the spin angular momentum of the nuclei and the strength of the applied magnetic field. The Gyromagnetic ratio γ_n is determined by:

$$\gamma_n = \frac{e}{2m_p} g_n = g_n \mu_N / \hbar \qquad \text{eq. 2}$$

where μ_N is the nuclear magneton, g_n is the g-factor of the nucleus and $\hbar$ is the Planck constant. Lastly, N_{upper} and N_{lower} in eq. 1 reflect the populations of nuclei in both states, k is the Boltzmann constant and T is the temperature.

Another critical aspect in performing ssNMR experiments refers to the spectral resolution that can depend on the macroscopic state of the sample under study. As mentioned before, the samples used in ssNMR do not undergo free tumbling that is seen for molecules in solution. As a result, orientation dependent interactions, including the chemical shift anisotropy (CSA) and magnetic dipole-dipole interactions are not averaged out, thereby leading to anisotropic line shapes that lower the spectral resolution. The CSA line broadening is caused by the asymmetry of the electronic environment around the nuclei. Magnetic dipole-dipole interactions, also called as dipolar couplings, occur between two homonuclear or heteronuclear spins that are located close to each other in space. As a result, the two spins are affected by their mutual magnetic field and the effective magnetic fields they experience are determined by their relative positions. The strength of the dipole-dipole interactions between the magnetic moments of two spins ($\overrightarrow{\mu_1}$ and $\overrightarrow{\mu_2}$) with a distance of r_{12} is given by:

$$E = \left(\frac{\mu_0}{4\pi}\right) (\overrightarrow{\mu_1} \cdot \overrightarrow{\mu_2}) r_{12}^{-3} (1 - 3\cos^2\theta) \qquad \text{eq. 3}$$

with $\vec{\mu} = \gamma \hbar I$, and θ is the angle between the distance vector r_{12} and the static magnetic field (Figure 1).

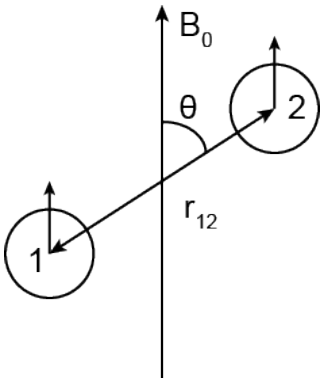

Figure 1. Schematic representation of dipolar coupling between two spins 1 and 2 with distance of r_{12} at the angle θ between r_{12} and the static magnetic field B_0.

Eq. 3 can be reformulated to the so-called dipolar alphabet:

$$H_D = \frac{\mu_0 \gamma_1 \gamma_2 h^2}{16\pi^3 r^3}(A + B + C + D + E + F)$$

where

$$A = I_{1z}I_{2z}(3\cos^2\theta - 1) \text{ and } B = \frac{1}{4}[I_1^+ I_2^- + I_1^- I_2^+](3\cos^2\theta - 1)$$

Normally, only the terms A and B need to be considered for dipolar couplings. This results in the heteronuclear H_D^{IS} and homonuclear H_D^{II} dipolar coupling as below:

$$H_D^{IS} = \frac{\mu_0 \gamma_1 \gamma_2 h^2}{16\pi^3 r^3}(3\cos^2\theta - 1)I_{1z}I_{2z}$$

and

$$H_D^{II} = \frac{1}{2}\frac{\mu_0 \gamma_1 \gamma_2 h^2}{16\pi^3 r^3}(3\cos^2\theta - 1)(3I_{1z}I_{2z} - I_1 \cdot I_2)$$

Similar orientation-dependent equations can be derived for the CSA interaction. Taken together, both CSA and dipolar interactions are dependent on the orientation of each molecule in the static magnetic field and all possible molecular orientations contribute to the ssNMR spectra, resulting in so called powder patterns in the case of a static ssNMR experiment (Figure 2, panel a).

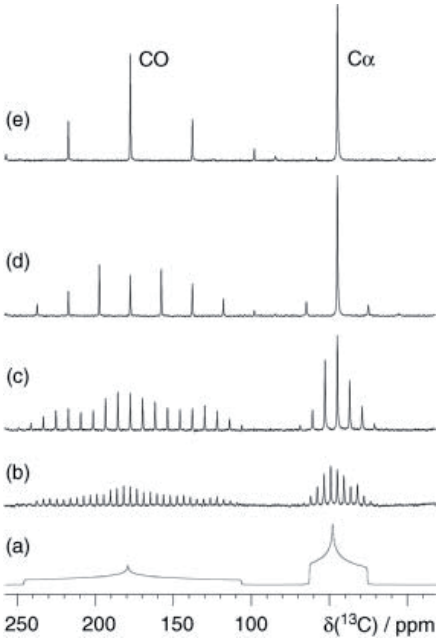

Figure 2. Simulated ^{13}C spectra of a glycine powder sample (a) without MAS and with MAS rates of (b) 1 kHz, (c) 2 kHz, (d) 5 kHz and (e) 10 kHz. Figure taken from ref[9].

In order to improve the spectral resolution, magic angle spinning (MAS)[7] is commonly used. It can be shown that rotating the sample at an angle of 54.74°[7] with respect to the static magnetic field largely averages out CSA and dipolar interactions leading to high-resolution spectra that mimic the molecular tumbling in liquids (Figure 2). Characteristic spinning sidebands separated by multiples of the MAS rate appear in the case of MAS rates (Figure 2) only partially averaged out these anisotropic interactions. Using high-speed MAS rotors, it is today possible to mostly average out ^{13}C-^{13}C and ^{13}C-^{1}H dipolar couplings (approximately 7.5 kHz and 30 kHz respectively). Under such conditions, detection in ssNMR is mostly performed on ^{13}C (in some cases, ^{15}N or ^{31}P) nuclei and decoupling of the ^{1}H-spins is applied during evolution and detection to improve spectral resolution. However, averaging out the strong ^{1}H-^{1}H couplings (~120 kHz) is more difficult and has only been possible recently with newly designed NMR probeheads and MAS rotors. With these advancements in hardware, it is possible to spin the samples between 50-126 kHz to better average ^{1}H-^{1}H couplings and even allow obtaining high-resolution, ^{1}H-detected

spectra[8] (Figure 3). Since the NMR sensitivity correlates to the gyromagnetic ratio as shown in eq. 2, using ^{1}H ssNMR also significantly improves ssNMR sensitivity and will be discussed further below.

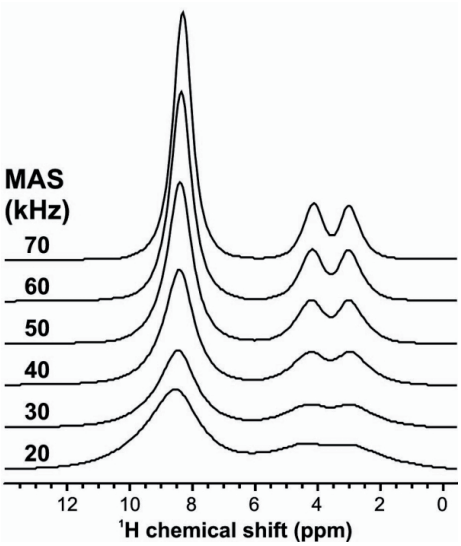

Figure 3. ^{1}H MAS spectra of glycine powder at different MAS rates. The spectral resolution is improved with increase of MAS rate. Figure taken from ref[10].

Improving signal sensitivity in ssNMR

As shown in eq. 1, the relatively low signal sensitivity in ssNMR is related in part to detection of ^{13}C (or ^{15}N, ^{31}P), which exhibit a low gyromagnetic ratio. In addition, studying specific components within large protein complexes reduces the sample quantity of the protein to be studied. For example, in this thesis proteins are examined that bind to microtubules, which are protein polymers that consist of 110 kDa tubulin heterodimers and are much larger in size compared to the binding partners (typically 14-16 kDa). Therefore the ssNMR sample container is mostly occupied by microtubules and carries only a small fraction of the isotope-labeled microtubule-binding protein of interest.

Cross Polarization

In ssNMR, cross polarization (CP)[11] is a general method to increase signal sensitivity for nuclei with low gyromagnetic ratios (Figure 4). During cross

polarization, magnetization is transferred from abundant spins *I* (mostly ^{1}H) via heteronuclear dipolar couplings to the spins *S* that are close in space (^{13}C, ^{15}N or ^{31}P). With cross polarization, the magnetization of the spin *S* with low gyromagnetic ratio is increased by γ_I/γ_S (i.e., for ^{13}C, $\gamma_I/\gamma_S = 4$; for ^{15}N, $\gamma_I/\gamma_S = 10$). In addition, proton nuclei from which the polarization originates in general exhibit much shorter T_1 relaxation times than ^{13}C or ^{15}N. Therefore, the recycle delay of the experiment can typically be faster and the whole experimental time period of the measurement can be shortened.

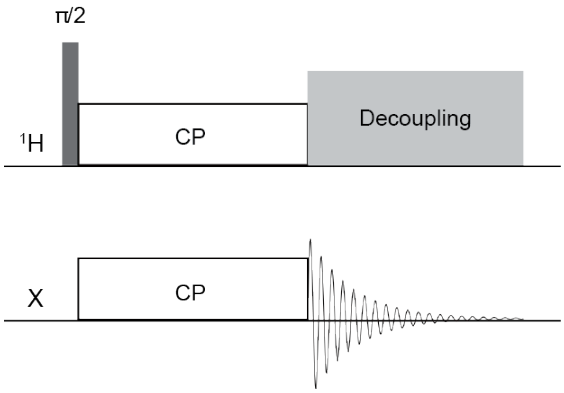

Figure 4. Schematic representation of a cross polarization experiment. During CP the magnetization is transferred from ^{1}H to nuclei X (i.e. ^{13}C or ^{15}N). Note that this experiment can be also used to enable magnetization transfer from spin X to another spin Y.

Proton detection

As indicated in eq. 1, detection of ^{1}H spins is in principle optimal for NMR sensitivity. In the past, such detection schemes where hampered in ssNMR by the dominant influence of ^{1}H-^{1}H dipolar couplings. With the advent of ultra-fast MAS where samples are spun at MAS rates of 50-110 KHz, averaging of ^{1}H-^{1}H couplings is greatly improved and ^{1}H-detection becomes possible in ssNMR as in solution-state NMR where ^{1}H-^{1}H couplings are averaged out by fast tumbling of molecules. The gyromagnetic ratio of ^{1}H is 4 times and 10 times higher than the ones for ^{13}C and ^{15}N respectively. Therefore, compared to general ^{13}C or ^{15}N detection in ssNMR, ^{1}H detection can provide a significant gain in sensitivity. Spectral resolution and sensitivity can be further improved by combining ultra-fast MAS (50-60 kHz) with preparation schemes that utilize D_2O and/or deuterated amino

acids or glucose to further reduce ^{1}H-^{1}H dipolar couplings, leading to high-resolution ^{1}H-detected spectra. Nowadays, commercially available probe and MAS rotor enable spinning the sample at 126 kHz, which expands the use of ^{1}H detection to fully protonated samples that can be studied by high-resolution ^{1}H-detected ssNMR.

Dynamic nuclear polarization

Another method for sensitivity enhancement in ssNMR is by employing the dynamic nuclear polarization (DNP) technique (see., e.g., ref. [12]). In DNP experiments, electrons are polarized via microwave irradiation and this magnetization is transferred to NMR nuclei, usually ^{1}H spins. Since the gyromagnetic ratio of electron spins is ~660 times higher than ^{1}H, the magnetization transfer from electrons to nuclei greatly enhances NMR signals. DNP experiments are usually conducted at low temperature (~100 K) to enable efficient polarization transfer with microwave irradiation under MAS conditions (Figure 5). For a DNP sample preparation, (bi)radical compounds (see Figure 6 for some examples) that carry two electrons are usually added to a buffer solution containing cryoprotectants (usually glycerol-d_8). Under MAS conditions, the most efficient DNP polarization transfer is established using the so called cross-effect (when using biradicals of polarization agents)[13].

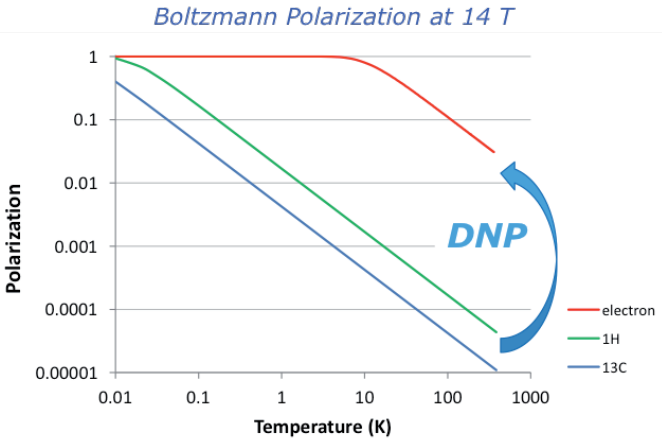

Figure 5. Temperature dependent polarization at 14T for different spins: electron (red), proton (green) and carbon (blue). Figure taken from ref[14].

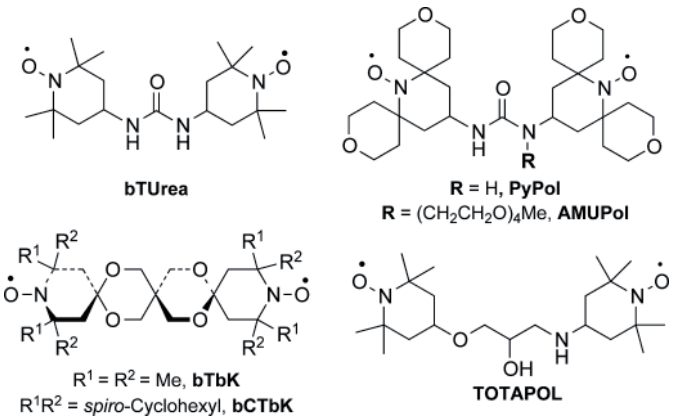

Figure 6. Examples of biradicals as polarization agents used for DNP. In this thesis, AMUPol was used. Figure is taken from ref[15].

NMR experiments used in this thesis

In this thesis, we studied microtubules as well as their interactions with microtubule-associated proteins (MAPs) using solid-state NMR. For reference, we also investigated the structure and dynamics of free MAPs using solution-state NMR. For example, in the latter case, we employed 2D ^{15}N- and ^{13}C-heteronuclear single-quantum correlation (HSQC) experiments[16], where magnetization is transferred through bond that is initiated from the direct-bonded protons of the amides or CH- groups to the attached ^{15}N or ^{13}C nuclei, resulting in the "fingerprints" of each residue of the free protein in solution (Figure 7). Note that these experiments can be also performed in ssNMR to probe the dynamic parts of the proteins[17]. Moreover, to obtain the backbone assignments of the proteins in solution, two complementary 3D experiments, HNCACAB and CBCA(CO)NH[18], were used and analyzed using the ^{15}N-HSQC as a reference. The HNCACB data set gives the chemical shift information for each peak in the HSQC spectrum of the residue I and the chemical shift information of the Cα and Cβ of residue i and of the previous residue (residue i-1) (Figure 8, left). The CBCA(CO)NH will also give the chemical shift information for each amide peak in the HSQC spectrum of the residue i but only the chemical shift information of the Cα and Cβ of residue i-1 (Figure 8, right). Hence, the information from this spectrum can be used to assign which Cα and Cβ are of the residue and of the previous residue in the HNCACB.

The corresponding analysis is also termed sequential resonance assignment in NMR.

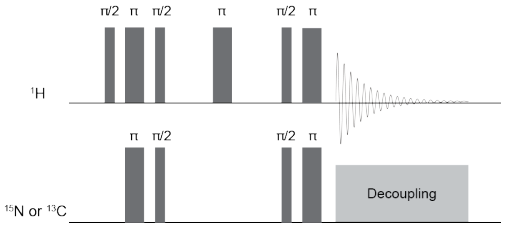

Figure 7. Schematic representation of ^{15}N- and ^{13}C-HSQC experiments[16].

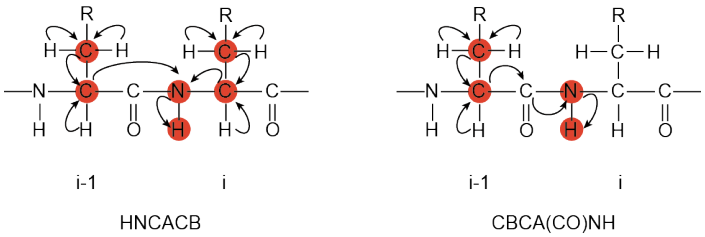

Figure 8. Schematic representation of magnetization transfer in the HNCACB (left panel) and the CBCA(CO)NH (right panel) experiments[18].

Next to the assignment of the NMR signals of the free protein, we also studied the dynamical properties of the free proteins. For example, to probe millisecond timescale chemical exchange of the protein of interest, we employed Carr-Purcell-Meiboom-Gill (CPMG)[19] relaxation dispersion and Chemical Exchange Saturation Transfer (CEST)[20] experiments in this thesis. In the case of a protein exchanging between the ground state and excited state, only the peaks for the ground state are visible if the population difference between the two states is significantly large and majority of the protein adopts a structure of the ground state. In CPMG experiment[19], a series of refocusing 180° pulses are applied during a constant transverse relaxation delay (40 ms was used in this thesis) (Figure 9a, upper panel). With increase of the CPMG pulse frequency, exchange-induced relaxation rate R_{ex} decreases and leads to reduction of the effective transverse relaxation rates ($R_{2,eff}$) (Figure 9a, lower panel). Therefore the $R_{2,eff}$ profile can be obtained using different CPMG pulse frequencies to reveal whether chemical exchange on the millisecond timescale occurs in the protein. In the CEST experiment[20], successive experiments with a weak B_1 field for a time

T_{EX} (15 Hz field for 400 ms on ^{15}N was used in this thesis) that "step" through the entire spectrum are recorded to probe the minor-state of the protein (Figure 9b). The signal intensity of the visible peak is unaffected when the field offset is far from either the ground or excited state. However, a reduction of intensity is detected when the field is resonant with the two states (Figure 9b, lower panel), thereby the chemical exchange of the protein can be probed and the chemical shift value of the minor state can be predicted.

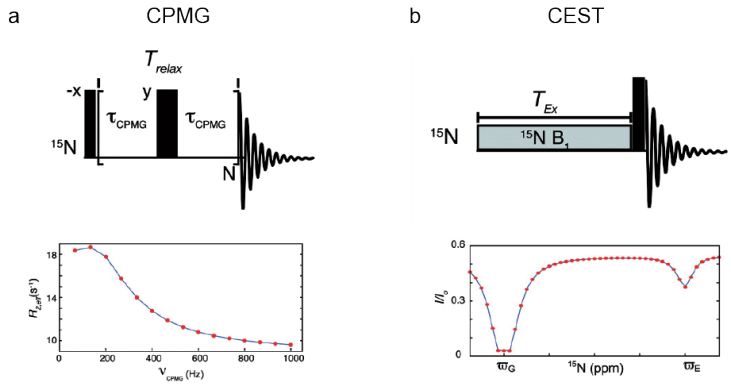

Figure 9. Schematic representation of a) CPMG and b) CEST experiments. The narrow and wide pulses represent 90° and 180° respectively. Typical relaxation dispersion curve obtained from CPMG and the intensity profile obtained from CEST experiments are shown under the pulse sequences respectively. Figure adapted from ref[20].

As for ssNMR experiments on microtubule-MAP complexes, we carried out carbon-detected experiments either under standard MAS rate (10-14 kHz) or fast MAS rate (44-55 kHz). The C-C Proton-Driven Spin Diffusion (PDSD)[21] and Radio Frequency-Driven Recoupling (RFDR)[22] was performed at standard and fast MAS rates respectively to characterize the folding of the proteins of interest. In this set of two-dimensional experiments, magnetization is transferred from protons to the ^{13}C nuclei via cross polarization. Magnetization is then exchanged between ^{13}C nuclei that are close in space, resulting in C-C cross peaks from all ^{13}C atoms within a certain distance, typically 5 Angstroms (Figure 10a). In addition, the NCA experiment[23] was used for analysis. In this case, magnetization transfer is initiated from protons to ^{15}N nuclei via cross polarization, then a specific cross polarization[24] is employed to transfer magnetization from ^{15}N to the $^{13}C\alpha$, resulting in a 2D N-C correlated spectrum (Figure 10b).

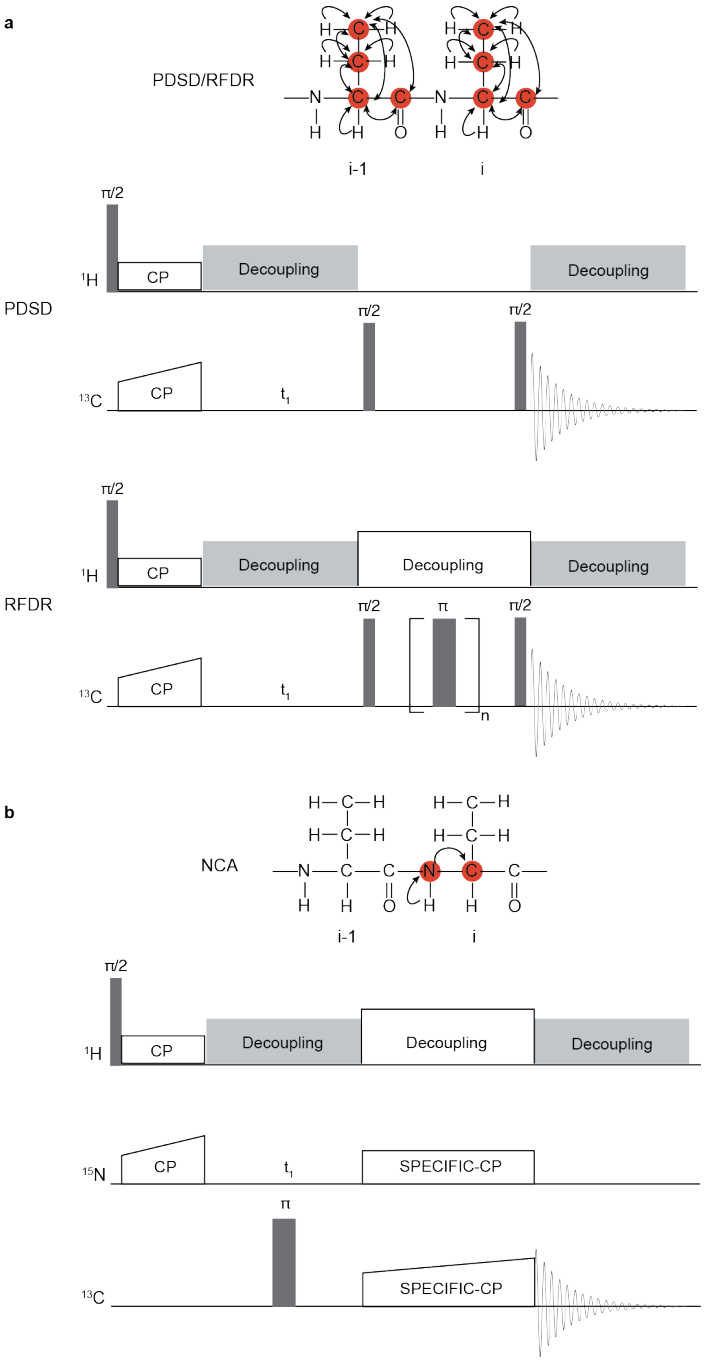

Figure 10. Schematic representation of magnetization transfer of a) PDSD/RFDR and b) NCA, as well as the pulse sequences of these experiments.

For ssNMR ^{1}H detection experiments, proteins with perdeuteration and back-exchanged amide protons were used for sample preparation to improve spectral resolution in the ^{1}H dimension as mentioned before. In the dipolar-based NH experiments magnetization is transferred from the amide protons to the ^{15}N nuclei via cross polarization, from which the magnetization is transferred back from ^{15}N to the amide protons, leading a 2D N-H correlated spectrum (Figure 11a). To transfer the solution assignments of proteins to the ssNMR experiments, the 3D CANH[25] experiment was used. In this experiment the magnetization is first transferred from the amide protons to the $^{13}C\alpha$ nuclei, followed by a specific cross polarization to transfer the magnetization to ^{15}N and then back to the amide protons for detection, resulting in a three-dimensional spectrum (Figure 11b). The spectrum is similar to the solution-state HNCA. The only difference is that in solution HNCA the amide nitrogen of residue i is coupled to the Cα of residue i and i-1, while the amide nitrogen of residue i is only coupled to the Cα of residue i in the solid-state CANH. Therefore, by combining the two spectra, the solution assignments of ^{1}HN, ^{15}N and $^{13}C\alpha$ can be transferred to the solid-state spectra for analysis. Notably, it is also possible to obtain complete sequential resonance assignments from ^{1}H ssNMR spectra using CANH, CONH, CAcoNH and COcaNH Experiments[4].

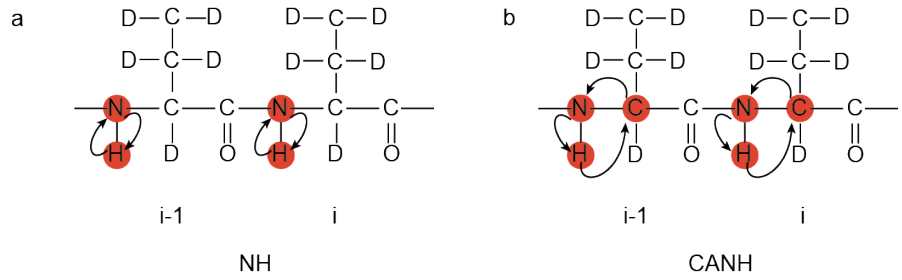

Figure 11. Schematic representation of magnetization transfer of a) NH and b) CANH experiments.

Microtubules

Microtubules (MTs) are important tubular cytoskeleton polymers in eukaryotic cells, which are formed by the α- and β-tubulin heterodimers (Figure 12a). The α/β-tubulin dimers (~110 kDa) bind in a head-to-tail manner to build a protofilament. In most cases 13 protofilaments associate in parallel to form a microtubule (Figure 12b), while microtubules can be also formed by different

numbers of protofilaments (e.g., 14 or 15 protofilaments)[26]. Therefore, microtubules are intrinsically polarized, with the α-tubulin-exposed minus end that is rather stable, and the dynamic plus end that exposes β-tubulin and switches rapidly with growth and shrinkage. Microtubules are essential in many cellular processes, including cell division, migration, polarization and intracellular trafficking, etc. In general, the centrosome is the main microtubule-organizing center (MTOC) in animal cells where microtubule nucleation takes place[27], while non-centrosomal microtubules can be also found, for example, in Golgi apparatus (in mammalian cells)[28], along existing microtubules[29], or anchored at the cell cortex[30]. There are two nucleotide-binding sites on each tubulin dimer. A guanosine-5'-triphosphate (GTP) is bound to α-tubulin and buried by the β-tubulin, making it non-hydrolysable, while the nucleotide bound to β-tubulin is exchangeable. Upon microtubule polymerization, The GTP bound on the β-tubulin is hydrolyzed into guanosine-5'-diphosphate (GDP). The GTP binding and hydrolysis on the plus end (also known as the GTP-cap model) determines the phase changes between microtubule polymerization and depolymerization so called 'dynamic instability'[31] (Figure 13). In addition, tubulin is associated with many post-translational modifications (PTMs), especially on the C-terminal tails. PTMs on the tubulin C-terminal tails include (de)tyrosination, polyglycylation, polyglutamylation and Δ2 (removal of the last two residues from the C-terminal tail of α-tubulin), which are related to different cellular processes and human diseases[32]. In addition, a lot of microtubule-binding agents bind to microtubules and they are used as drug for cancer treatments by either interfering depolymerization or polymerization of microtubules (for example, the microtubule stabilizer paclitaxel and microtubule destabilizer vincristine)[33].

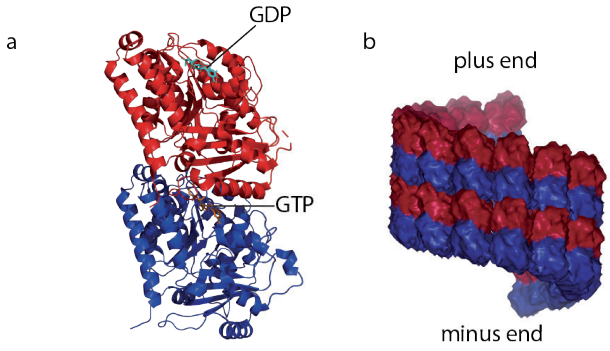

Figure 12. A) Cartoon representation of α/β-tubulin dimer (PDB: 4I55) and cryo-EM reconstruction of Taxol-stabilized microtubule (PDB: 5SYF). α- and β-tubulin are labeled in blue and red respectively.

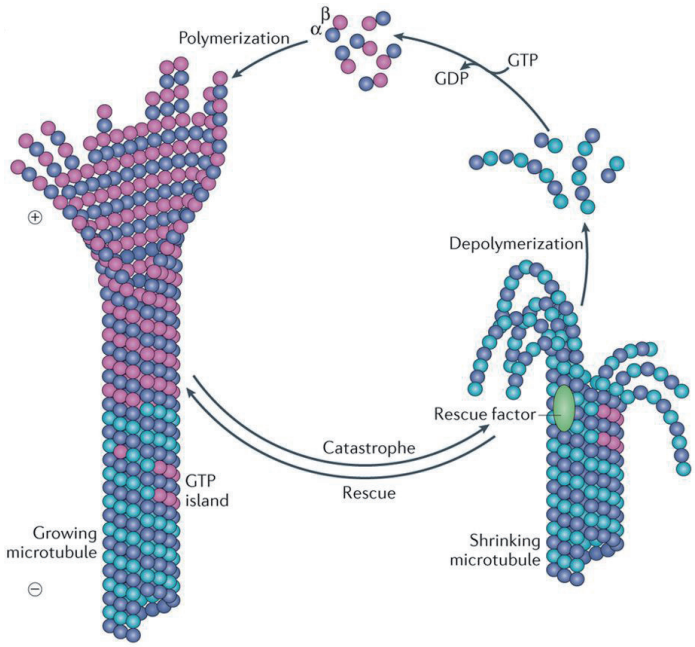

Figure 13. Schematic representation of the tubulin assembly-disassembly cycle. Figure adapted from ref[34].

Microtubule-associated proteins

The dynamics of the microtubule polymerization-depolymerization cycle is also regulated by the interactions of numerous microtubule-associated proteins (MAPs). In addition, Some MAPs can play important roles in directing microtubules to certain cellular locations, crosslinking microtubules with other proteins, or promoting microtubule bundling[34].

Among numerous MAPs, the microtubule plus-end-tracking proteins (+TIPs) are distinguished by their binding of growing ends of microtubule, which are important components of microtubule dynamics regulators[35]. For example, members of XMAP215 family of microtubule polymerases bind to microtubule plus end and recruit tubulin dimer to promote microtubule polymerization[36], while microtubule depolymerization can be regulated by members of kinesin-8, kinesin-13 or kinesin-14 families[34]. Members of kinesin-4 family can stabilize MT with a particular length[37], and the cytoplasmic linker protein-associated proteins (CLASPs) as well as the cytoskeleton-associated protein glycine-rich domain (CAP-

Gly domain) family proteins can promote rescue and suppress catastrophe of MTs[38]. In cells, the +TIPs coordinate as a network to regulate MT dynamics in order to guide MTs to different cellular locations, stabilize the attachment of plus ends to the cell cortex for transport of vesicles and other cellular signaling events[34].

On the other hand, the regulation of the microtubule minus end dynamics and the associated proteins on the minus ends are much less known. The main regulator that is associated with minus end is the γ-tubulin ring complex (γ-TURC), which binds to the microtubule minus ends and acts as a microtubule nucleation factor[39]. Recently, the calmodulin-regulated spectrin-associated protein (CAMSAP) family, which includes CAMSAP1, CAMSAP2 and CAMSAP3, was discovered to bind to the free minus ends of non-centrosomal microtubules and function independently of γ-TURC[40]. CAMSAP1 can track the growing microtubule minus ends, while CAMSAP2 and CAMSAP3 decorate stretches on the microtubule lattice and stabilize minus ends[41]. Therefore, CAMSAP proteins are known as microtubule minus-end-targeting proteins (–TIPs).

Besides the +TIPs and –TIPs, some MAPs have been discovered that bind the lattice of microtubules, including stable tubule-only polypeptide (STOP, also known as MAP6)[42] and the MAP7 protein family[43].

Structural studies of microtubule in complex with small molecules and MAPs

The dynamic structural organization of microtubule is crucial in eukaryotic cells, and the interactome of microtubules is a complicated network that involves numerous molecules including MAPs to regulate the microtubule assembly-disassembly cycle. Therefore, understanding the detailed molecular mechanisms of the transition between polymerization and depolymerization, as well as how microtubules and MAPs interact and function, especially at the atomic level, becomes very important. With the resolution revolution of cryo-electron microscopy (cryo-EM), high-resolution structures of stabilized and dynamic microtubules can be obtained and compaction of the interdimer interface can be observed upon GTP hydrolysis[44]. Additionally, cryo-EM can provide structural information of microtubule-binding agents or MAPs in complex

with microtubules[45]. Due to the filamentous nature of microtubules, X-ray crystallography has been of limited use to directly obtain information on microtubules and their interactions with MAPs. Instead, X-ray crystallography has strongly contributed to elucidating binding mechanisms of different microtubule-binding agents via studying monomeric tubulin and these experiments have provided useful information for drug development[46].

For more than a decade, NMR has shown its potential to carry out structural studies on microtubules/tubulin and their interactions with small molecules[47] and MAPs[48]. For example, the binding pockets of MAP6 with microtubules were determined by solution-state NMR. The same study also showed that calmodulin (calcium-modulated protein) competes with microtubules for MAP6 binding, since MAP6 uses similar regions for calmodulin binding[48a]. More recently, the microtubule-binding mechanism of the companion of cellulose synthase 1 to plant microtubules was demonstrated by solution-state NMR[48b]. Moreover, NMR can provide information of local dynamics of microtubules, including the disordered tubulin C-terminal tails that are largely absent in current cryo-EM and x-ray crystallography structures. Indeed, a recent study on isotope-labeled tubulin from *T. thermophile* showed that the detyrosination and polyglycylation PTMs on the unstructured, flexible tubulin C-terminal tails[49].

Complementary to such solution-state NMR studies, ssNMR has been used to directly study the interactions of microtubules with microtubule-binding agents or MAPs. For example, our group could previously show that the binding of the microtubule-stabilizing agent patupilone to microtubules could be detected by ssNMR and that this interaction resulted in large chemical shift changes of patupilone compared the free-state patupilone[47]. In addition, ssNMR was used to study the binding mode of CAP-Gly domain of dynactin with microtubules and the data revealed that the structural plasticity of CAP-Gly domain enables it to adopt conformational changes upon binding to microtubules[5a]. On the other hand, to directly study the structures and dynamics on the microtubules with ssNMR has so far been precluded due to the difficulty of obtaining sufficient yields of isotope-labeled microtubules[50], which leads to high expense of isotope labeling.

In this thesis, the binding modes of two kinds of MAPs, the minus-end binding CAMSAP proteins and MAP7 were studied upon interactions with microtubules by ssNMR. The structures of these proteins as well as the details of their interactions with MTs are still under investigation. Previous studies discovered that CAMSAPs bind and stabilize the microtubule minus ends[41]. CAMSAPs have a N-terminal calponin homology (CH) domain, three predicted coiled-coil regions (CC1, CC2 and CC3) and a helical domain, as well as the C-terminal CKK domain, which is the domain that binds to the microtubule minus end (Figure 14). On the other hand, MAP7 binds the microtubule lattice and can recruit the kinesin-1 motor protein to 'walk' along the microtubules[51]. MAP7 contains a N-terminal microtubule-binding domain, which is predicted as a coiled-coil domain, and a C-terminal kinesin-1 binding domain that recruits kinesin-1 to microtubules. Between the two structured domains there is a long intrinsically disordered region (Figure 14). A recent study showed that part of the intrinsically disordered region is also associated the microtubule binding[52].

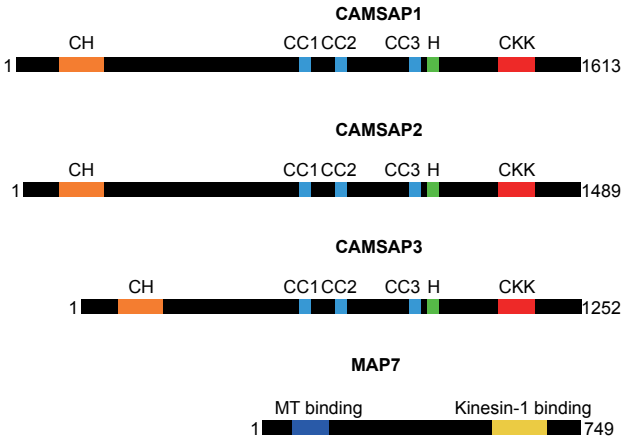

Figure 14. Schemes of domain organization of mammalian CAMSAPs and MAP7 proteins. H: helical domain. In this thesis, the CKK domains from CAMSAP1 and CAMSAP3, as well as the microtubule-binding domain of MAP7 were studied.

Scope of this thesis: In **Chapter 1**, a general introduction about solid-state NMR and its recent advancements in terms of NMR sensitivity (DNP, proton detection) and resolution is given. The biological background of microtubules and microtubule-associated proteins is also introduced in this chapter.

In Chapter 2: we discuss the preparation of the isotope-labeled CKK domain of CAMSAP3 in complex with microtubules. We could obtain chemical-shift perturbations and local dynamics changes upon CKK domain binding to microtubules compared to the free CKK, thereby allowing to identify the binding interface of CKK with microtubules.

In Chapter 3: we study the structural determinants of the CKK domain binding to microtubules. We apply high-resolution ^{1}H detection on CKK in complex with microtubules to obtain residue-specific information of the behavior of the domain upon binding to microtubules. We also probe the local dynamics of CKK domain to shed light on the properties of CKK that induce conformational changes of microtubules upon interaction.

In Chapter 4: we investigate and compare the N-terminal microtubule-binding region of human MAP7 between free- and bound-state with microtubules by using NMR and integrated structural biology techniques to discover the binding mode and mechanism of MAP7 with microtubules.

In Chapter 5: we present a general protocol that enables to prepare functional, isotope-labeled tubulin and microtubules from mammalian cells for ssNMR studies. In combination with ^{1}H detection and DNP we are able to probe the rigid tubulin subunits in microtubules and loop regions that exhibit sizable dynamics. Moreover, this approach allowed us to directly detect the disordered, flexible tubulin tails and the nucleotides bound to tubulin.

In Chapter 6: a general discussion regarding the data presented in the previous chapters and future perspectives as well as recommendations for future ssNMR studies on microtubule dynamical properties and, their interactions with other proteins are given.

Finally, a summary of the thesis is presented.

References:

[1] V. Tugarinov, L. E. Kay, *Journal of the American Chemical Society* **2003**, *125*, 13868-13878.

[2] a) B. H. Meier, R. Riek, A. Böckmann, *Trends in Biochemical Sciences* **2017**, *42*, 777-787; b) M. Renault, A. Cukkemane, M. Baldus, *Angewandte Chemie-International Edition* **2010**, *49*, 8346-8357.

[3] a) V. Ladizhansky, *Biochimica et Biophysica Acta (BBA) - Proteins and Proteomics* **2017**, *1865*, 1577-1586; b) M. Kaplan, C. Pinto, K. Houben, M. Baldus, *Quarterly Reviews of Biophysics* **2016**, *49*, 1-26.

[4] S. Xiang, U. B. le Paige, V. Horn, K. Houben, M. Baldus, H. van Ingen, *Angewandte Chemie International Edition* **2018**, *57*, 4571-4575.

[5] a) S. Yan, C. Guo, G. Hou, H. Zhang, X. Lu, J. C. Williams, T. Polenova, *Proceedings of the National Academy of Sciences* **2015**, *112*, 14611; b) J. Yehl, E. Kudryashova, E. Reisler, D. Kudryashov, T. Polenova, *Scientific Reports* **2017**, *7*, 44506.

[6] a) B. E. Ackermann, G. T. Debelouchina, *Angewandte Chemie International Edition* **2019**, *58,* 6300; b) C. Ader, S. Frey, W. Maas, H. B. Schmidt, D. Gorlich, M. Baldus, *Proceedings of the National Academy of Sciences of the United States of America* **2010**, *107*, 6281-6285.

[7] E. R. Andrew, A. Bradbury, R. G. Eades, *Nature* **1958**, *182*, 1659-1659.

[8] S. Penzel, A. Oss, M.-L. Org, A. Samoson, A. Böckmann, M. Ernst, B. H. Meier, *Journal of Biomolecular NMR* **2019**, *73*, 19-29.

[9] E. Barbet-Massin, G. Pintacuda, in *NMR of Biomolecules* (Eds.: I. Bertini, K. S. McGreevy, G. Parigi), **2012**.

[10] nmr900.ca/testspectra_e.html.

[11] A. Pines, M. G. Gibby, J. S. Waugh, *The Journal of Chemical Physics* **1972**, *56*, 1776-1777.

[12] A. S. Lilly Thankamony, J. J. Wittmann, M. Kaushik, B. Corzilius, *Progress in Nuclear Magnetic Resonance Spectroscopy* **2017**, *102-103*, 120-195.

[13] D. Mance, P. Gast, M. Huber, M. Baldus, K. L. Ivanov, *The Journal of Chemical Physics* **2015**, *142*, 234201.

[14] bruker.com/products/mr/nmr/dnp-nmr/overview.html.

[15] C. Sauvée, M. Rosay, G. Casano, F. Aussenac, R. T. Weber, O. Ouari, P. Tordo, *Angewandte Chemie International Edition* **2013**, *52*, 10858-10861.

[16] N. E. Jacobsen, in *NMR Spectroscopy Explained*, **2007**.

[17] O. C. Andronesi, S. Becker, K. Seidel, H. Heise, H. S. Young, M. Baldus, *Journal of the American Chemical Society* **2005**, *127*, 12965-12974.

[18] S. Grzesiek, A. Bax, *Journal of Magnetic Resonance (1969)* **1992**, *99*, 201-207.

[19] D. M. Korzhnev, L. E. Kay, *Accounts of Chemical Research* **2008**, *41*, 442-451.
[20] P. Vallurupalli, G. Bouvignies, L. E. Kay, *Journal of the American Chemical Society* **2012**, *134*, 8148-8161.
[21] N. M. Szeverenyi, M. J. Sullivan, G. E. Maciel, *Journal of Magnetic Resonance (1969)* **1982**, *47*, 462-475.
[22] A. E. Bennett, C. M. Rienstra, J. M. Griffiths, W. Zhen, P. T. Lansbury, R. G. Griffin, *The Journal of Chemical Physics* **1998**, *108*, 9463-9479.
[23] M. Baldus, *Progress in Nuclear Magnetic Resonance Spectroscopy* **2002**, *41*, 1-47.
[24] M. Baldus, A. T. Petkova, J. Herzfeld, R. G. Griffin, *Molecular Physics* **1998**, *95*, 1197-1207.
[25] D. H. Zhou, A. J. Nieuwkoop, D. A. Berthold, G. Comellas, L. J. Sperling, M. Tang, G. J. Shah, E. J. Brea, L. R. Lemkau, C. M. Rienstra, *Journal of Biomolecular NMR* **2012**, *54*, 291-305.
[26] R. H. Wade, D. Chrétien, D. Job, *Journal of Molecular Biology* **1990**, *212*, 775-786.
[27] J. Wu, A. Akhmanova, *Annual Review of Cell and Developmental Biology* **2017**, *33*, 51-75.
[28] M. Rios Rosa, *Philosophical Transactions of the Royal Society B: Biological Sciences* **2014**, *369*, 20130462.
[29] C. Sánchez-Huertas, J. Lüders, *Current Biology* **2015**, *25*, R294-R299.
[30] A. D. Sanchez, J. L. Feldman, *Current Opinion in Cell Biology* **2017**, *44*, 93-101.
[31] A. Desai, T. J. Mitchison, *Annual Review of Cell and Developmental Biology* **1997**, *13*, 83-117.
[32] S. Gadadhar, S. Bodakuntla, K. Natarajan, C. Janke, *Journal of Cell Science* **2017**, *130*, 1347.
[33] C. Dumontet, M. A. Jordan, *Nature Reviews Drug Discovery* **2010**, *9*, 790.
[34] A. Akhmanova, M. O. Steinmetz, *Nature Reviews Molecular Cell Biology* **2015**, *16*, 711.
[35] A. Akhmanova, M. O. Steinmetz, *Nature Reviews Molecular Cell Biology* **2008**, *9*, 309.
[36] G. J. Brouhard, J. H. Stear, T. L. Noetzel, J. Al-Bassam, K. Kinoshita, S. C. Harrison, J. Howard, A. A. Hyman, *Cell* **2008**, *132*, 79-88.
[37] P. Bieling, I. A. Telley, T. Surrey, *Cell* **2010**, *142*, 420-432.
[38] a) N. Galjart, *Nature Reviews Molecular Cell Biology* **2005**, *6*, 487; b) J. E. Lazarus, A. J. Moughamian, M. K. Tokito, E. L. F. Holzbaur, *PLOS Biology* **2013**, *11*, e1001611.
[39] J. M. Kollman, A. Merdes, L. Mourey, D. A. Agard, *Nature Reviews Molecular Cell Biology* **2011**, *12*, 709.

[40] M. C. Hendershott, R. D. Vale, *Proceedings of the National Academy of Sciences* **2014**, *111*, 5860.

[41] K. Jiang, S. Hua, R. Mohan, I. Grigoriev, Kah W. Yau, Q. Liu, Eugene A. Katrukha, A. F. M. Altelaar, Albert J. R. Heck, Casper C. Hoogenraad, A. Akhmanova, *Developmental Cell* **2014**, *28*, 295-309.

[42] C. Bosc, A. Andrieux, D. Job, *Biochemistry* **2003**, *42*, 12125-12132.

[43] E. Gallaud, R. Caous, A. Pascal, F. Bazile, J.-P. Gagné, S. Huet, G. G. Poirier, D. Chrétien, L. Richard-Parpaillon, R. Giet, *The Journal of Cell Biology* **2014**, *204*, 1111.

[44] Gregory M. Alushin, Gabriel C. Lander, Elizabeth H. Kellogg, R. Zhang, D. Baker, E. Nogales, *Cell* **2014**, *157*, 1117-1129.

[45] E. H. Kellogg, N. M. A. Hejab, S. Poepsel, K. H. Downing, F. DiMaio, E. Nogales, *Science* **2018**, *360*, 1242.

[46] A. E. Prota, K. Bargsten, D. Zurwerra, J. J. Field, J. F. Díaz, K.-H. Altmann, M. O. Steinmetz, *Science* **2013**, *339*, 587.

[47] A. Kumar, H. Heise, M. J. J. Blommers, P. Krastel, E. Schmitt, F. Petersen, S. Jeganathan, E.-M. Mandelkow, T. Carlomagno, C. Griesinger, M. Baldus, *Angewandte Chemie International Edition* **2010**, *49*, 7504-7507.

[48] a) J. Lefèvre, P. Savarin, P. Gans, L. Hamon, M.-J. Clément, M.-O. David, C. Bosc, A. Andrieux, P. A. Curmi, *The Journal of biological chemistry* **2013**, *288*, 24910-24922; b) C. Kesten, A. Wallmann, R. Schneider, H. E. McFarlane, A. Diehl, G. A. Khan, B.-J. van Rossum, E. R. Lampugnani, W. G. Szymanski, N. Cremer, P. Schmieder, K. L. Ford, F. Seiter, J. L. Heazlewood, C. Sanchez-Rodriguez, H. Oschkinat, S. Persson, *Nature Communications* **2019**, *10*, 857.

[49] K. P. Wall, M. Pagratis, G. Armstrong, J. L. Balsbaugh, E. Verbeke, C. G. Pearson, L. E. Hough, *ACS Chemical Biology* **2016**, *11*, 2981-2990.

[50] N. Kaul, V. Soppina, Kristen J. Verhey, *Biophysical Journal* **2014**, *106*, 2636-2643.

[51] P. J. Hooikaas, M. Martin, T. Mühlethaler, G.-J. Kuijntjes, C. A. E. Peeters, E. A. Katrukha, L. Ferrari, R. Stucchi, D. G. F. Verhagen, W. E. van Riel, I. Grigoriev, A. F. M. Altelaar, C. C. Hoogenraad, S. G. D. Rüdiger, M. O. Steinmetz, L. C. Kapitein, A. Akhmanova, *The Journal of Cell Biology* **2019**, jcb.201808065.

[52] S. R. Tymanskyj, B. H. Yang, K. J. Verhey, L. Ma, *eLife* **2018**, *7*, e36374.

CHAPTER 2

2

A structural model for microtubule minus-end recognition and protection by CAMSAP proteins

Adapted from

Joseph Atherton, Kai Jiang, Marcel M Stangier, Yanzhang Luo, Shasha Hua, Klaartje Houben, Jolien J E van Hooff, Agnel-Praveen Joseph, Guido Scarabelli, Barry J Grant, Anthony J Roberts, Maya Topf, Michel O Steinmetz, Marc Baldus, Carolyn A Moores and Anna Akhmanova

Nature Structural & Molecular Biology volume 24, pages 931–943 (2017).

Abstract

CAMSAP and Patronin family members regulate microtubule minus-end stability and localization and thus organize noncentrosomal microtubule networks, which are essential for cell division, polarization and differentiation. Here, we found that the CAMSAP C-terminal CKK domain is widely present among eukaryotes and autonomously recognizes microtubule minus ends. Through a combination of structural approaches including solution- and solid-state NMR, we uncovered how mammalian CKK binds between two tubulin dimers at the interprotofilament interface on the outer microtubule surface. *In vitro* reconstitution assays combined with high-resolution fluorescence microscopy and cryo-electron tomography suggested that CKK preferentially associates with the transition zone between curved protofilaments and the regular microtubule lattice. We propose that minus-end-specific features of the interprotofilament interface at this site serve as the basis for CKK's minus-end preference. The steric clash between microtubule-bound CKK and kinesin motors explains how CKK protects microtubule minus ends against kinesin-13-induced depolymerization and thus controls the stability of free microtubule minus ends.

Introduction

Microtubules (MTs) are highly dynamic polymers that assemble and disassemble from their two ends: the fast-growing plus end and the slow-growing minus end. Although abundant data are available regarding the regulation of MT plus ends[1], much less is known about the proteins that specifically regulate MT minus ends, although MT minus-end organization defines the architecture of cellular MT arrays[2]. The best-studied MT-nucleating and minus-end-binding factor is the γ-tubulin ring complex (γ-TuRC)[3]. Recently, the members of calmodulin-regulated spectrin-associated protein (CAMSAP) and the Patronin family have been shown to control noncentrosomal MT minus-end organization independently of γ-TuRC in different systems, including the mitotic spindle in insect cells[4], cortically attached MT arrays in epithelial cells[5] and MT bundles in neurons[6].

CAMSAP1, CAMSAP2 and CAMSAP3 (in vertebrates) and Patronin (in invertebrates) recognize and track uncapped, growing MT minus ends[7]. In mammals, CAMSAP2 and CAMSAP3 are deposited on MT lattices formed by MT minus-end polymerization and in this way generate stable MT stretches that can serve as a source of noncentrosomal MT outgrowth[8]. In contrast, CAMSAP1 tracks growing MT minus ends but does not decorate them[7]. CAMSAPs and Patronin contain a C-terminal domain common to **C**AMSAP1, **K**IAA1078 and **K**IAA1543 (CKK) as well as an N-terminal Calponin-homology domain and several coiled-coil regions[9]. In mammalian CAMSAPs, minus-end recognition has been shown to depend on the CKK domain, whereas the ability of CAMSAP2 and CAMSAP3 to stay attached to the MT lattice is associated with additional adjacent regions[7]. However, in fly Patronin, minus-end recognition has been proposed to be mediated by the unstructured linker region in combination with the adjacent C-terminal coiled coil[10]. The deletion of the CKK domain in CAMSAP3 causes a loss-of-function phenotype in mice[5], and the CKK domain of Patronin (PTRN-1) in worms is necessary and sufficient for supporting proper MT dynamics and axon regeneration[6a], thus demonstrating the functional importance of this domain.

Here, we set out to investigate the nature of the MT minus-end specificity of CAMSAPs. Structural analysis by X-ray crystallography, cryo-EM and solid-state NMR showed that the globular CKK domain binds a unique site between two tubulin dimers at the interprotofilament interface. Fluorescence microscopy demonstrated that the high-affinity site for CKK binding is located several tubulin dimers behind the outmost MT minus end. Cryo-electron tomography (cryo-ET) of MT minus ends revealed a heterogeneous array of gently curved protofilaments that retain lateral interactions. On the basis of these data, we propose that the CKK preferentially binds the transition zone between the regular lattice and the curved sheet-like structure of the minus-end extremity, which presents a subtly altered interprotofilament interface that is optimal for CKK binding. Finally, our structural and *in vitro* reconstitution data showed that CKK sterically hinders the interaction of kinesin-13 with MT minus ends, thereby explaining how CAMSAPs and Patronin protect MT minus ends against depolymerization by these factors.

Materials and methods

NMR sample preparation and experiments. Uniformly ^{13}C-^{15}N-labeled variants of CKK were produced in *E. coli* strain Rosetta 2 in M9 minimum medium containing 25 µg/ml kanamycin and 35 µg/ml chloramphenicol. The cells were induced with 0.3 mM IPTG at 25 °C overnight after the OD_{600} reached 0.6. Proteins were purified by a ÄKTA pure system with a POROS™ MC column that was saturated with Ni^{2+}. The column was first equilibrated with washing buffer (50 mM phosphate buffer, pH 8, 200 mM NaCl, 1 mM β-mercaptoethanol and 20 mM imidazole). Proteins were eluted with the same buffer but containing 400 mM imidazole. After purification, proteins were loaded onto a SEC HiLoad Superdex 75 26/60 column (GE Healthcare), which was equilibrated in 40 mM phosphate buffer with 150 mM NaCl and 1 mM DTT, pH 7.0. Proteins were then concentrated and used for solution-state NMR measurements with 5% D_2O supplementation or for ssNMR sample preparation.

For ssNMR experiments, [^{13}C, ^{15}N] CAMSAP3 CKK–MT complexes were prepared. 20 mg of lyophilized tubulin was first dissolved in BRB80 buffer to a final concentration of 2 mg/ml. Tubulin was then polymerized with the addition of 20 µM paclitaxel for 30 min at 37 °C. Paclitaxel-stabilized MTs were centrifuged at 55,000 rpm (Beckman TLA-55 rotor) at 30 °C for 30 min. The pellet was resuspended in warm BRB80 buffer, and labeled CKK domain was added to a final concentration of 65.3 µM (4:1 CKK/tubulin). The mixture was incubated at 37 °C for 30 min and then centrifuged at 55,000 rpm (Beckman TLA-55 rotor) at 30 °C for 30 min. The pellet was washed with phosphate buffer without disturbing the pellet. Finally, the pellet was transferred and packed into a 3.2-mm rotor.

Resonance assignments were obtained from previous results (PDB 1UGJ), and additional solution-state NMR experiments on free CKK were recorded on a 600-MHz spectrometer (Bruker Biospin) to assign missing residues. In detail, we conducted two-dimensional (2D) HSQC, as well as three-dimensional (3D) HNCA, HNCO, HNCACB, CBCA(CO)NH, HAHB(CO)NH and hCCH-DIPSI experiments[11]. ssNMR experiments involved 2D NCA and CC proton-driven spin-diffusion (PDSD) experiments (temperature 260 K, MAS rate 14 kHz). Mixing schemes used SPECIFIC-CP transfers[12] (in the case of ^{15}N-^{13}C polarization transfer) and spin diffusion under weak coupling conditions[13] (for the purpose of ^{13}C-^{13}C

polarization transfer) for PDSD mixing times. Data were recorded on a 950-MHz standard-bore spectrometer (Bruker Biospin) equipped with a 3.2-mm triple-channel MAS HCN probe. ssNMR data were analyzed by using NMR assignments obtained on free CKK as a reference. Resolved residues in our NCA ssNMR spectra that exhibited correlations that matched the solution-state NMR data within 0.5 ppm in ^{13}C and 1 ppm in ^{15}N dimensions were considered unperturbed. Likewise, resolved residues whose signals matched with ssNMR data within 1 ppm in the indirect dimension and 0.5 ppm in the direct dimension in the ^{13}C-^{13}C PDSD experiments were treated as unperturbed. Larger deviations were considered altered and are below (Figure 10a, b) indicated in red.

Protein purification for crystallization. *Mus musculus* CAMSAP3 CKK proteins was purified according to ref[14].

Protein expression and purification for cryo-EM. Human CAMSAP1 wild type, N1492A CKK (residues 1474–1613) and mouse CAMSAP3 CKK (residues 1112–1252) were cloned into the pET28a vector. After purification with Ni–NTA resin (Qiagen), proteins were further purified on a MonoS ion-exchange column and a Superose 6 gel-filtration column (GE Healthcare). Purified proteins were concentrated to ~20 mg/ml in BRB20 buffer.

Protein expression and purification for *in vitro* assays. All proteins used for TIRFM were expressed according to ref[14]. The CKK of *P. infestans* was obtained by PCR from genomic DNA (a gift from F. Govers, Wageningen University). Fly and worm Patronin cDNAs were kindly provided by V. Gelfand (Northwestern University) and M. Harterink (Utrecht University), respectively. In CAMSAP1$_{mini}$-GFP protein, the GFP tag was inserted directly after the C terminus of the CKK domain and was followed by a short flexible linker (CAMSAP1$_{1227–1613}$-GGSGGS-GFP). Purifications of protein were performed according to ref[14].

Total internal reflection fluorescence microscopy (TIRFM) and *In vitro* MT assays. TIRFM and *in vitro* assays were performed according to ref[14].

Quantification of the intensity of the wild-type and mutant CAMSAP1$_{mini}$ on dynamic MTs. To quantify the minus-end and lattice intensity of CAMSAP1$_{mini}$ in a time-lapse movie, kymographs were generated in ImageJ with the KymoResliceWide plug-in. The minus-end positions were marked by 5-pixel-wide linear ROIs corresponding to CAMSAP1 mini signals. The maximum intensity within the 5-pixel region along the spatial axis of the kymograph was measured with a macro written in ImageJ.

Structure determination of the CAMSAP3 CKK domain. CKK3$_{core}$ was concentrated to 14 mg/ml and the structure was determined according to ref[14].

MT pelleting assays. 10 mg/ml porcine brain tubulin was diluted in 1×BRB80 buffer (80mM K-PIPES, pH 6.8, supplemented with 1 mM EGTA, 1 mM $MgCl_2$ and 1 mM DTT) to 2 mg/ml. After the addition of 1 mM GTP, the sample was incubated on ice for 5 min. MT polymerization was started by transfer to 37 °C with 20 µM paclitaxel. Pelleting assays in the presence of CAMSAP3 CKK were performed by mixing with different molar ratios of CKK:MTs. As control treatments, taxol-stabilized MTs or CAMSAP3 CKK was applied alone. Samples were then centrifuged at 180,000g for 30 min at 25 °C, an aliquot was taken from the supernatant. After removal of the supernatant, the pellet was resuspended in SDS sample buffer. Samples were loaded and analyzed on Coomassie-stained 15% SDS gels.

Cryo-EM. Cryo-EM experiments and data processing were performed according to ref[14].

Results

Minus-end recognition by CAMSAPs depends on the conserved CKK domain

We have previously shown that the CKK domain in mammalian CAMSAPs binds minus ends[7]. To investigate whether other CAMSAP domains might also control minus-end recognition, we tested the ability of different purified GFP-tagged CAMSAP1 domains to bind to MT minus ends and lattices *in vitro*. None of the CAMSAP fragments that lacked the CKK domain showed any minus-end preference (Figure 1a–f). We found that the predicted helical domain and the linker, which precede the CKK, had only very weak MT affinity of their own but increased MT binding of CAMSAP1 CKK, though not its minus-end selectivity (Figure 1a–f). An additional negatively charged linker region of CAMSAP1, located upstream of its third coiled-coil domain, suppressed MT-lattice binding and enhanced minus-end selectivity when it was present together with the CKK domain (Figure 1a–e; this construct is denoted CAMSAP1$_{mini}$). We concluded that the minus-end preference of CAMSAPs depends on the CKK domains, whereas additional domains modulate their end selectivity or ability to decorate MT lattices.

To test whether the sequence conservation of CKK translates into functional conservation, we next purified GFP-tagged CKK domains derived from flies (*Drosophila melanogaster*) and worms (*Caenorhabditis elegans*), as well as from four more evolutionarily distant eukaryotes (*Trichomonas vaginalis*, *Tetrahymena thermophila*, *Naegleria gruberi* and *Phytophthora infestans*). From these six CKK domains tested, four (*D. melanogaster*, *C. elegans*, *T. vaginalis* and *T. thermophila*) specifically tracked the growing minus ends of MTs assembled from pig-brain tubulin in in vitro MT-dynamics reconstitution experiments (Fig. 1g), whereas the two others (*N. gruberi* and *P. infestans*) showed strong binding along the entire MT lattice (data not shown). These data demonstrated that CKK is a protein module that recognizes MT minus ends, a property preserved over long evolutionary distances.

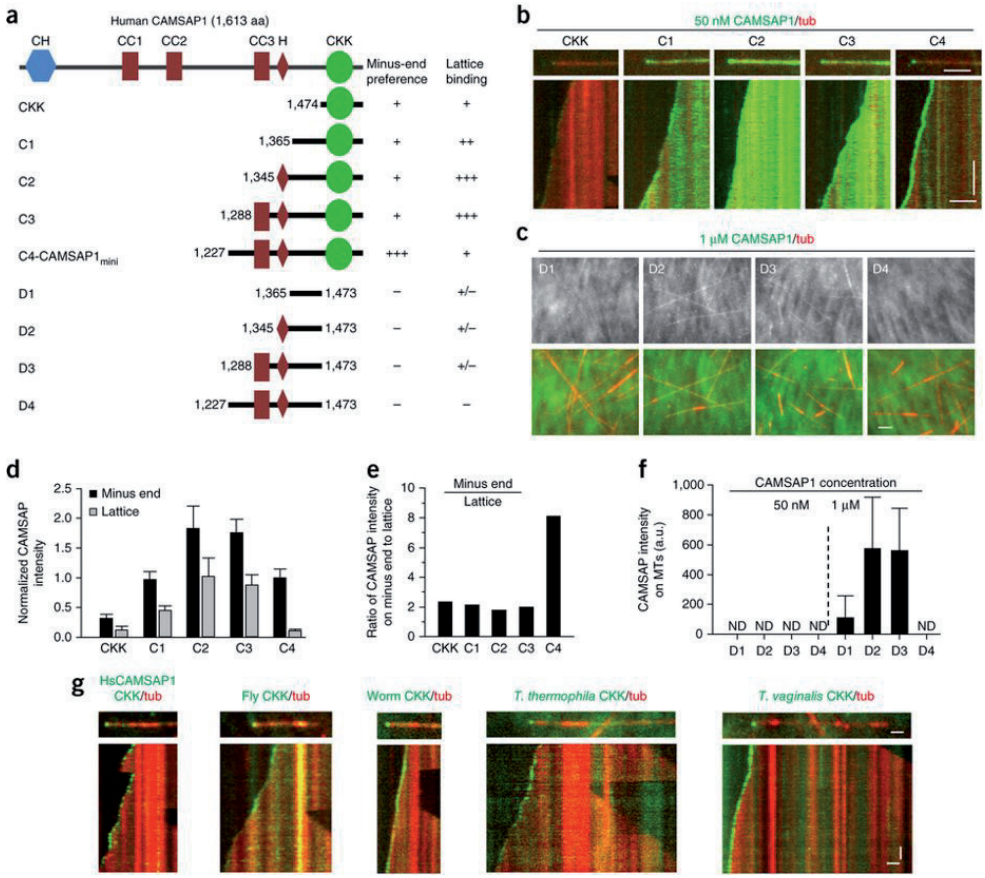

Figure 1. The CKK is a highly conserved domain for MT minus-end tracking. (a) Schematic of CAMSAP1 domain organization and the constructs used. (b,c) kymographs (b) and corresponding TIRFM images (c). Scale bars: horizontal, 2 µm; vertical, 2 min. (d–f) Quantification of localization of GFP-CAMSAP1 fragments to MT minus ends and lattice, based on data in b and c. The intensity was normalized to the average minus-end intensity of the C4 fragment. Data are mean ± s.d., n = 30 MTs. ND, not detectable; a.u., arbitrary units. (g) TIRFM images (top) and kymographs (bottom) of GFP-tagged CKK domains from humans (CAMSAP1), flies (*D. melanogaster)*, worms (*C. elegans*), *T. thermophile* and *T. vaginalis.* Scale bars: horizontal, 1 µm; vertical, 30 s. Tub, tubulin.

CKK are well-folded domains in the free-state

To study the binding mode of CKK with MTs, we employed solution-state NMR to characterize the structural elements of the CAMSAP3 CKK domain. To obtain backbone assignments for free CAMSAP3 CKK, we recorded 2D ^{15}N-HSQC, 3D HNCACB, CBCA(CO)NH and HNCA experiments. The dispersion of the peaks on the HSQC spectrum indicated that the CKK domain was well folded and that the

3D structure comprised elements of different secondary structures (Figure 2a). By analyzing the Cα and Cβ signals, sequential backbone connections could be obtained for protein assignments (Figure 2b). Based on the assigned backbone chemical shifts, we could predict the secondary structure of CKK domain by using TALOS+[15]. The TALOS+ results suggested that the CKK domain consists of two N-terminal α helices, as well as six β strands (Figure 3), which is in line with previously deposited but unpublished NMR structure (PDB: 1UGJ). We also obtained assignments for the N- and C-termini of CAMSAP3 CKK domain. The N-terminus was fully assigned, while the assignments for C-terminus were not complete due to the repetitiveness of the amino-acid sequence such as in the case of K1239 and K1240. Taken together, the resonance assignments obtained strongly suggest that both termini are unstructured and flexible. The complete assignment list has been deposited in Biological Magnetic Resonance Data Bank (BMRB) with the entry code: 27234.

To further characterize the 3D structure of CKK domain, we determined the crystal structure of the mouse CAMSAP3 CKK domain core (residues 1121–1239; denoted $CKK3_{core}$). Similar to our NMR data, the $CKK3_{core}$ has a compact, globular structure composed of two N-terminal α-helices, which are connected by a disordered loop (loop1) and pack against a central five-stranded β-sheet (Figure 4). To facilitate crystallization, a protein construct was used in which the tail was truncated (see caption Figure 4b). Taken together, our understanding of the free CKK structure provided the basis to further study the interaction of CKK domains in complex with MTs.

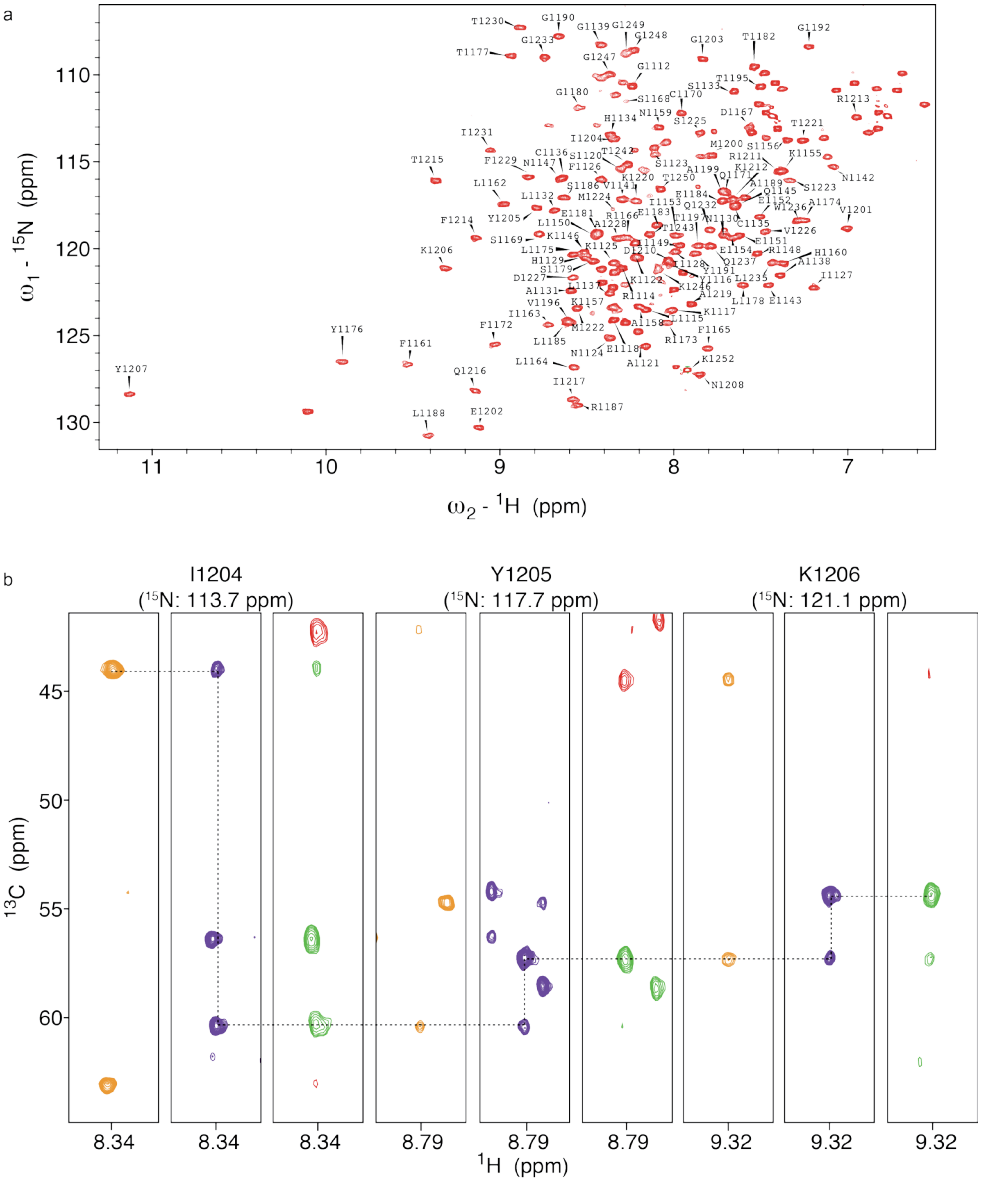

Figure 2. Structure elucidation of *M. musculus* CAMSAP3 CKK domain as seen by solution-state NMR. a) Solution-state assignments of free-state CAMSAP3-CKK as shown on the ^{15}N-HSQC spectrum. b) Strips of CBCA(CO)NH (orange), HNCA (purple) and HNCACB (green and red) of I1204 to K1206 are shown as examples of sequential backbone assignments of the corresponding Cα signals.

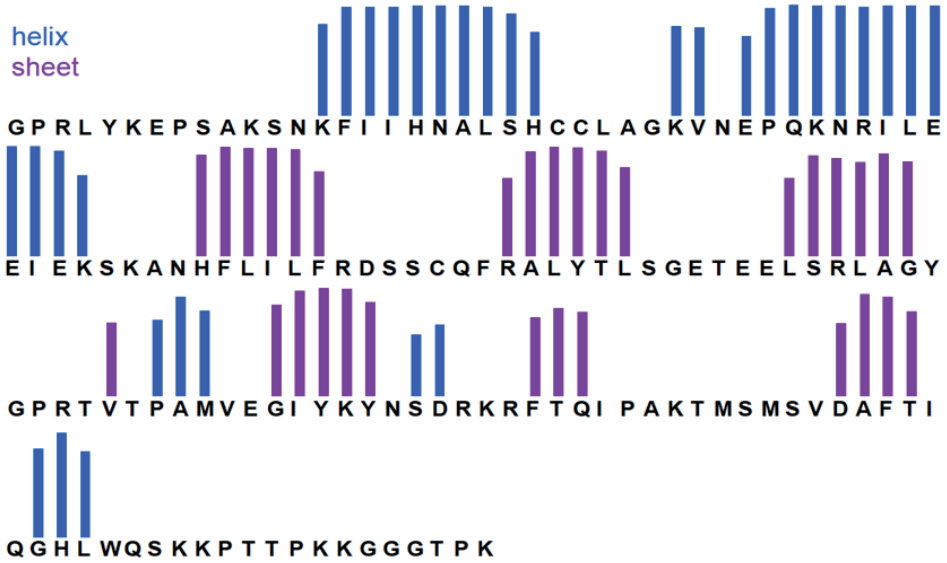

Figure 3. TALOS+ prediction of propensities for secondary structural elements of *M. musculus* CAMSAP3 CKK domain based on the assignments shown in Figure 2.

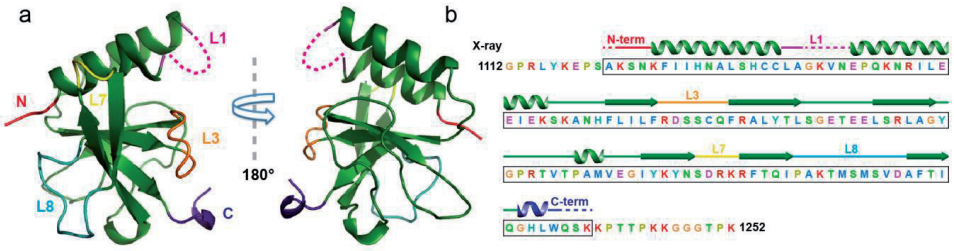

Figure 4. The X-ray crystal structure of the mouse CAMSAP3 CKK domain. a) Two views 180° apart of the ribbon representation of the *M. musculus* CAMSAP3 CKK domain crystal structure. Key loops as well as the N- and C-termini of the domain are labeled. b) The *M. musculus* CAMSAP3 CKK sequence, colored according to side chain property, is shown, with overlying secondary structure based on our crystal structure. The boxed region indicates the construct used for X-ray crystallography. Secondary structure estimations deduced by X-ray crystallography are indicated above, color coded consistent with the scheme in panel a, with unsolved regions indicated with dashed lines.

CKK domains bind an intradimer site between protofilaments

Although CKK shows a clear preference for MT minus ends, at high concentrations it can also decorate the entire MT lattice. We reasoned that a high-resolution structure of the lattice-bound CKK domain might shed light on the

mechanism of its MT minus-end recognition. Therefore, we used cryo-EM to analyze the extended CKK domain of CAMSAP3 (1112–1252) bound to 13-protofilament (pf) taxol-stabilized MTs. Filtered images of these MTs showed additional density corresponding to CKK domains spaced by 8 nm (Figure 5a), a result indicative of binding every tubulin dimer. A striking feature of these CKK-decorated MTs is the presence of a right-handed skew in the protofilaments. This feature was evident in the filtered images of the MT segments used for reconstruction and was specific to the CKK–MT data sets (Figure 5a, b). This result indicated that CKK binding modifies the MT lattice with which it interacts, in agreement with the idea that the regular MT lattice conformation is not the most favored substrate for CKK domains.

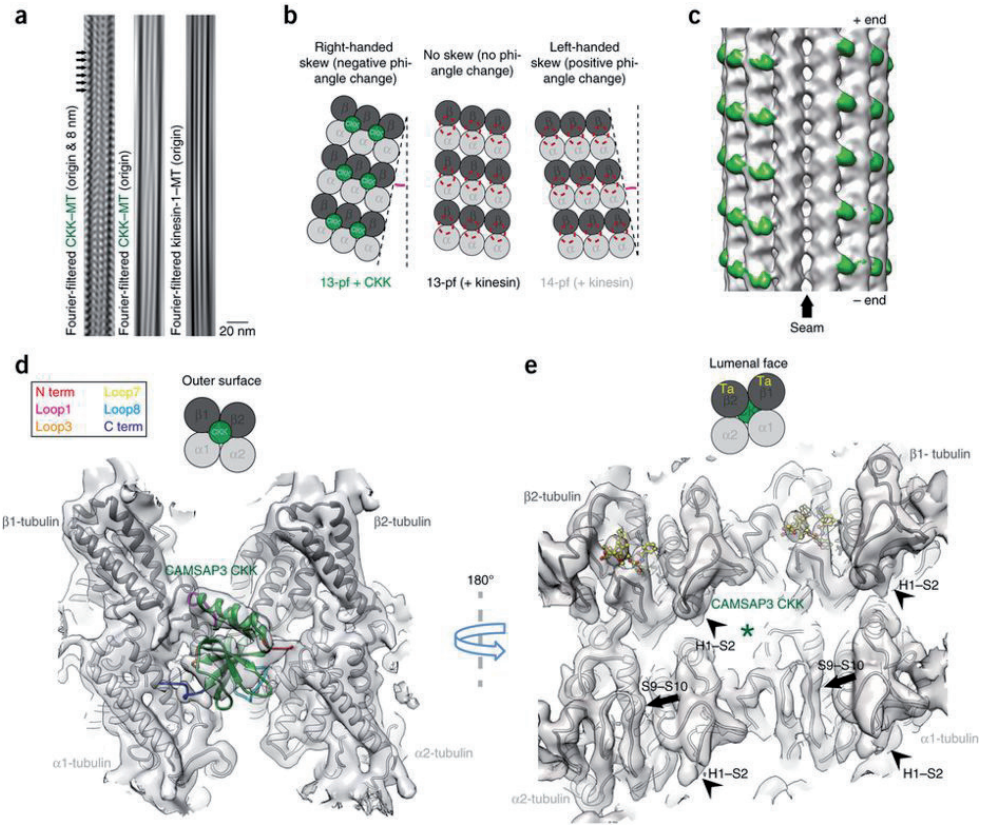

Figure 5. a) Fourier-filtered images of 13-pf MTs. Left, filtering of a CAMSAP3-CKK decorated 13-pf MT showing density corresponding to the CAMSAP3 CKK domain every tubulin dimer; center, filtering highlighting the MT moiré pattern and the presence of protofilament skew. Right, filtering of a kinesin-1-decorated 13-pf MT, highlighting a comparative lack of skew. b) Schematic of three sets of three protofilaments depicting the skew

detected in the CKK 13-pf MT data sets (left) compared with kinesin-bound 13-pf (middle) and 14-pf paclitaxel-stabilized MTs (right). The skew-angle size is exaggerated for ease of viewing. c) The asymmetric reconstruction of the CAMSAP3-CKK-decorated 13-pf paclitaxel-stabilized MT low-pass filtered to 15-Å resolution, showing extra densities (green) every 8 nm corresponding to the CAMSAP3 CKK domains, which are absent at the seam (arrow). d) The averaged reconstruction of the CAMSAP3 CKK domain viewed from the MT surface contacting two β-tubulins and two α-tubulins at the intradimer interprotofilament interface. The CKK is colored as in the X-ray structure (Figure 3), except for the N terminus (red) and loop1 (magenta), which are absent in our crystal structure but visible in our EM density. α-tubulin is shown in light gray, and β-tubulin is shown in dark gray. Term, terminus. e) The averaged reconstruction of the MT-bound CAMSAP3 CKK domain viewed from the MT lumen, showing density corresponding to paclitaxel bound to β-tubulin (yellow). Along with the distinctive appearance of the H1–S2 and S9–S10 loops (arrowheads and arrows, respectively). In d and e, schematic drawings appear on top. Ta, paclitaxel-binding site.

An asymmetric 3D reconstruction (~9 Å resolution) showed the CKK domain binding the MT lattice every 8 nm between protofilaments except at the seam (Figure 5c). Using the pseudosymmetry of the MTs, we obtained an averaged reconstruction with overall final resolutions (5.3 Å) that allowed α- and β-tubulin to be clearly distinguished (Figure 4d,e). From these data, we concluded that CKK domains bind at the tubulin intradimer B-lattice interface, where conserved differences between α- and β-tubulin explain this binding-site selection (Figure 6a).

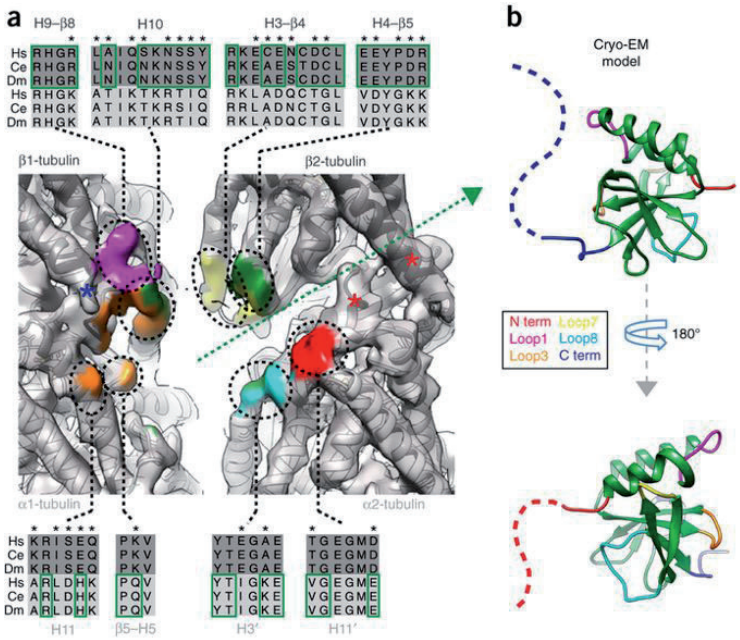

Figure 6. a) CKK-interaction surface of the MT, with cryo-EM density colored according to CKK contacts (<6 Å distance; coloring as in Figure 5d). Sequence alignments for contact regions in β-tubulin (top) and α-tubulin (bottom) indicate sequence differences between human α1a tubulin and β3 tubulins (asterisks) that may

contribute to CKK binding to the intra- versus the interdimer site. Comparison between *H. sapiens* (Hs) β3 tubulin and α1a tubulin (most common isoforms in mammalian brain[16]); *C. elegans* (Ce) β1 tubulin and α3 tubulin; and *D. melanogaster* (Dm) β1 tubulin and α-tubulin at 84B. Residues contacting the CKK are within green boundaries. b) 180° rotations of the CKK domain, with loop coloring referring to MT contact sites in a.

For ease of description, the four tubulin subunits contacting a single CKK domain are referred to as β1-, β2-, α1- and α2-tubulin (Figures 5d,e and 6a). In general, the CKK wedges snugly between the β-tubulins and forms more extensive contacts with the β-tubulins than with the α-tubulins (Figure 6a). Contacts between the CKK domain and its MT-binding site are distributed across the domain and also involve the N and C termini (Figures 5d and 6a,b).

To confirm and extend the details of CKK interaction with MTs at the atomic level, we then analyzed the structure of the CKK domain of CAMSAP3 bound to MTs using solid-state NMR (ssNMR). To prepare the CKK/MTs complex for ssNMR, a MT pelleting assay was first performed for optimization of our NMR sample preparation. As shown on the SDS-PAGE gel for the pelleting assay, no unbound CKK was detected when using a molar ratio of 1:1 for CKK:MTs, while a higher molar ratio of CKK:MTs resulted in remaining unbound CKK in the supernatant after ultracentrifugation (Figure 7). We therefore used a molar ratio of 4:1 for CKK:MTs to prepare our ssNMR sample. Subsequently, we prepared a [^{13}C, ^{15}N] uniformly labeled CAMSAP3 CKK in complex with taxol-stabilized MTs was prepared and packed it into a 3.2 mm MAS rotor for measurements. We firstly recorded a ^{13}C-^{13}C Proton-Driven Spin Diffusion (PDSD) experiment to obtain a global structural view of the ssNMR sample. For this purpose, we overlaid the assignments of free CKK obtained from solution-state NMR onto the ssNMR spectrum (Figure 8). Overall, the assignments, in particular the backbone correlations involving Cα-Cβ and Cβ-Cγ correlations, matched well with the spectrum, indicating that CKK remained folded upon interaction with MTs. With a ^{13}C-^{13}C mixing time of 30 ms in this experiments, some sidechain correlations with Cα, for example, the isoleucine Cα-Cδ cross peaks were predicted but not visible in the spectrum due to the longer distance between the two carbons compared to Cα-Cβ correlations. Similar results were obtained for the 2D NCA and NCACX experiments showing that the backbone correlations agreed well between free- and bound-state CKK (Figure 9).

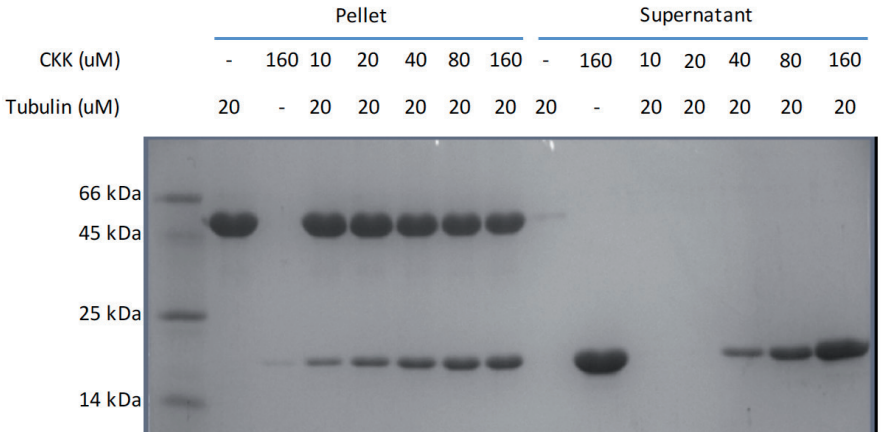

Figure 7. Optimization of sample preparation for CAMSAP3 CKK in complex with MTs. A MT pelleting assay was performed with different molar ratios of CKK:tubulin. As a result, a molar ratio of CKK:tubulin=4:1 was used for sample preparation for ssNMR studies to allow maximum decoration of CKK on MTs.

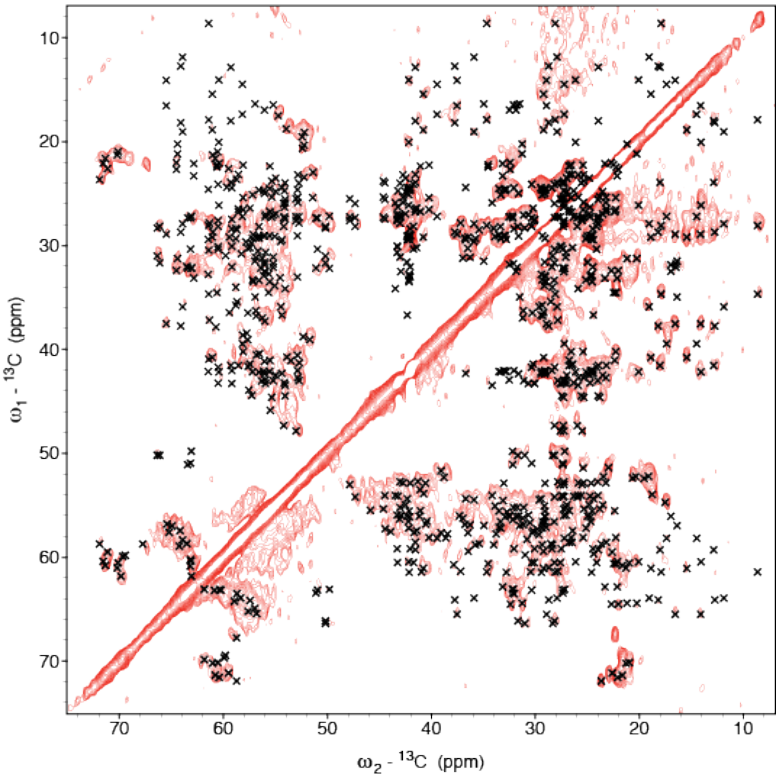

Figure 8. ^{13}C-^{13}C PDSD with 30 ms C-C mixing time of [^{13}C, ^{15}N] labeled CAMSAP3 CKK in complex with Taxol-stabilized MTs. To evaluate the sample quality and analyze the binding mode of CKK domain, the assignments of free-state CKK obtained in solution-state NMR (black crosses) are overlaid onto the spectrum.

Next we aimed to identify the binding interface of CKK domain and MTs. To do so, we compared the solution NMR results (including the PDB 1UGJ) and our X-ray crystallographic results of free CKK with 2D ssNMR data (^{13}C-^{13}C PDSD in Figure 8, NCA in Figure 9) recorded on [^{13}C, ^{15}N] labeled CKK in complex with MTs. This procedure allowed us to identify CKK residues that underwent significant chemical-shift/intensity changes after MT binding (Figure 10a-c, labeled in red) and those that experienced no significant change (labeled in blue). For example, in our EM density, helix α1 of the CKK domain sits across the β1- and β2-tubulins, while beneath it, loop7 and adjacent regions of the β-barrel wedge in between the β-tubulin subunits (Figure 6). Consistently with this configuration, residues from MT-bound CKK helix-α1 and adjacent loop7 displayed ssNMR chemical-shift differences relative to free CKK (for example, I1127, I1128 and R1213, Figure 10c). Similarly, our cryo-EM and ssNMR data corroborated interactions between CKK loop1 (G1139 seen in ssNMR) and β1-tubulin, and CKK loop7 and β2-tubulin, while CKK loop3 (C1170 seen in ssNMR) lies at the intradimer interface contacting both β1-tubulin and α1-tubulin. CKK loop8 is well positioned to form contacts with α2-tubulin, and our ssNMR data supported the involvement of this loop in the MT interaction. For example, V1226 and D1227 both show chemical shift or signal intensity difference compared to the free state CKK. However, loop8 is visible only at less conservative cryo-EM density thresholds thus suggesting that this loop has greater flexibility than the rest of the CKK domain in this region. Together, our results demonstrated that residues identified to undergo changes in ssNMR signals cluster on the CKK MT-facing surface. In contrast, residues displaying unaltered ssNMR signals are predominantly solvent exposed (Figure 10b-e). The ssNMR data thus supported the EM-derived binding mode at an atomic level.

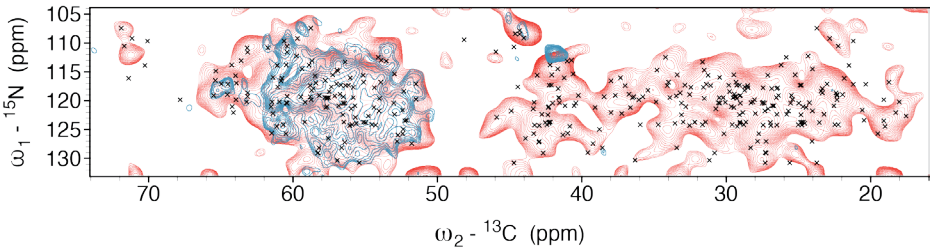

Figure 9. 2D NCA (blue) and NCACX (red) with 30 ms C-C mixing time of [^{13}C, ^{15}N] labeled CAMSAP3 CKK in complex with Taxol-stabilized MTs. The assignments of free-state CKK obtained in solution-state NMR (black crosses) are overlaid onto the spectra.

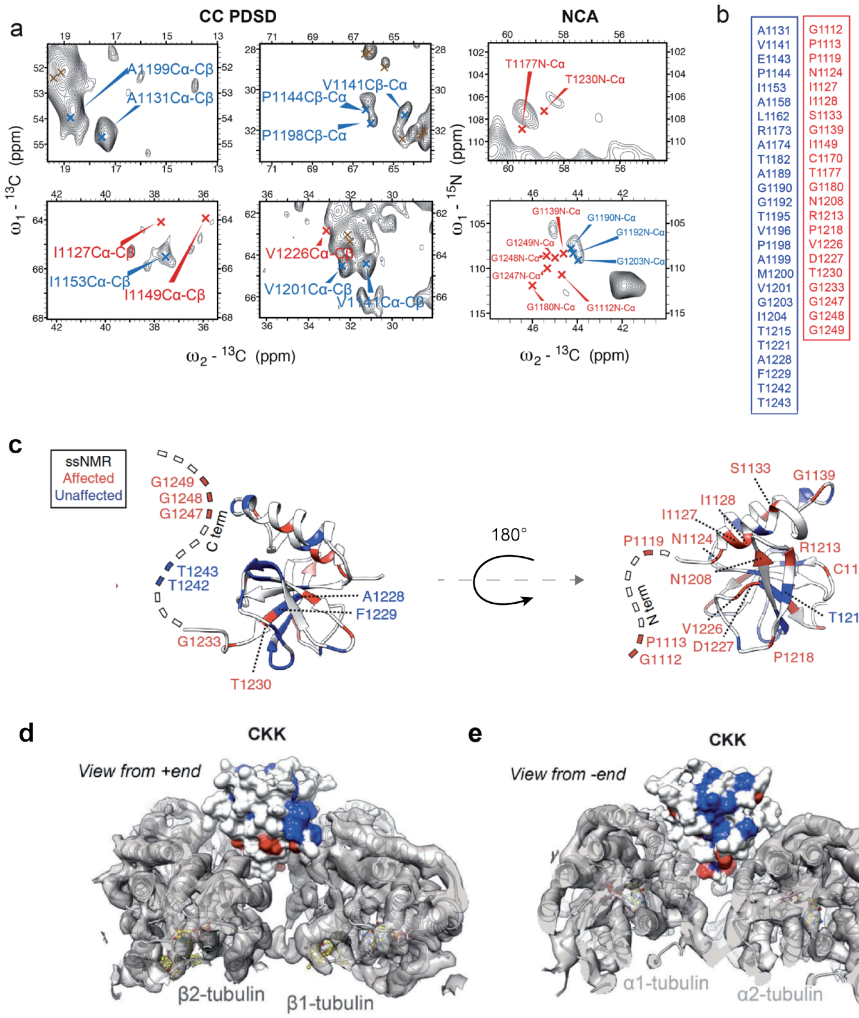

Figure 10. a) Zooms of well-resolved regions in the solid-state ^{13}C-^{13}C (PDSD, left and middle panels) and NCA (right panel) ssNMR spectra of [^{15}N, ^{13}C] labeled CKK bound to MTs. Crosses indicate expected signals based on solution-state chemical shifts of free CKK in solution. Signals for which a good match is found between expected and observed chemicals shifts are indicated in blue, while the absence of a corresponding signal is indicated in red. Brown crosses correspond to expected signals in overlapping regions. b) Full list of affected (red) and unaffected (blue) residues based on the NMR data. c) CKK views as in Figure 5b, showing ssNMR data on [^{13}C, ^{15}N] labeled CKK–decorated MTs relative to free CKK. Red, residues showing significant chemical-shift or intensity changes; blue, residues showing no change; white, residues not analyzed. The unresolved N and C termini are represented as dashed lines with each dash depicting a single residue. d, e) View from the MT plus-end d) or minus-end e) of the MT-bound CKK, reporting on ssNMR data obtained on [^{13}C, ^{15}N] labeled CKK decorated MTs relative to NMR results on free CKK. The CKK is shown as a color-coded surface representation whilst a ribbon representation of the MT (light grey for α-tubulin and dark grey for β-tubulin) is shown within its respective grey transparent solid cryo-EM density. CKK residues that underwent significant chemical-

shift/intensity changes are colored in red (affected) and those that experienced no change are indicated in blue (unaffected). White residues were not analyzed due to signal overlap.

The CKK N and C termini are not visible in the crystal structure, and both are flexible in solution (see above and PDB 1UGJ). However, our cryo-EM and ssNMR data also supported a role of the CKK N and C termini in MT binding. Density corresponding to the final portion of the N terminus leading into helix-α1 (starting at S1120) is visible in our cryo-EM reconstruction contacting α2-tubulin (Figure 6a and 11a, left panel), and the additional cryo-EM density suggests that more N-terminal regions make additional contacts with β2-tubulin (red asterisks in Figure 6a; red dashed line in Figure 11a, left panel). The CKK N terminus is therefore partially stabilized in complex with the MT, in agreement with the N-terminal truncation construct having lower MT affinity (Figure 11a, middle and right panels). Furthermore, although this region was not readily modeled, cryo-EM density corresponding to the conserved basic C terminus of the CKK domain and/or the β-tubulin C-terminal tail is visible (Figure 11b, left panel). ssNMR measurements in the CAMSAP3 CKK–MT complex suggested that the CKK C terminus retains some conformational variability when interacting with MTs (Figure 10c). In particular, we detected ssNMR signals from T1242 and T1243 on the CKK C-terminal tail in our dipolar based ssNMR experiments (Figure 10c and 11c). This observation implies that these two residues are rigidified by MTs upon the interaction. However, we did not detect signals from residues G1247, G1248 and G1249 (Figure 10c), indicating that this part of the C-terminal tail most likely remains flexible. The location of the CKK C terminus suggested that it interacts with the flexible acidic C-terminal tail of β1-tubulin; this possibility was supported by the observation that the interaction of GFP-tagged CAMSAP3 CKK domain with MTs significantly decreased after the acidic C-terminal tails of tubulin had been cleaved (Figure 11b, middle and right panels). Together, our cryo-EM and ssNMR data showed that CKK binds through multiple binding sites across two tubulin dimers at their intradimer interface between protofilaments and associates more closely with β-tubulin than α-tubulin.

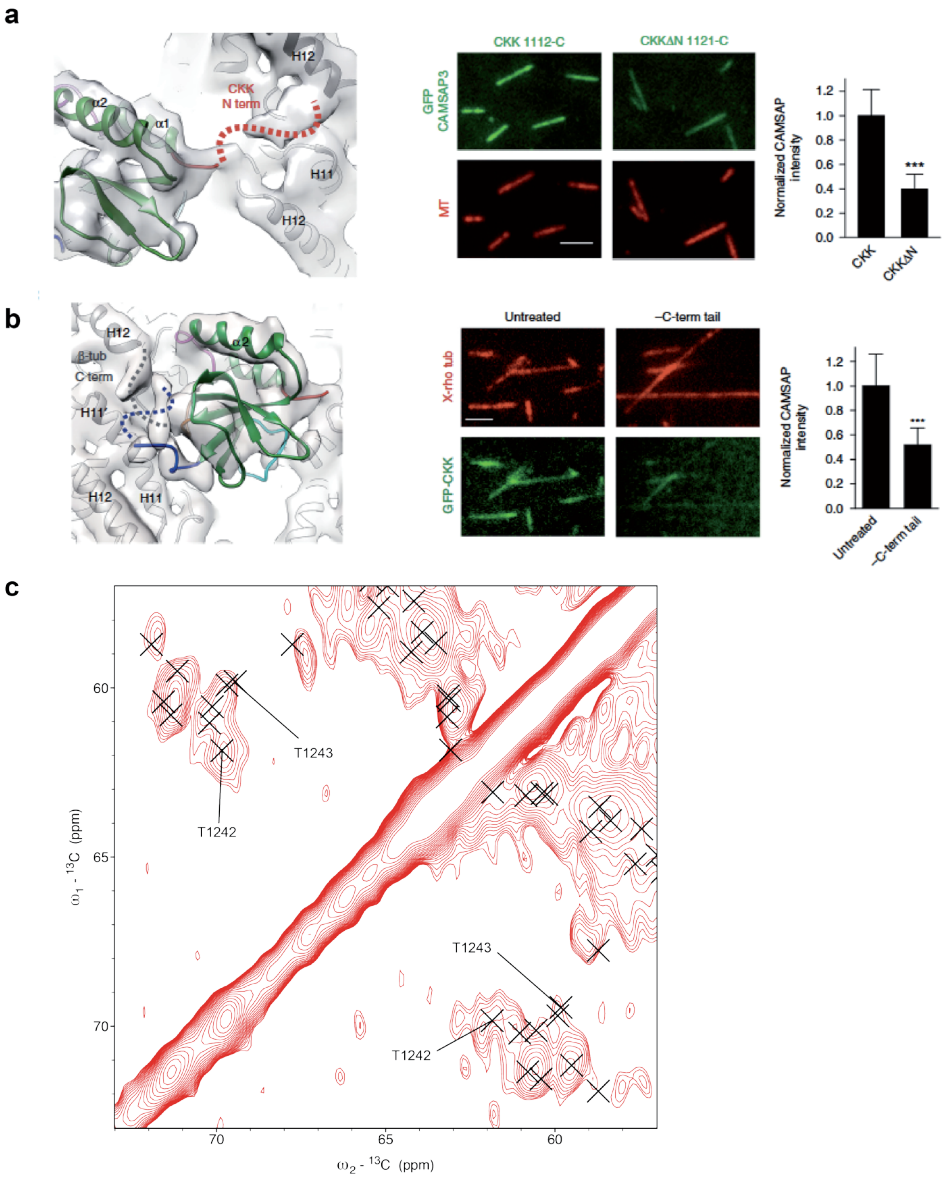

Figure 11. a) CAMSAP3 CKK–MT cryo-EM density at lower threshold, showing the CKK N terminus (left panel). TIRFM experiments showing the importance of the CKK N-terminal extension in MT binding. Intensity is normalized to average CKK lattice intensity. Scale bar, 2 µm. Data are mean ± s.d.; CKK, n = 104 MTs; CKKΔN, n = 118 MTs. ***P < 0.001, two-tailed Mann–Whitney U test (middle and right panels). b) CAMSAP3 CKK–MT cryo-EM density probably corresponding to interaction between the CKK flexible C terminus (blue dotted line) and the β-tubulin C terminus (gray dotted line), not usually seen in MT reconstructions[17] (left panel). X-rhodamine (rho)-labeled paclitaxel-stabilized MTs (red), either untreated or treated with subtilisin to remove their C-terminal tails, incubated with 200 nM GFP-tagged CAMSAP3 CKK and imaged with TIRFM. Scale bar, 4 µm. The intensity of MT labeling, normalized to that of wild type, is quantified. Data are mean ± s.d., n = 100 MTs. ***P <

0.001, two-tailed Mann–Whitney U test (middle and right panels). c) Zoom-in region of threonine Cα-Cβ correlations of a ^{13}C-^{13}C PDSD spectrum shown in Figure 7. T1242 and T1243, which are located in the CKK C-terminal tail, were detected in this experiment.

Analysis of CKK mutants supports the identified CKK–MT interface

To further validate the identified CKK–MT binding mode, we made a series of CKK mutants in the context of a short version of CAMSAP1 ($CAMSAP_{1mini}$, residues 1227–1613), which displayed more robust minus-end tracking activity than that of the CKK domain alone (Figure 1a–e). Mutations of several conserved positively charged residues decreased the overall binding affinity of $CAMSAP1_{mini}$ toward MTs and their minus ends (Figure 12a–c). Truncation of the N-terminal extension or mutations of positively charged residues in this sequence had a similar effect, as did truncations of the positively charged C-terminal tail region (Figure 12a). These data supported the validity of our CKK–MT lattice reconstruction and its relevance for CKK binding to the MT minus end.

Unexpectedly, a mutation of a conserved asparagine residue (N1492 of CAMSAP1) to alanine dramatically increased the ability of CKK to bind to the MT lattice and decreased, though did not abolish, its selectivity toward minus ends (Figure 12a–c). The importance of CAMSAP1's N1492 residue was further emphasized by the observation that mutating it to bulky charged or uncharged amino acids decreased the affinity of CKK for both MT minus ends and lattices, whereas substituting it for either serine or threonine enhanced MT lattice binding and decreased minus-end selectivity even further (Figure 12d). CAMSAP1 N1492 is expected to contact the C terminus of helix H4 of β2-tubulin (cyan in Figure 12b), and our data suggested that the formation of the CKK–MT complex is very sensitive to both the size and the chemical nature of the side chain in this position. For example, the potential hydrogen-bond formation between this residue and β-tubulin may affect the affinity of the CKK–MT interaction. Overall, these experiments identified two main classes of mutations: (i) mutations of positively charged CKK residues, which weakened the interaction between CKK and the negatively charged surfaces of the MT ends and lattice, including less structurally ordered regions of both the CKK and MT, and (ii) mutations that specifically increased lattice binding. Remarkably, the effects of these latter

mutations were rather subtle, thus suggesting that the mechanism of minus-end discrimination itself is also subtle.

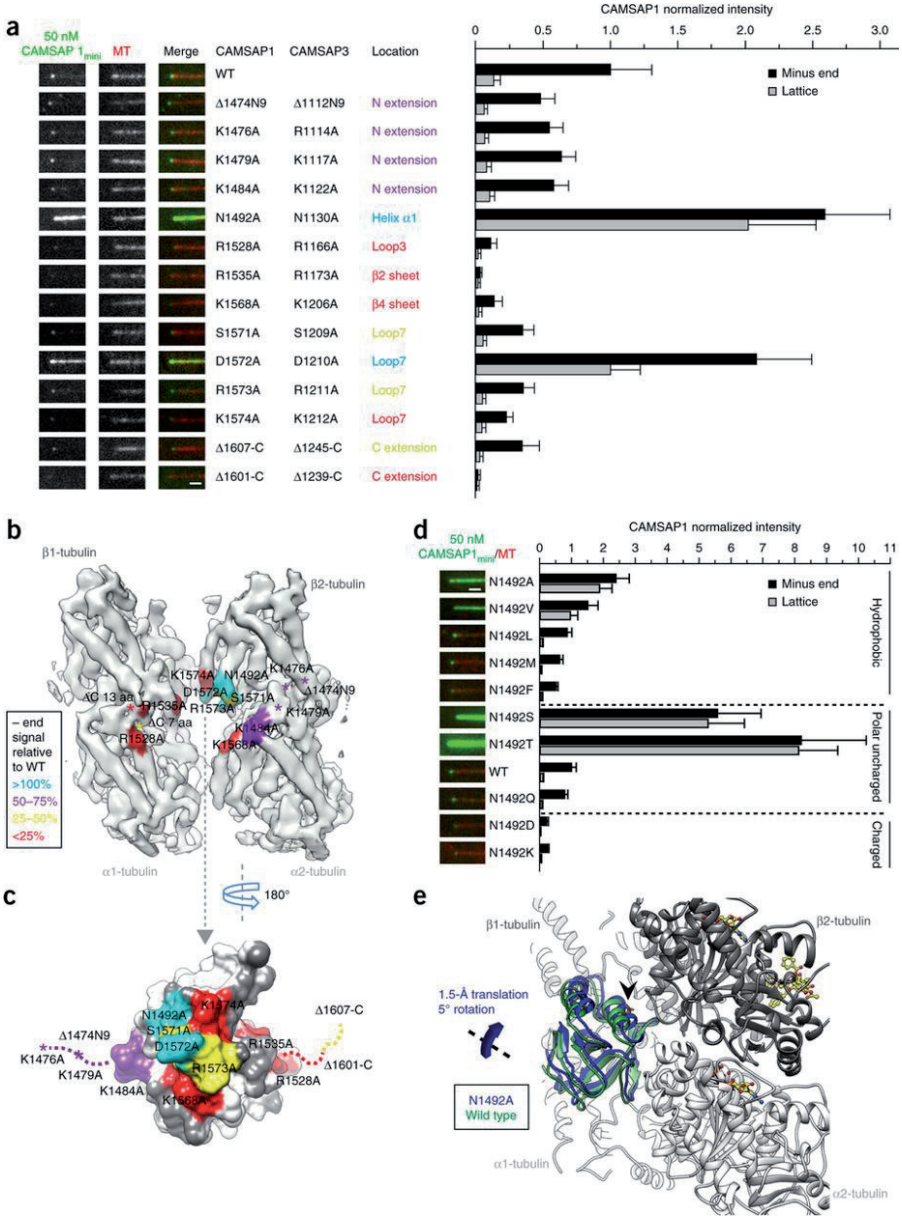

Figure 12. a) Left, TIRFM images of GFP-CAMSAP1$_{mini}$ wild type and mutants binding to the minus ends of dynamic MTs. Scale bar, 1 µm. The corresponding residues in CAMSAP3 and their locations are indicated. Right, quantification of GFP-CAMSAP1mini intensities at MT minus ends and on MT lattice. The intensity is normalized to the average minus-end intensity of wild type. Data are mean ± s.d.; n ranged from 17 to 87 MTs. b) View of the CKK-interaction surface of the MT cryo-EM density, with mutated CKK residues mapped (<8 Å distance) and

colored according to the percentage change in the minus-end fluorescence signal in mutants relative to wild type (as in a). c) Surface representation of the tubulin-interacting face of the CAMSAP1 CKK domain. Mutated CKK residues are colored according to the percentage change in the minus-end fluorescence signal of corresponding mutants relative to wild type in our TIRF assays (as in a). d) Left, TIRFM images of GFP-CAMSAP1$_{mini}$ N1492 mutants; scale bar, 1 µm. Right, quantification of GFP-CAMSAP1$_{mini}$ intensities at MT minus ends and on MT lattice. The intensity is normalized to the average minus-end intensity of wild type. Data are mean ± s.d.,n = 30 MTs. e) The N1492A CAMSAP1 CKK binds at the intradimer, interprotofilament MT binding site but in an orientation subtly different from that of wild type. Ribbon representation comparing the position of N1492A CAMSAP1 CKK with wild-type CAMSAP1 CKK relative to the tubulin-binding surface. N1492A CAMSAP1 CKK (blue) is rotated 5° around the indicated axis and translated 1.9 Å into the interprotofilament-binding site, relative to wild-type CAMSAP1 CKK (green). Arrowhead depicts the position of N1492.

We reasoned that understanding the mechanism underlying the higher affinity of the N1492A mutant for MTs would provide insight into CKK's minus-end specificity. Therefore, we obtained a 3D reconstruction of the CAMSAP1 CKK N1492A mutant by using cryo-EM (Figure 12e). As with the wild-type CKK, the N1492A mutant also binds at the tubulin intradimer B-lattice interface with the same overall orientation as the that of the wild-type CKK. However, two distinct structural properties were observed for the mutant compared with wild type: (i) less protofilament skew in CKK N1492A–decorated MTs (Figure 13) and (ii) a subtle shift of CKK N1492A itself toward the main MT body (Figure 12e). These results suggested that very small changes in the CKK–MT interaction determine the binding selectivity of CKK between the lattice and the minus end. Moreover, the adjustment in the CKK-MT interaction by the N1492A mutant-movement of the CKK domain deeper between protofilaments- may reflect aspects of the mechanism of end selectivity by wild-type CKK via selection of a tubulin conformation present only at MT minus ends.

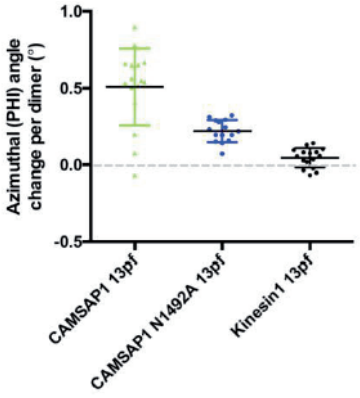

Figure 13. Protofilament skew for representative MTs. The reduced skew produced by CAMSAP1-N1492A CKK-decorated MTs are compared to wild type CKK MTs and control kinesin decorated paclitaxel-stabilized MTs.

The high-affinity CKK-binding site at MT minus ends

Having defined the CKK–MT binding mode, we set out to determine whether the state of MT minus ends affects CKK binding. We found that the binding of CAMSAP1mini to MT minus ends was insensitive to the nucleotide state of MTs, because the protein bound well to the minus ends of GMPCPP-stabilized (GTP like) or taxol-stabilized (GDP) MTs, as well as dynamic GTP or GTP-γS-bound (GDP-Pi like) MTs (Figure 14a,b). In contrast, we observed no accumulation of $CAMSAP1_{mini}$ at depolymerizing MT minus ends (Figure 14c), thus suggesting that their structure does not support CKK binding.

To determine the precise localization of CKK on MT minus ends, we implemented the model-convolution method[18] to determine the relative positions of the CKK and the MT minus end from their 1D intensity profiles along the MT axis (Figure 14d,e). Our data showed that CKK accumulated ~16 nm, equivalent to a few tubulin dimers, behind the outmost MT minus end (estimated measurement error of ~8 nm). This result suggested that some structural features of MT minus ends at this specific location form a preferred CKK-binding site.

Cryo-ET shows preserved interprotofilament contacts at MT ends

To gain insight into the structure of this binding site, we analyzed individual ends of GMPCPP-stabilized MTs by cryo-ET (Figure 14f). Because no averaging was imposed, the tomographic 3D reconstructions contain information about overall polymer configuration and thus allow for direct visualization of the conformation of tubulin that CKK recognizes. The data quality readily allowed for discrimination of individual protofilaments and in many cases individual subunits (Figure 14g), and provided critical 3D information about the MT ends. First, plots of individual protofilament trajectories at both plus and minus ends show a range of curvatures and lengths of curved regions (example of a minus end in Figure 14h). Second, although there is a wide variation of protofilament curvature, protofilaments at each end are on average less curved than in the model (Figure 14i,j). The minus- and plus-end protofilaments are similar with respect to the length (18 ± 15 nm and 11 ± 8 nm at the minus and plus ends, respectively) and the extent of longitudinal curvature, results consistent with those of previous

cryo-EM studies in 2D[19]. Hence, CKK minus-end preference does not depend on longitudinal curvature alone.

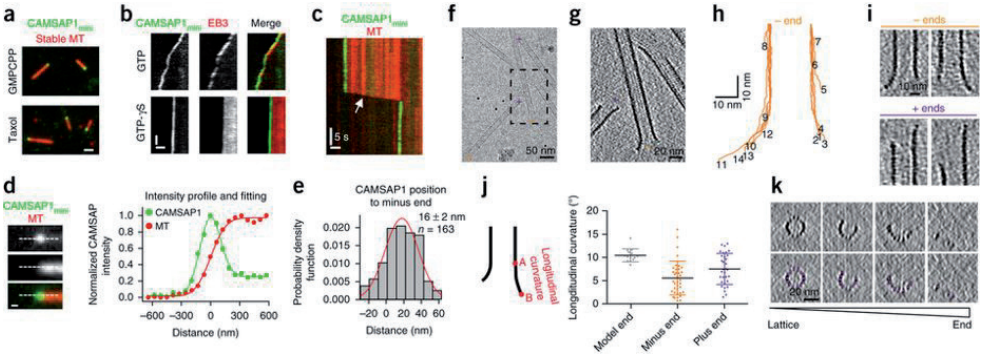

Figure 14. a) TIRFM images of the minus-end localization of GFP-CAMSAP1$_{mini}$ on GMPCPP or taxol-stabilized MTs. Scale bar, 1 µm. b) Kymographs showing that GFP-CAMSAP1$_{mini}$ tracks growing MT minus ends when MTs are polymerized in the presence of GTP or GTP-γS, whereas mCherry-EB3 decorates the entire lattice of GTP-γS MTs. Scale bars: horizontal, 1 µm; vertical, 30 s. c) Kymograph showing that GFP-CAMSAP1$_{mini}$ tracks a growing but not a depolymerizing MT minus end (white arrow). Scale bars: horizontal, 1 µm; vertical, 5 s. d) TIRFM image of rhodamine-labeled stable GMPCPP MT and CAMSAP1$_{mini}$-GFP. Normalized 1D intensity profiles of CAMSAP1$_{mini}$-GFP and MT and corresponding fitting of point-spread-function-convoluted models. To decrease the error introduced by the flexible linker between CKK and GFP, GFP was inserted at the CKK C terminus. Scale bar, 200 nm. e) Distribution of the position of CAMSAP1$_{mini}$-GFP relative to the MT minus end. Mean ± s.e.m. are shown; n = 163 MTs. f) Projection image from a cryo-ET tilt series showing *in vitro* GMPCPP-stabilized MTs, including several ends. The black dots are gold fiducials for tilt-series alignment. g) Longitudinal slice through MTs in the tomographic volume corresponding to the boxed region in f. h) 2D graphical representation of an exemplar minus end, plotting 3D protofilament radial trajectories. Here, for a 14-pf MT, 7 pf are plotted on either side, numbered around the circumference (pf14 is adjacent to pf1). i) Sagittal slices through tomographic volumes showing a range of curvatures and lengths at both ends. Some protofilaments terminate in the lattice before curvature is observed. j) Longitudinal curvature of ends. Left, schematic of longitudinal curvature A–B. Right, graph with only curved end regions longer than one dimer long plotted. Data show individual points, mean ± s.d.; model end (PDB 3JAT and 3RYH), n = 14 pf; plus end, n = 32 pf (5 MTs); minus end, n = 38 pf (5 MTs). Minus end versus plus end, not significant; model versus data, statistically significant ($P < 0.01$, Kolmogorov–Smirnov test). k) Series of transverse sections through an MT from lattice to end. Bottom panels show traced protofilament positions.

Intriguingly, adjacent protofilaments within an MT end retain connectivity with their neighbors (Figure 14k), even while the protofilaments spread away from the MT axis, and the total protofilament number is decreased. This behavior is in contrast to the MT-end model in which protofilament separation is an essential consequence of their curvature and is more consistent with the classical 'rams' horns' of depolymerizing MTs[19a], to which CAMSAP do not bind (Figure 14c). In other words, in nondepolymerizing MTs, protofilaments curving outward from the MT axis flatten from cylinders into gently curving

sheet-like structures, which retain lateral connectivity[19b]. Given that the CKK domain binds at the interprotofilament interface, the tomographic data suggest that potential CKK-binding sites are retained in the end structures characterized here. To determine whether CKK binding perturbs these curved sheet-like structures, we examined MT minus ends in the presence of CKK but detected no differences relative to the control MTs (Figure 15a–d). This analysis, when combined with our fluorescence-based localization of the CKK binding site, suggested that the CKK prefers neither the extreme end nor the MT lattice but a transition region from the straight lattice to a curved and flattened polymer.

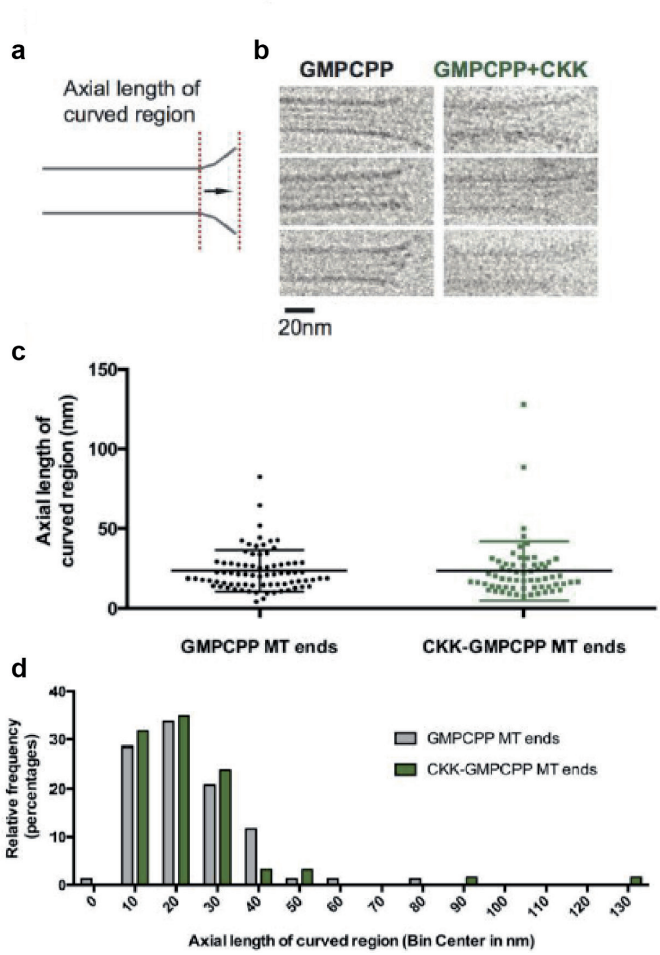

Figure 15. a) A scheme illustrating the curved region of a MT end in 2D. The measured axial length of the curved region is the distance between the two red dashed lines. b) Gallery of 2D projections of exemplar GMPCPP MT ends with or without 1.5 mg/ml CAMSAP3 CKK domain. Note similar end structures with moderate longitudinal

curvature, but also the much higher background in the presence of excess CKK protein. c) 2D quantification of the axial length of curved regions of GMPCPP MT ends (as shown in panel a) in the presence or absence of CAMSAP3 CKK domain. No significant difference is observed with added CKK domain, two-tailed Mann-Whitney U test. For GMPCPPMT ends, n=77 MT ends; for CKK-GMPCPP-MT ends, n=63 MT ends. Data represent mean ± SD. d) A histogram of axial length of curved regions of GMPCPP MT ends shows similar length distributions in the presence or absence of CAMSAP3 CKK domain. In both cases, the most common bin center of end lengths is 20 nm (bin width 10 nm).

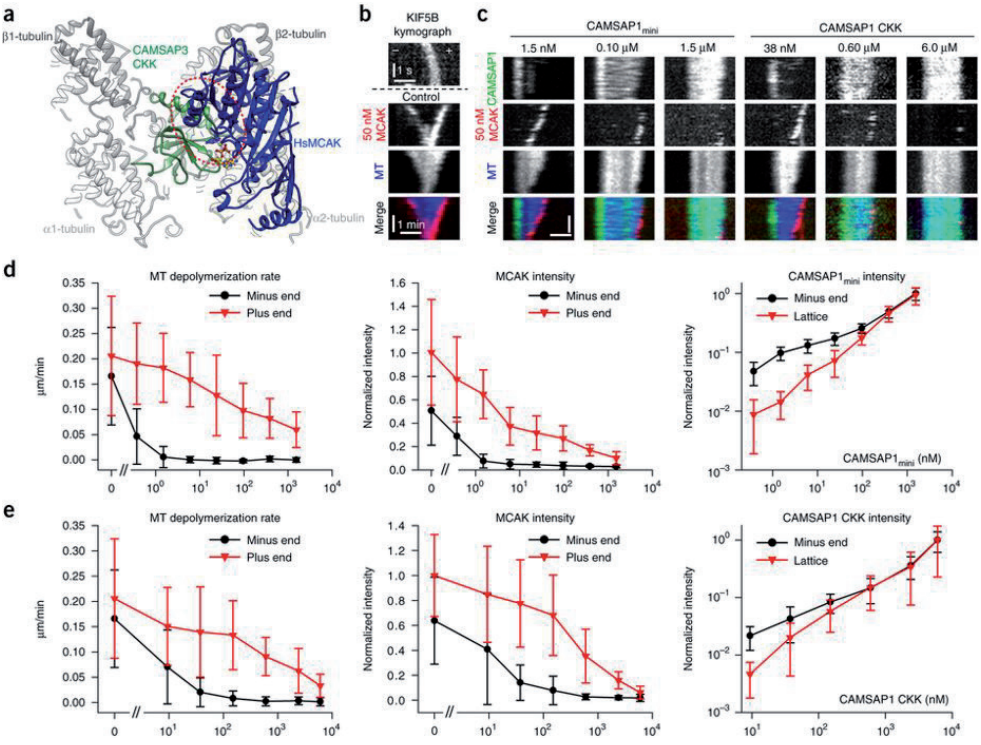

Figure 16. a) An MT tubulin dimer pair bound to CAMSAP3 CKK (green), shown with the expected position of an MD of HsMCAK (in complex with ADP; PDB 4UBF) by alignment with MT-bound kinesin-1[20]. b) Kymographs of MT-depolymerization assay with GMPCPP-stabilized MTs (blue) and GFP-MCAK (red). Scale bars: horizontal, 1 µm; vertical, 1 s (top) or 1 min (bottom). MT polarity was determined on the basis of the movement of the SNAP-Alexa647-tagged plus end-directed motor kinesin-1 KIF5B (green, residues 1–560). c) Kymographs of MT-depolymerization assays with GMPCPP-stabilized MTs (blue), GFP-MCAK (red) and different concentrations of SNAP-Alexa647-tagged CAMSAP1$_{mini}$ or CKK (green). Scale bars: horizontal, 1 µm; vertical, 1 min. In b and c, MT minus (−) ends are shown on the left, and plus (+) ends are shown on the right. d,e) Quantification of MT-depolymerization rate, MCAK intensity and CAMSAP1 intensity at different concentrations of CAMSAP1$_{mini}$ (d) or CKK (e).

CKK blocks MCAK interaction with MT minus ends

Fly Patronin and three mammalian CAMSAPs have been shown to protect MT minus ends from depolymerization by kinesin-13[10, 21], but the underlying mechanism is unknown. By superimposing the human (Hs) MCAK motor structure onto our CKK–MT cryo-EM reconstruction, we found that CKK and HsMCAK would strongly clash with each other at a number of positions (Figure 16a). Hence, CKK and MCAK would be expected to compete for the binding sites at MT minus ends. To test this hypothesis, we measured *in vitro* disassembly of GMPCPP-stabilized MTs by 50 nM MCAK in the presence of different concentrations of CAMSAP1$_{mini}$ or the isolated CKK domain (Figure 16b,c). CAMSAP1$_{mini}$ and CKK almost completely inhibited the minus-end binding and depolymerization of MCAK at 1.5 nM and 38 nM, respectively, whereas the activity of MCAK on plus ends was largely unaffected at those concentrations (Figure 16d,e). Above 1 µM concentration, even though both CAMSAP1mini and CKK fully decorated the MT shaft with lattice intensities higher than those observed at the minus ends at low concentrations, this decoration did not lead to complete inhibition of MT plus-end accumulation and depolymerization by MCAK (Figure 16d,e). This observation suggested that the CKK has the highest affinity for MT minus ends and then for the MT lattice, and has the lowest affinity for MT plus ends. The alternative mechanism-in which displacement of MCAK from MT minus ends is due to CKK-mediated alteration of the MT minus-end structure, which would be less favorable for MCAK binding-is not supported by our cryo-EM images even at a CKK concentration of >50 µM, which was much higher than the concentrations used in our in vitro assays (Figure 15a–d). This result indicated that the competition between CKK and MCAK on MT minus ends is primarily based on steric hindrance.

Discussion

In this study, we demonstrated that the CKK is a highly conserved globular-protein module. Using a combination of solution-state NMR and X-ray crystallography techniques, the structure of mammalian was solved that includes two α-helices and five-stranded β-sheet as well as unstructured termini. By using ssNMR and comparing the chemical-shift correlation patterns of ssNMR data

obtained of CAMSAP3 CKK in complex with MTs to data obtained using solution-state NMR assignments of free CAMSAP3 CKK in solution, we could map the binding interface of CKK interaction with MTs. Cryo-EM showed that CKK interacts with an interprotofilament site between two tubulin dimers on the outer surfaces of MTs. Several lines of evidence suggest that an optimal site for CKK binding deviates from the interprotofilament interface within a regular, straight MT structure. First, the decoration by CKK distorts the normal MT lattice, thereby generating a right-handed protofilament skew. Second, tubulin copolymerization with CKK yields mainly non-MT, curved polymers. Third, the interaction between CKK and its binding site is intrinsically asymmetric, with the helical parts of CKK interacting more closely with the β-tubulin pairs, whereas its connectivity with the α-tubulin pair is less compact and is able to accommodate plasticity at minus ends. Fourth, the N1492A mutation increases affinity and subtly alters the CKK position relative to the MT, thus resulting in a deeper insertion between the protofilaments. The size and the chemical nature of the N1492-substituted side chain also affect CKK affinity for the MT lattice, thus suggesting that the optimal binding site for the wild-type CKK domain might depend on specific but subtle conformational features of tubulin dimers at MT minus ends to allow for a more buried fit between protofilaments. Fifth, high-resolution microscopy showed that the high-affinity CKK-binding region is located, on average, two tubulin dimers behind the outmost MT end. This binding site fits very well with the average position of the transition zone between the straight protofilaments in the MT shaft and the mildly curved tubulin sheets identified at MT ends by cryo-ET.

At this transition zone, pairs of α-tubulins would be more laterally flattened and more flexible than the more constrained lattice-like β-tubulin pairs (Figure 17a). In agreement with this scenario, our structures show that the lattice-bound CKK has tight shape complementarity and a large contact surface with the β-tubulin pairs, whereas the α-tubulin pairs surround the CKK more loosely. In contrast, at the plus end, β-tubulin pairs are expected to acquire a more flattened and flexible arrangement than α-tubulins. This arrangement would disfavor the interaction of CKK with the plus end, thereby explaining its inability to effectively compete with MCAK at this location. In summary, flattening of β-tubulin pairs at the plus end may squeeze CKK out of the tubulin groove, thus avoiding steric clashes, whereas flattening of α-tubulin pairs at the

minus end may tighten their multiple contacts around the CKK. This tightening would lead to a binding preference for the minus end, some capacity to bind the straight MT lattice and low affinity for MT plus end. The lack of CKK binding at rapidly depolymerizing MT minus ends, where the lateral contacts between protofilaments are expected to be lost, owing to their strong curling, is consistent with the requirement for maintenance of lateral protofilament connectivity and/or more gentle longitudinal curvature for CAMSAP binding.

Importantly, although our analysis showed that CKK was the only CAMSAP part able to autonomously recognize MT minus ends, some longer CAMSAP fragments, such as CAMSAP1$_{mini}$, had a higher affinity for the minus ends. These data indicated that CAMSAP regions outside of the CKK domain contribute to the affinity and selectivity of minus-end binding, and additional work will be needed to decipher the underlying mechanisms.

The MT minus-end-binding mode of the CKK domain is distinct from those of other known MT-tip-interacting proteins. The most conceptually simple mode of MT-end recognition relies on the presence of unique binding sites on α- and β-tubulin exposed on the outermost MT ends, as is the case for the γ-TuRC at the minus end[3] and probably for the centriole protein CPAP at MT plus ends[22]. However, the preference of most known MT regulators is based on recognition of certain MT-lattice features that are different at MT ends compared with the MT shaft. For example, EB proteins bind at the vertex of four tubulin dimers[23] and sense a GTP-hydrolysis transition state of tubulin within the MT lattice at both plus and minus ends[24]. Doublecortin, which also binds at the vertex of four tubulin dimers[25] and acts as an MT-end-binding protein, is thought to be sensitive to the extent of protofilament longitudinal curvature[26]. MT-depolymerizing kinesin-13s can also accumulate at MT ends, probably because of a preference for the more curved or flexible conformations of tubulin located outside the lattice[27]. Importantly, none of these mechanisms are specific for the plus or the minus end.

CAMSAPs are similar to most other MT-end-binding proteins in that they bind on the outer surfaces of MTs: in contrast to γ-TuRC binding, which caps MTs, CAMSAP binding is compatible with further MT polymerization at the minus end[7]. CAMSAPs and γ-TuRCs thus do not directly compete for binding to MT

minus ends; however, the restricted lattice-like conformation of tubulin at γ-TuRC-capped minus ends probably prevents formation of CAMSAP-preferred binding regions. Importantly, in contrast to EB-MT association, CAMSAP-MT association is insensitive to the hydrolysis state of the tubulin-bound nucleotide. Whereas the tubulin interdimer interface to which EBs bind changes conformation in response to nucleotide, the intradimer interface to which CKKs bind does not[23b, 28]. This difference in conformational changes accounts for the ability of CAMSAPs to recognize growing GTP- as well as GDP-bound minus ends generated by MT severing[7].

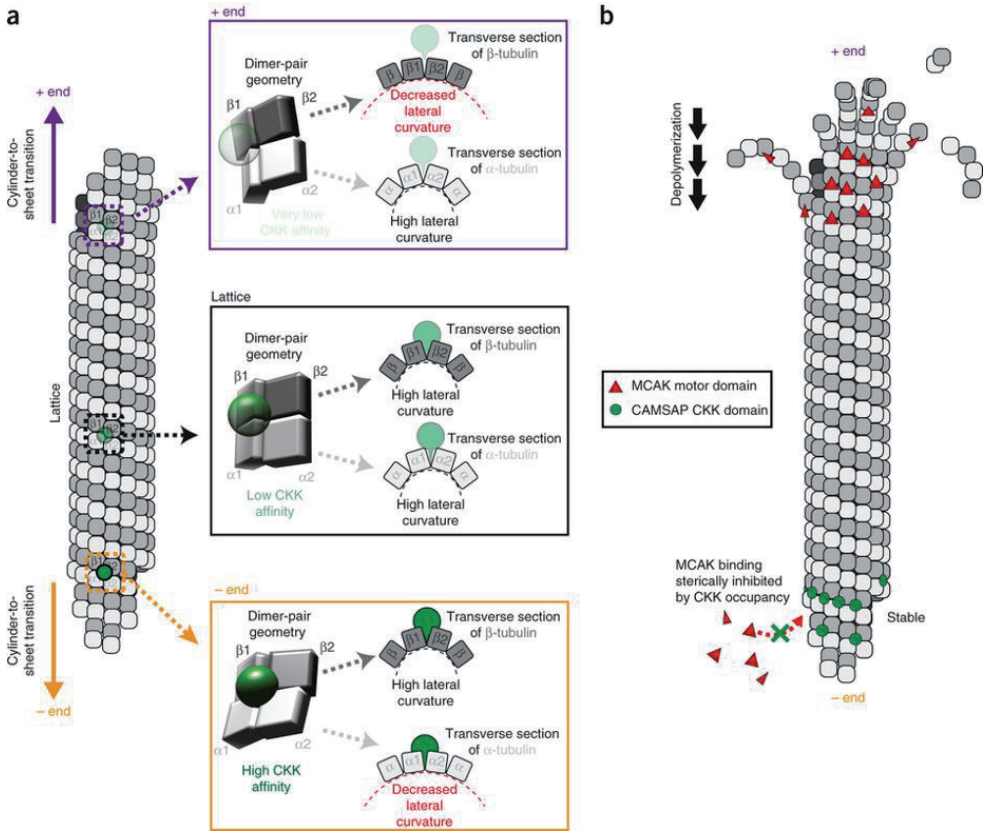

Figure 17. a) Proposed mechanisms of MT minus-end binding and protection from MCAK-induced depolymerization by the CKK domain. a) Toward the ends of stable or growing MTs, there is a transition from the regular lattice to sheet-like regions, with increasing longitudinal curvature and decreasing lateral curvature. Protofilaments retain lateral connectivity, and thus interprotofilament CKK-binding sites are preserved. Given the polar nature of MTs, these lattice-to-sheet transitions create unique conformations of B-lattice tubulin dimer pairs at either end of the MT: at the minus end, α-tubulins in dimer pairs are more flattened than β-tubulins, whereas the opposite is true at the plus end. In this way, we propose that the unique dimer-pair conformation at the minus end, compared with dimer-pair conformations in the lattice or at the plus end, favors

CKK binding. b) Model of minus-endspecific protection from MCAK-induced depolymerization by the CKK domains. CKKs (green circles) specifically bind to a curved minus-end region, and steric inhibition thereby prevents the association of MCAK motor domains (red triangles) with the same region. Because the CKKs do not bind to the corresponding region of the plus end, MCAK is free to bind and depolymerize from the plus end.

CAMSAP's interaction with MT minus ends can be expected to have several consequences. First, by preferentially binding between laterally connected but curved protofilaments, the CKK, in the context of the full-length protein, might inhibit formation of a regular lattice, thus explaining why CAMSAPs slow down MT minus-end polymerization[7]. Second, CKK binding at intradimer-binding sites can also explain the protection of MT minus ends from kinesin-13-driven depolymerization by direct steric inhibition (Figure 17b).

Together, our data show that the unique MT-binding mode of the CKK domains enables CAMSAPs to combine the ability to recognize MT minus ends with the preservation of the dynamic properties of these ends. Hence, CAMSAPs can be rapidly recruited to MT minus ends generated by release from the sites of MT nucleation, severing or breakage, and consequently protect the ends from disassembly by depolymerases and, by decorating polymerizing minus ends, form stretches of stabilized MT lattice. Future studies will show whether other proteins share the CKK's MT-binding mode or whether this mode is unique to this evolutionarily ancient and widespread protein module.

References:

[1] A. Akhmanova, M. O. Steinmetz, *Nature Reviews Molecular Cell Biology* **2015**, *16*, 711.

[2] A. Akhmanova, Casper C. Hoogenraad, *Current Biology* **2015**, *25*, R162-R171.

[3] J. M. Kollman, A. Merdes, L. Mourey, D. A. Agard, *Nature Reviews Molecular Cell Biology* **2011**, *12*, 709.

[4] E. Derivery, C. Seum, A. Daeden, S. Loubéry, L. Holtzer, F. Jülicher, M. Gonzalez-Gaitan, *Nature* **2015**, *528*, 280.

[5] M. Toya, S. Kobayashi, M. Kawasaki, G. Shioi, M. Kaneko, T. Ishiuchi, K. Misaki, W. Meng, M. Takeichi, *Proceedings of the National Academy of Sciences* **2016**, *113*, 332.

[6] a) M. Chuang, A. Goncharov, S. Wang, K. Oegema, Y. Jin, Andrew D. Chisholm, *Cell Reports* **2014**, *9*, 874-883; b) Kah W. Yau, Sam F. B. van Beuningen, I. Cunha-Ferreira, Bas M. C. Cloin, Eljo Y. van Battum, L. Will, P. Schätzle, Roderick P. Tas, J. van Krugten, Eugene A. Katrukha, K. Jiang, Phebe S. Wulf, M. Mikhaylova, M. Harterink, R. J. Pasterkamp, A. Akhmanova, Lukas C. Kapitein, Casper C. Hoogenraad, *Neuron* **2014**, *82*, 1058-1073.

[7] K. Jiang, S. Hua, R. Mohan, I. Grigoriev, Kah W. Yau, Q. Liu, Eugene A. Katrukha, A. F. M. Altelaar, Albert J. R. Heck, Casper C. Hoogenraad, A. Akhmanova, *Developmental Cell* **2014**, *28*, 295-309.

[8] N. Tanaka, W. Meng, S. Nagae, M. Takeichi, *Proceedings of the National Academy of Sciences* **2012**, *109*, 20029.

[9] A. J. Baines, P. A. Bignone, M. D. A. King, A. M. Maggs, P. M. Bennett, J. C. Pinder, G. W. Phillips, *Molecular Biology and Evolution* **2009**, *26*, 2005-2014.

[10] M. C. Hendershott, R. D. Vale, *Proceedings of the National Academy of Sciences* **2014**, *111*, 5860.

[11] a) S. Grzesiek, A. Bax, *Journal of Magnetic Resonance (1969)* **1992**, *96*, 432-440; b) E. T. Olejniczak, R. X. Xu, S. W. Fesik, *Journal of Biomolecular NMR* **1992**, *2*, 655-659; c) S. Grzesiek, A. Bax, *Journal of Biomolecular NMR* **1993**, *3*, 185-204.

[12] M. Baldus, A. T. Petkova, J. Herzfeld, R. G. Griffin, *Molecular Physics* **1998**, *95*, 1197-1207.

[13] K. Seidel, A. Lange, S. Becker, C. E. Hughes, H. Heise, M. Baldus, *Physical Chemistry Chemical Physics* **2004**, *6*, 5090-5093.

[14] J. Atherton, K. Jiang, M. M. Stangier, Y. Luo, S. Hua, K. Houben, J. J. E. van Hooff, A.-P. Joseph, G. Scarabelli, B. J. Grant, A. J. Roberts, M. Topf, M. O. Steinmetz, M. Baldus, C. A. Moores, A. Akhmanova, *Nature Structural &Amp; Molecular Biology* **2017**, *24*, 931.

[15] Y. Shen, F. Delaglio, G. Cornilescu, A. Bax, *Journal of Biomolecular NMR* **2009**, *44*, 213-223.

[16] Max A. Tischfield, Elizabeth C. Engle, *Bioscience Reports* **2010**, *30*, 319.

[17] E. Nogales, R. Zhang, *Current Opinion in Structural Biology* **2016**, *37*, 90-96.

[18] a) M. K. Gardner, B. L. Sprague, C. G. Pearson, B. D. Cosgrove, A. D. Bicek, K. Bloom, E. D. Salmon, D. J. Odde, *Cellular and Molecular Bioengineering* **2010**, *3*, 163-170; b) Sebastian P. Maurer, Nicholas I. Cade, G. Bohner, N. Gustafsson, E. Boutant, T. Surrey, *Current Biology* **2014**, *24*, 372-384.

[19] a) E. M. Mandelkow, E. Mandelkow, R. A. Milligan, *The Journal of Cell Biology* **1991**, *114*, 977; b) D. Chrétien, S. D. Fuller, E. Karsenti, *The Journal of Cell Biology* **1995**, *129*, 1311.

[20] J. Atherton, I. Farabella, I. M. Yu, S. S. Rosenfeld, A. Houdusse, M. Topf, C. A. Moores, *eLife* **2014**, *3*, e03680.

[21] S. S. Goodwin, R. D. Vale, *Cell* **2010**, *143*, 263-274.

[22] A. Sharma, A. Aher, Nicola J. Dynes, D. Frey, Eugene A. Katrukha, R. Jaussi, I. Grigoriev, M. Croisier, Richard A. Kammerer, A. Akhmanova, P. Gönczy, Michel O. Steinmetz, *Developmental Cell* **2016**, *37*, 362-376.

[23] a) Sebastian P. Maurer, Franck J. Fourniol, G. Bohner, Carolyn A. Moores, T. Surrey, *Cell* **2012**, *149*, 371-382; b) R. Zhang, Gregory M. Alushin, A. Brown, E. Nogales, *Cell* **2015**, *162*, 849-859.

[24] M. Zanic, J. H. Stear, A. A. Hyman, J. Howard, *PLOS ONE* **2009**, *4*, e7585.

[25] F. J. Fourniol, C. V. Sindelar, B. Amigues, D. K. Clare, G. Thomas, M. Perderiset, F. Francis, A. Houdusse, C. A. Moores, *The Journal of Cell Biology* **2010**, *191*, 463.

[26] S. Bechstedt, K. Lu, Gary J. Brouhard, *Current Biology* **2014**, *24*, 2366-2375.

[27] a) A. Desai, S. Verma, T. J. Mitchison, C. E. Walczak, *Cell* **1999**, *96*, 69-78; b) C. A. Moores, M. Yu, J. Guo, C. Beraud, R. Sakowicz, R. A. Milligan, *Molecular Cell* **2002**, *9*, 903-909.

[28] Gregory M. Alushin, Gabriel C. Lander, Elizabeth H. Kellogg, R. Zhang, D. Baker, E. Nogales, *Cell* **2014**, *157*, 1117-1129.

CHAPTER 3

3

Structural determinants of microtubule minus end preference in CAMSAP CKK domains

Joseph Atherton, Yanzhang Luo, Shengqi Xiang, Chao Yang, Kai Jiang, Marcel Stangier, Annapurna Vemu, Alex Cook, Su Wang, Antonina Roll-Mecak, Michel O. Steinmetz, Anna Akhmanova, Marc Baldus, and Carolyn A. Moores

Adapted from manuscript under revision.

Abstract

CAMSAP/Patronins regulate microtubule minus-end dynamics. Their end specificity is mediated by their CKK domains, which we proposed recognize specific tubulin conformations found at minus ends. To critically test this idea, we compared the human CAMSAP1 CKK domain (HsCKK) with a CKK domain from *Naegleria gruberi* (NgCKK), which has lost minus-end specificity. Near-atomic cryo-electron microscopy structures of HsCKK- and NgCKK-microtubule complexes show that these CKK domains share the same protein fold, bind at the intradimer interprotofilament tubulin junction, but exhibit subtly different footprints on microtubules. Whereas NgCKK binding does not alter the microtubule architecture, HsCKK remodels its microtubule interaction site and changes the underlying polymer structure because the tubulin lattice conformation is not optimal for its binding. NMR experiments show that HsCKK is remarkably rigid, supporting this remodelling ability. Thus, in contrast to many MAPs, CKK domains can differentiate subtly specific tubulin conformations to enable microtubule minus-end recognition.

Introduction

The involvement of the microtubule (MT) cytoskeleton in numerous processes in eukaryotic cells is enabled by the diverse and adaptable properties of individual MTs. MTs act as tracks for molecular motors, while growing and shrinking MTs can be used to generate force. MTs can also act as signalling hubs, such that specific tubulin conformations within particular regions of the polymer stimulate recruitment of distinct MT binding partners. The molecular basis of these effects, mediated by the conformational adaptability of tubulin dimers, is only just beginning to be understood and represents a key topic in the cytoskeleton field.

The ends of MTs are important sites of conformational diversity and are often points of communication between the MT cytoskeleton and other cellular components, such as membranes, organelles, centrosomes and chromosomes[1]. The exact conformation(s) of MT ends is an ongoing source of debate, but current evidence points to their being composed of zones with distinct and dynamic

tubulin conformations[2]. MT minus ends were long thought to be static and structurally homogeneous, capped by γ-TuRCs and buried at MT organizing centres. More recently however, the discovery and characterization of CAMSAP (calmodulin-regulated spectrin-associated proteins)/Patronin family members has revealed that control of non-centrosomal MT minus-end dynamics, and their interaction with specific cellular regions, are vital in numerous aspects of cell physiology[3]. CAMSAP/Patronins are centrally involved in diverse activities including promoting cell polarity, regulation of neuronal differentiation and axonal regeneration, and definition of spindle organization and asymmetry, thereby highlighting the importance of regulation of MT minus-end dynamics in these varied contexts[4].

At the molecular level, CAMSAPs/Patronins stabilize uncapped MT minus ends and support MT minus-end growth[5]. CAMSAP/Patronins are large, multi-domain proteins with many cellular binding partners. However, the family is defined by the presence of a CKK domain (originally identified in CAMSAP1, KIAA1078 and KIAA1543) which is necessary and sufficient for MT minus-end binding in many CAMSAP/ Patronins[6]. Previously, we showed that CAMSAP/Patronin CKK domains preferentially bind to a zone behind the extreme MT minus end which corresponds to a region where the lattice undergoes a transition to gently curved tubulin sheets[2b]. Solid-state NMR (ssNMR) and subnanometer resolution single particle cryo-EM showed that CKK domains bind on the MT lattice between two tubulin dimers on adjacent protofilaments. Mutagenesis of residues at the MT-binding interface in the CKK domain disrupted lattice and minus end binding, showing that the same regions of the CKK domain that contact the MT are also involved in binding to the minus-end zone. Taking these data together, we proposed a model for CAMSAP/Patronin MT minus end recognition, which is mediated by sensitivity of the CKK domain to a curved sheet-like conformation of tubulin exclusive to MT minus ends. Specifically, the model suggests that the tighter CKK interaction with β-tubulin disfavours binding at MT plus ends while the looser α-tubulin contacts preferentially accommodate tubulin curvature at minus ends. This interaction also can occur on the MT lattice, but CKK binding induces distortion of the non-optimal binding site configuration, manifesting as protofilament skew within the polymer.

Despite these findings, several critical questions relating to the structural basis of this recognition mechanism remain unanswered: How is the CKK-induced MT lattice distortion accommodated, and what can this tell us about minus-end recognition? Can CKK binding to different MT protofilament architectures shed further light on the mechanism of minus end recognition? Intriguingly, we also previously identified CKKs in the amoeboflagellate *N. gruberi* and the potato blight fungus *P. infestans* that had lost the binding preference for MT minus ends that was proposed to be present in CKK domains from the last eukaryotic common ancestor. Can a comparison of CKK domains with and without minus-end binding specificity also provide insight into MT minus-end recognition? Since discrimination between different MT lattice zones can depend on relatively subtle structural differences, high-resolution information is needed to address these questions. It is currently not possible to image MT minus ends directly at the necessary resolution to observe these conformational variations. However, our previous work showed that CKK lattice binding can be used as a proxy for minus end binding, and cryo-EM studies of the lattice could yield near-atomic resolution information about the CKK-tubulin complex. In addition, high-resolution NMR measurements can provide residue-specific information that allows studying local environment changes and interaction dynamics of CKK domains in complex with MTs at the atomic level.

In order to answer these questions, we carried out high-resolution, ^{1}H-detected ssNMR study on the previously characterized human CAMSAP1 CKK (HsCKK) N1492A mutant to obtain further structural details. Solution-state NMR data on different mammal CKK variants revealed their distinctive rigidity that supports the ability of HsCKK to remodel MTs. HsCKK-induced skew arises within the MT lattice from the tilting of entire protofilaments coincidental with contraction of the MT diameter. We also investigated the CKK domain from *Naegleria gruberi* (NgCKK), which does not show minus-end binding preference. The direct comparison of tubulin binding by NgCKK with that of human CAMSAP1 CKK (HsCKK) - which has minus end binding preference - allowed us to probe our previous model of minus-end recognition. NgCKK binding does not induce the protofilament skew that HsCKK binding produces, reinforcing that induction of skew is a structural signature for minus-end binding capability.

Materials and Methods

Protein preparations for NMR. Human CAMSAP1 N1492A CKK (residues 1474-1613) was cloned into a pET28a vector. For sample preparation of standard MAS ssNMR, uniformly [^{13}C, ^{15}N]-labeled CAMSAP1 N1492A CKK was produced in *E. coli* strain Rosetta 2 in M9 minimum medium supplemented with 25 µg/ml kanamycin and 35 µg/ml chloramphenicol. Cells were induced when the OD_{600} reached 0.6 with 0.3 mM IPTG at 25 °C for 5 hrs. For ^{1}H detected ssNMR experiments, uniformly [^{2}H, ^{13}C, ^{15}N]-labeled CKK mutant was produced in *E.coli* Rosetta 2 strain in M9 minimum medium that was prepared with D_2O, deuterated ^{13}C-glucose and ^{15}N-NH_4Cl. When OD_{600} reached 0.6, 0.3 mM IPTG was added for induction at 25 °C for 5 hrs. The proteins were purified by a ÄKTA pure system with a POROS™ MC column that was saturated with Ni^{2+}. The column was first equilibrated with washing buffer (50 mM phosphate buffer, pH 8, 200 mM NaCl, 1 mM β-mercaptoethanol and 20 mM imidazole). Proteins were eluted with the same buffer but containing 400 mM imidazole. Proteins were then loaded onto a SEC HiLoad Superdex 75 26/60 column (GE Healthcare) that was equilibrated with 40 mM phosphate buffer, pH 7, supplemented with 150 mM NaCl and 1 mM DTT. Subsequently, the labeled proteins were concentrated and used for ssNMR sample preparation.

To prepare CKK-MT complexes for standard-speed MAS ssNMR, 20 mg of lyophilized porcine tubulin was dissolved in BRB80 buffer to a final concentration of 2 mg/ml. Microtubule polymerization was done with 1 mM GTP and addition of 20 µM paclitaxel (Sigma) for 30 min at 30 °C. Paclitaxel-stabilized MTs were pelleted down at 180,000 x g (Beckman TLA-55 rotor) at 30 °C for 30 min and resuspended in warm BRB80 buffer with 20 µM paclitaxel. [^{13}C, ^{15}N]-labeled CKK N1492A was then added to a final concentration of 65.3 µM (4:1 CKK/tubulin) and incubated at 37 °C for 30 min. The pellet was centrifuged down at 180,000 × g (Beckman TLA-55 rotor) at 30 °C for 30 min and washed with 40 mM phosphate buffer, pH 7, without disturbing the pellet. The pellet was then transferred and packed into a 3.2 mm rotor.

To prepare the CKK-MTs complexes for ^{1}H detected experiments, uniformly [^{2}H, ^{13}C, ^{15}N]-labeled CKK was first purified and kept in the protonated buffer overnight to allow back-exchange of amide protons. 5 mg of lyophilized

porcine brain tubulin was dissolved in 2.5 mL BRB80 buffer to obtain a concentration of 2 mg/mL. Tubulin was then polymerized with 1 mM GTP and 20 µM paclitaxel for 30 min at 30 °C. Paclitaxel-stabilized MTs were then ultracentrifuged at 180,000 × g at 30°C for 30 min and then resuspended with warm BRB80 buffer with 20 µM paclitaxel. The CKK domain was added to the resuspended MTs and incubated at 37°C for 30 min. The CKK-MTs complexes were then ultracentrifuged at 180,000 × g at 30°C for 30 min. Finally, the pellet was washed with phosphate buffer and packed into a 1.3 mm MAS NMR rotor.

For sample preparation for solution-state NMR, uniformly [^{13}C, ^{15}N]-labeled and ^{15}N-labeled CAMSAP1 N1492A CKK were expressed and purified as described above and supplemented with 5% D_2O for solution-state NMR measurements.

NMR experiments and data analysis. Resonance assignments of CAMSAP1 CKK N1492A were obtained from standard solution-state NMR experiments (2D HSQCs, 3D HNCA, HNCO, HNCACB, CBCA(CO)NH) on free [^{13}C, ^{15}N]-labeled CKK recorded on a 600 MHz spectroscopy (Bruker Biospin). Standard MAS ssNMR experiments were conducted on a 950 MHz standard-bore spectrometer (Bruker Biospin) equipped with a 3.2 mm triple-channel MAS HCN probe. The experiments include 2D ^{13}C-^{13}C proton-driven spin-diffusion (PDSD)[7] and NCA experiments[8] (set temperature 260 K, MAS rate 14 kHz). The spin diffusion mixing time was set to 30 ms, and a SPECIFIC-CP[9] transfer time of 2.2 ms was employed for the NCA experiment. Fast MAS, ^{1}H detected ssNMR experiments were performed on an 800 MHz wide-bore spectrometer (Bruker Biospin) equipped with a 1.3 mm triple-channel MAS HXY probe. The experiments include 2D NH and 3D CANH[10] (set temperature 244 K, MAS rate 55 kHz). ssNMR MT samples were stable over time as confirmed by comparing ssNMR spectra at low and fast MAS and by conducting negative staining EM experiments before and after ssNMR measurements (see Chapter 5).

CPMG relaxation dispersion[11] and CEST measurements[12] were based on the 2D ^{1}H-^{15}N HSQC spectra and were recorded as pseudo 3D on the ^{15}N-labeled CAMSAP1 N1492A CKK. The acquisition times in each 2D plane are 66 ms for ^{1}H (direct dimension) and 48.6 ms for ^{15}N (indirect dimension). CPMG relaxation

dispersion experiments were conducted with temperature compensation and single scan interleaved. The data were measured at CPMG fields of 50, 150, 250, 350, 450, 550, 650, 750, 850, 950, 1050, 1150, 1250, 1400 and 1500 Hz, which all applied for a constant transverse relaxation time of 40 ms. The saturation during CEST experiments were carried out with 400 ms of 15 Hz fields on ^{15}N. The saturation offsets ranged between 8200 and 6325Hz with a spacing of 25 Hz on ^{15}N.

The difference of chemical-shift values between the free- and bound-state CKK on both ^{1}H and ^{15}N dimensions were first measured in ppm and then were combined as $\sqrt{(\Delta N * 0.15)^2 + \Delta H^2}$ ref[13]. The signal linewidth in ^{1}H and ^{15}N dimensions were determined to amount to 0.1 and 0.6 ppm, respectively.

CMPG data were processed as follows: For each residue, the standard deviation and the average of signal intensities with different CPMG frequencies were calculated. The ratio of these two values is plotted for every residue on the structures.

For determining chemical-shift changes between free and MT bound CAMSAP1 CKK and CAMSAP1 CKK N1492A we transferred solution-state NMR shifts obtained on the free variants to ssNMR experiments on the complexes assuming spectral proximity in three independent dimensions (HN, N, Cα). With this strategy, we were able to transfer 48 backbone assignments as demonstrated in Figure 2d.

Protein expression and purification for TIRF Microscopy. Strep-GFP-tagged human CAMSAP1 CKK (residues 1474-C) and *Naegleria gruberi* CKK (residues 612-C, reference sequence XM_002675733.1) were prepared as described previously. Briefly, both proteins were expressed in HEK293T cells using a modified pTT5 expression vector (Addgene no. 44006), purified using StrepTactin beads (GE) and eluted in elution buffer (50 mM HEPES, 150 mM NaCl, 1mM $MgCl_2$, 1mM EGTA, 1mM dithiothreitol (DTT), 2.5 mM d-Desthiobiotin and 0.05% Triton X-100, pH 7.4). Purified proteins were snap-frozen and stored at -80 °C.

TIRF microscopy analysis of CKK binding to dynamic MTs. TIRF microscopy was performed on an inverted research microscope Nikon Eclipse Ti-E (Nikon) with the perfect focus system (PFS) (Nikon), equipped with a Nikon CFI Apo TIRF 100×1.49-NA oil objective (Nikon) and a Photometrics Evolve 512 EMCCD (Roper Scientific) camera, and controlled with MetaMorph 7.7 software (Molecular Devices). Images were projected onto the chip of an Evolve 512 camera with an intermediate 2.5× lens (Nikon C mount adaptor 2.5×). To keep in vitro samples at 30 °C, we used an INUBG2E-ZILCS (Tokai Hit) stage-top incubator.

For excitation, we used 491 nm/100 mW Stradus (Vortran) and 561 nm/100 mW Jive (Cobolt) lasers. For simultaneous imaging of green and red fluorescence, we used a triple-band TIRF polychroic filter (ZT405/488/561rpc, Chroma) and triple-band laser emission filter (ZET405/488/561m, Chroma), mounted in the metal cube (91032, Chroma) together with an Optosplit III beam splitter (Cairn Research) equipped with a double-emission-filter cube configured with ET525/50m, ET630/75m and T585LPXR (Chroma) filters.

Doubly cycled GMPCPP-stabilized MT seeds were prepared by incubating the tubulin mix containing 70% unlabeled porcine brain tubulin (Cytoskeleton), 18% biotin-tubulin (Cytoskeleton) and 12% rhodamine-tubulin (Cytoskeleton) at a total final tubulin concentration of 20 µM with 1 mM GMPCPP (Jena Biosciences) at 37°C for 30 minutes. MTs were pelleted by centrifugation in an Airfuge for 5 minutes at 119,000 x g and then depolymerized on ice for 20 minutes. This was followed by a second round of polymerization at 37°C with 1 mM GMPCPP. MT seeds were then pelleted as above and diluted 10-fold in MRB80 buffer (80 mM PIPES, pH 6.8, supplemented with 4 mM $MgCl_2$ and 1 mM EGTA) containing 10% glycerol, snap frozen in liquid nitrogen and stored at -80°C.

The *in vitro* reconstitution assays with dynamic MTs were then performed. Briefly, after coverslips were functionalized by sequential incubation with 0.2 mg/ml PLL-PEG-biotin (Susos) and 1 mg/ml neutravidin (Invitrogen) in MRB80 buffer, GMPCPP-stabilized microtubule seeds were attached to the coverslips through biotin-neutravidin interactions. Flow chambers were further blocked with 1 mg/ml κ-casein. The reaction mix with purified proteins in MRB80 buffer supplemented with 20 µM porcine brain tubulin, 0.5 µM X-rhodamine-tubulin, 75 mM KCl, 1 mM GTP, 0.2 mg/ml κ-casein, 0.1% methylcellulose and

oxygen scavenger mix (50 mM glucose, 400 µg/ml glucose oxidase, 200 µg/ml catalase and 4 mM DTT) was added to the flow chamber after centrifugation in an Airfuge for 5 minutes at 119,000 x g. The flow chamber was sealed with vacuum grease, and dynamic MTs were imaged immediately at 30 °C with a TIRF microscope. All tubulin products for TIRF microscopy were from Cytoskeleton.

Protein expression and purification for Cryo-EM. Human CAMSAP1 residues 1474-1613 encompassing the CKK domain (HsCKK) were cloned into pET28a vector and expressed in BL21(DE3) cells (Stratagene). Following purification via immobilized metal-affinity chromatography (IMAC) using Ni-NTA resin (Qiagen), the protein was further purified on an ion exchange column MonoS and gel filtration column Superose 6 (GE Healthcare). Purified protein was concentrated to ~20 mg/ml in BRB20 buffer (20mM PIPES, 2mM $MgCl_2$, 1mM EGTA, 1mM DTT, pH 6.8), snap-frozen and stored at -80 °C.

The DNA encoding for the CKK domain of *N. gruberi* CAMSAP (NgCKK, residues 621-788; Uniprot Gene: NAEGRDRAFT_50049) was cloned into the pET-based bacterial expression vector PSPCm2, which encodes for an N-terminal 6x His-tag and a PreScission cleavage site using a positive selection cloning approach (Olieric et al., 2010). Following protein expression in BL21 (DE3) RIPL cells (Agilent), protein was purified by immobilized metal-affinity chromatography (IMAC) followed by size exclusion chromatography. Purified protein was concentrated to ~24 mg/ml in BRB20 buffer, snap-frozen and stored at -80 °C. Protein quality and identity were analyzed by SDS-PAGE and mass spectrometry, respectively.

tsA201 cell tubulin was purified from tsA201 cell cultures as described previously. Briefly, tubulin was isolated from cell lysates via immobilized TOG1 affinity, then tubulin eluted with 0.5M ammonium sulfate. Tubulin was then buffer exchanged into BRB80 buffer (80mM PIPES, 2mM $MgCl_2$, 1mM EGTA, 1mM DTT, pH 6.8) with 10% glycerol, and 20 µM GTP and flash frozen in liquid nitrogen. The tubulin was further purified by cycling then buffer exchanged into BRB80 with 20µM GTP and flash frozen in liquid nitrogen.

Cryo-EM Sample Preparation. MTs were polymerized at 37°C for 45 minutes from tsA201 cell tubulin at 5mg/ml in BRB80 containing 1 mM GTP. 1mM paclitaxel was then added and MTs incubated at 37°C for another 45 minutes. Stabilised MTs were left at room temperature for at least 24 hours then diluted in BRB80 to 0.5mg/ml before use. 4µl of MTs in BRB20 were pre-incubated on glow-discharged holey C-flat™ carbon EM grids (Protochips, Morrisville, NC) at room temperature for 90 seconds, excess buffer manually blotted away, then 4µl of 1mg/ml HsCKK domain or NgCKK added for 45 seconds. Excess buffer was again manually blotted away, followed by a final 4µl application of either HsCKK or NgCKK at the same concentration. Grids were then placed in a Vitrobot Mark IV (FEI Co., Hillsboro, OR) at room temperature and 80% humidity, incubated for a further 45 seconds, then blotted and vitrified in liquid ethane.

Cryo-EM data collection and processing. Low dose movies were collected manually on a K2 direct electron detector (Gatan) installed on a FEI Tecnai G2 Polara operating at 300kV with a quantum post-column energy-filter (Gatan), operated in zero-loss imaging mode with a 20-eV energy-selecting slit. A defocus range of 0.5-3.5µm and a calibrated final sampling of 1.39Å/pixel was used with the K2 operating in counting mode at 5e-/pixel/second. The total exposure was ~42e-/Å2 over 16 seconds at 4 frames/sec. Movie frames were aligned using Motioncorr2 with a patch size of 5 to generate full dose and dose-weighted sums. Full dose sums were used for CTF determination in gCTF, then dose-weighted sums used in particle picking, processing and generation of the final reconstructions.

Results

Reducing minus end selectivity and pf skew of CAMSAP1 N1492A CKK mutant improved high-resolution NMR studies

Previous study has shown that HsCKK domains introduce protofilament skew of MTs upon binding[2b]. What are the properties of HsCKK that support induction of whole-protofilament skew? To answer this question at atomic resolution we employed solid-state NMR (ssNMR). To collect the highest quality

ssNMR data, a high affinity HsCKK-MT interaction is required. Our previous work identified an HsCKK mutant, N1492A, that increased the binding affinity for MTs compared to wild-type HsCKK while reducing its selectivity for MT minus ends, thereby reducing sample heterogeneity and increasing spectral resolution. We then first prepared the [^{13}C, ^{15}N]-labeled CAMSAP1 CKK N1492A in complex with MTs for ssNMR measurements. Interestingly, the spectra recorded from the mutant showed a much better sensitivity and spectral resolution (Figure 1a, b, blue spectra), compared to the spectra that we recorded previously on the wild type CAMSAP3 CKK in complex with MTs[2b] (Figure 1a, b, red spectra). These findings suggest that the mutant binds MTs with higher affinity, leading to an increase of sample homogeneity and a concomitant reduction in protofilament skew, which is in agreement with previous findings.

Given the improved spectral quality of the CAMSAP1 CKK N1492A data sets, we resorted to the use of fast magic angle spinning (MAS), ^{1}H detected ssNMR experiments to further elucidate the CKK conformations in complex with MTs. As shown in our previous study (Chapter 2) using wild type CKK, conventional, carbon-detected ssNMR data allowed us to compare the chemical shift differences of ^{13}C and ^{15}N to the liquid state NMR data. Including the ^{1}H-detected ssNMR spectra, we could obtain additional structural information by analyzing ssNMR signals along the proton (^{1}H) dimension. As shown in Figure 2, we could directly compare peaks we observed from the carbon-detected and proton-detected spectra. The ^{15}N dimension can be aligned with the 2D NCA (^{13}C-detection) and 2D NH (^{1}H-detection) (Figure 2a, b), while with the help of the 3D CANH spectrum, the ^{13}C dimension can be aligned (Figure 2a, c). This strategy allowed us to analyze and, where appropriate, transfer the solution-state assignments of free CAMSAP1 CKK N1492A to the solid-state spectra recorded on the bound state N1492A mutant. Using this approach, we could transfer 48 backbone assignments of free CKK N1492A to the solid-state spectra (Figure 2d).

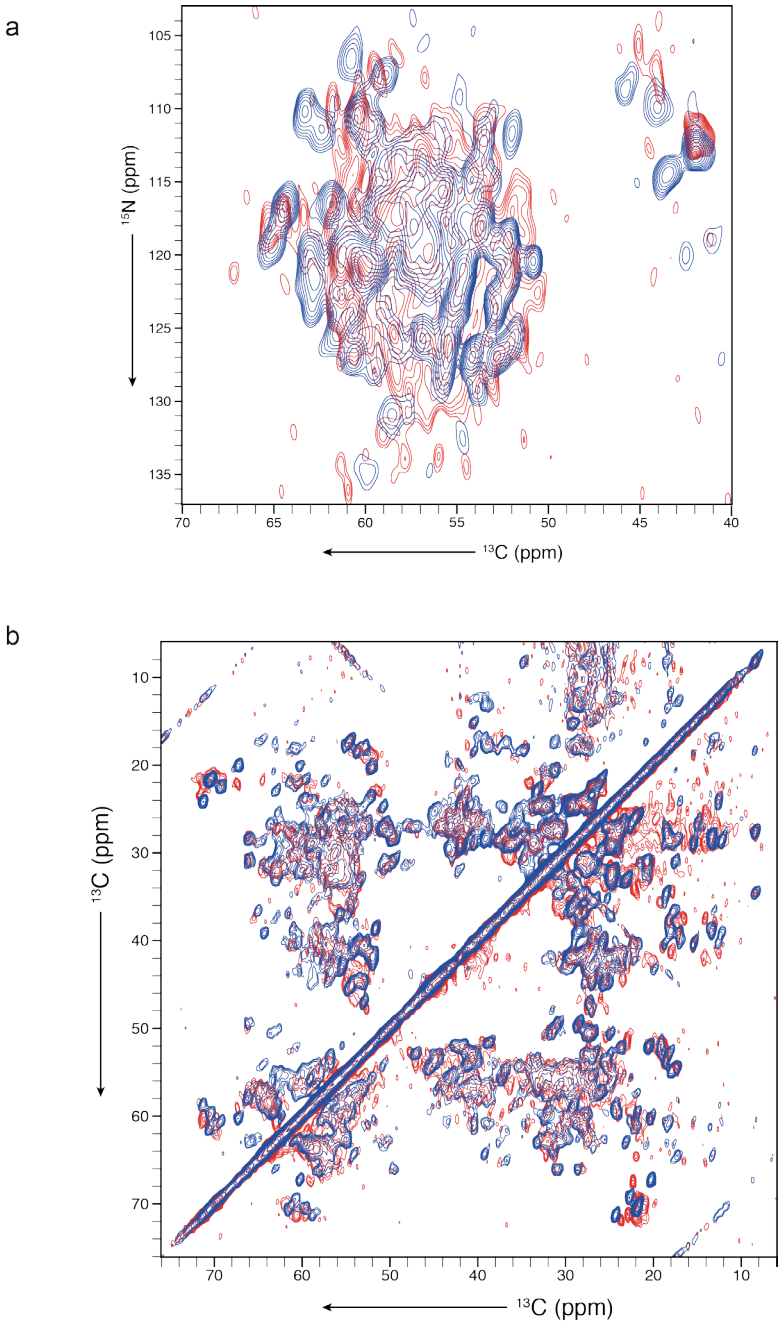

Figure 1. Comparison of solid-state NMR spectra obtained on WT (red, CAMSAP3 CKK) and mutant (blue, CAMSAP1 CKK N1492A) CKK. Data are shown from a) 2D NCA and b) 2D PDSD spectra.

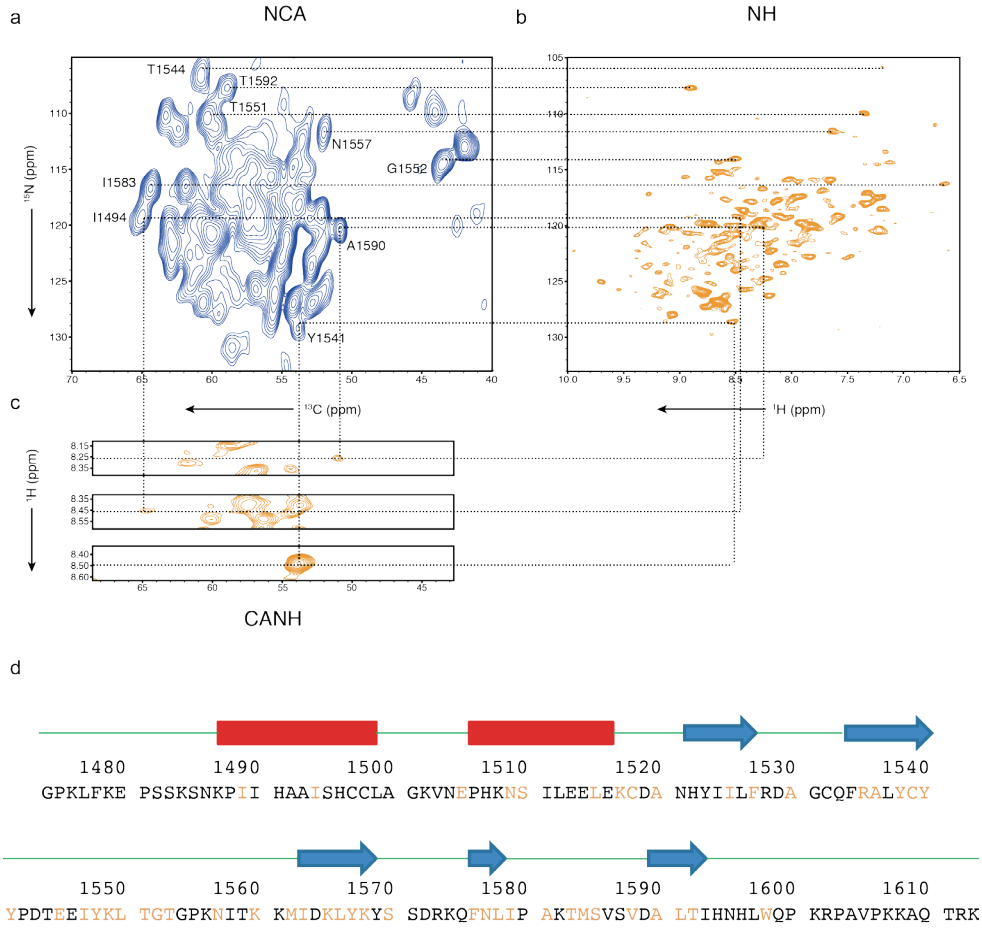

Figure 2. Signal alignments of CAMSAP1 CKK N1492A in complex with MTs. The CAMSAP1 CKK N1492A-MTs complexes were measured at both a) standard MAS as well as b) and c) high MAS for identification of the peaks. a) 9 peaks from the 2D NCA spectrum were shown as examples aligning the ^{15}N dimension of the 2D NH spectrum. b) 3 peaks from the NH spectrum were shown to align the ^{1}H dimension of the 3D CANH. c) These 3 peaks also align the ^{13}C dimension of the NCA spectrum. d) Protein sequence of CAMSAP1 CKK N1492A with representative structural elements (green line: random coil, red box: α helix, blue arrow: β strand). The residues that were transferred and assigned based on the solution-state assignments are labeled in orange.

CKK domains are remarkably rigid both in the free and MT-bound state

We then analyzed the ssNMR and the solution-state NMR results to further examine the binding mode of CAMSAP1 CKK N1492A. An overlay of the solution-state HSQC and the solid-state NH revealed that several peaks appeared at similar chemical-shift values while other peaks underwent chemical-shift perturbations upon binding to MTs (Figure 3a). For example, I1563 and T1551,

which are in loop4 and far from the binding interface with MTs as shown in our previous cryo-EM results, displayed no chemical shift differences between the free- and bound-state (Figure 3b, left and middle panels). However, T1592, which is more close to the binding interface, has almost 0.1 ppm difference on the ^{1}H dimension (Figure 3b, right panel). Interestingly, we did not observe significant chemical-shift changes for the entire set of assigned Cα positions (see examples, Figure 3b, lower panels). This observation suggested that CAMSAP1 CKK N1492A did not undergo significant conformational changes upon MT binding. Instead, the residues showing chemical-shift changes on the NH spectrum were most likely due to changes in the local chemical environment as a result of MT binding, demonstrating that these residues are close to the binding interface. Indeed, the chemical-shift perturbations observed upon MT binding agreed with the previous reported CKK-MT interface while providing a more quantitative and residue-specific description of the behavior of the domain (Figure 4).

To obtain additional insight into the binding mechanism of CKK domains to MTs, we probed residue-specific dynamics of the free CKK domains using solution-state NMR. Specifically, we conducted Carr-Purcell-Meiboom-Gill (CPMG) relaxation dispersion[11] and Chemical Exchange Saturation Transfer (CEST) experiments[12] to reveal possible millisecond time-scale conformational exchange processes of mammalian CKK domains. The CPMG profiles of HsCKK_N1492A, HsCKK and the CKK domain from mouse CAMSAP3 all showed no exchange in these CPMG time ranges (50 Hz~1.5 kHz) (Figure 5). Similarly, the results of additional CEST experiments using HsCKK_N1492A speak against slow milli-second time-scale motion in free CKK domains, for example, in residues T1553 and S1585, which exhibited significant chemical-shift changes upon complex formation (Figure 6a). Similar results were obtained for CAMSAP3 CKK (Figure 6b). Taken together, our NMR experiments suggest that the 3D structures of human CKK domains are remarkably rigid and, in contrast to many other MAPs, do not undergo structural changes upon MT binding. These CKK properties are likely to be integral to the mechanism of CAMSAP CKK recognition of MT minus ends.

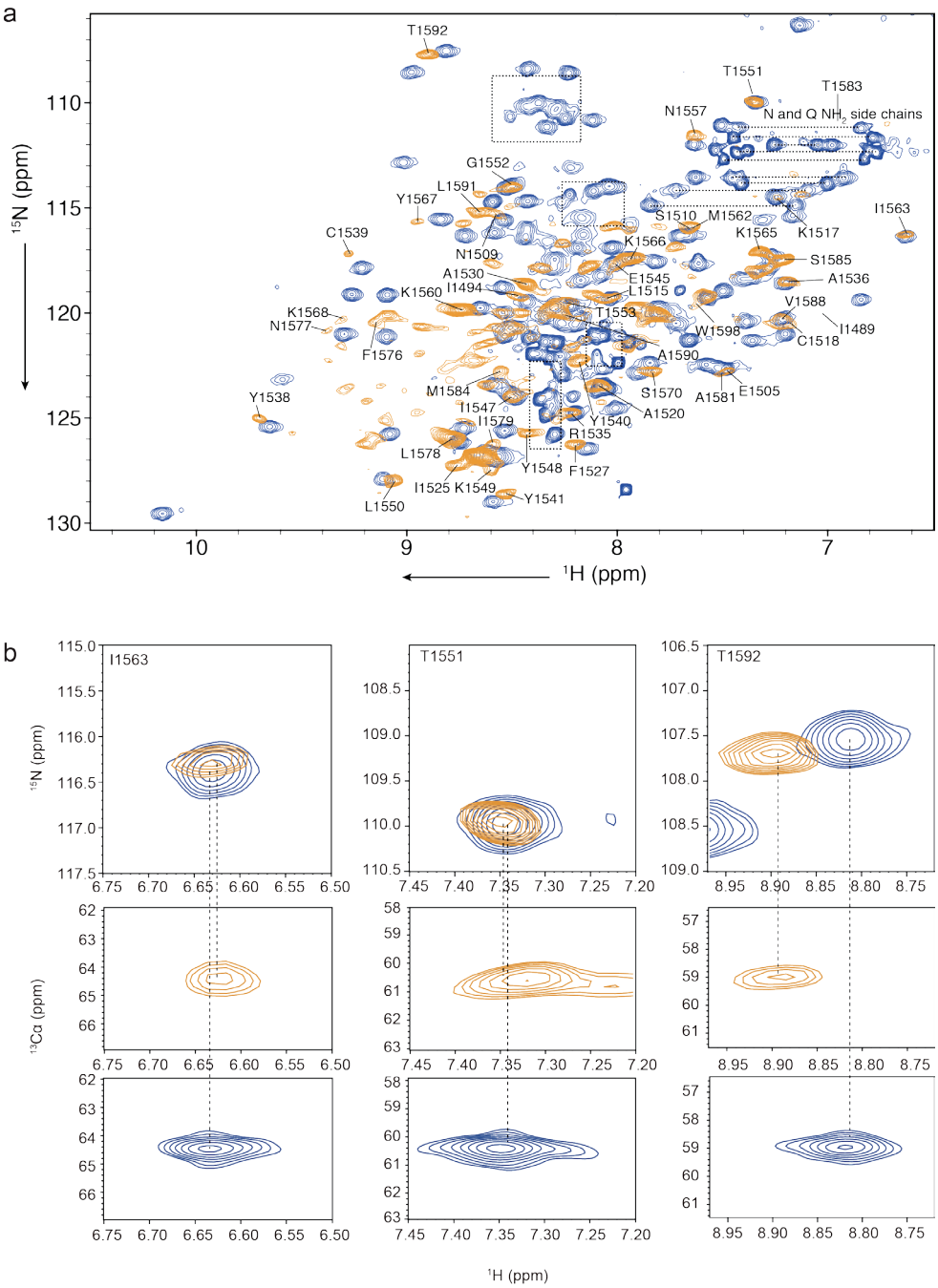

Figure 3. a) NMR Chemical-shift perturbations of CAMSAP1 CKK N1492A upon binding to MTs. 2D NH correlations are shown for free CAMSAP1 CKK N1492A in solution (blue) and MT bound CKK (orange). For clarification, NH_2 correlations from the side chains of N and Q residues are indicated by dashed lines. Furthermore, signals from purification tags are highlighted (boxes) that do not appear in the ssNMR NH

correlation spectrum (orange) of the MT-bound CKK. The 48 transferred assignments based on solution-state NMR data were shown on the spectrum, note that the signals for I1489 and T1583 were weak in the NH spectrum and invisible at the presented contour level; b) Spectral cutouts comparing solid-state NMR signal sets of free (blue) and MT bound (orange) HsCKK_N1492A for three selected residues. Top panels show the zoom-in regions from the 2D ^{15}N-^{1}H correlated spectra, while the middle and bottom panels reflect regions from 3D CANH (solid state) and HNCA (liquid state) spectra at corresponding ^{15}N chemical shifts, respectively. See panel b for full spectra.

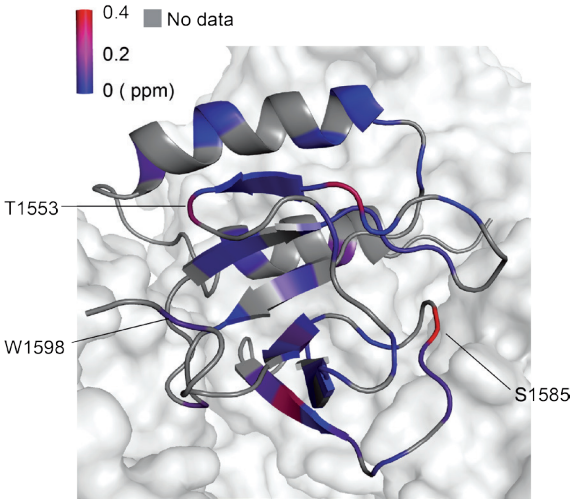

Figure 4. Chemical-shift perturbations, colored by differences in ppm, arising from HsCKK_N1492A binding to MTs mapped on the structure of CKK-MT complex (PDB: 5M5C); the CKK domain is depicted in a ribbon representation while the MT surface is shown as a space-filling model.

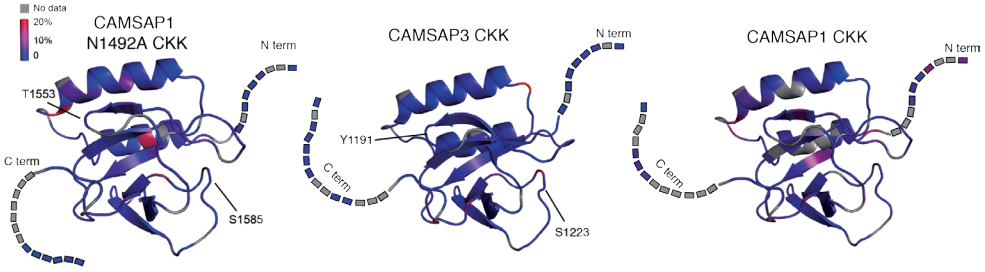

Figure 5. Changes of transverse relaxation rates obtained from solution-state NMR CPMG experiments plotted on the 3D structure of the free CKK domains. Comparison of CAMSAP1 N1492A CKK (left panel), wild type CAMSAP3 CKK (middle panel) and CAMSAP1 CKK (right panel) transverse relaxation rates with same CPMG setting.

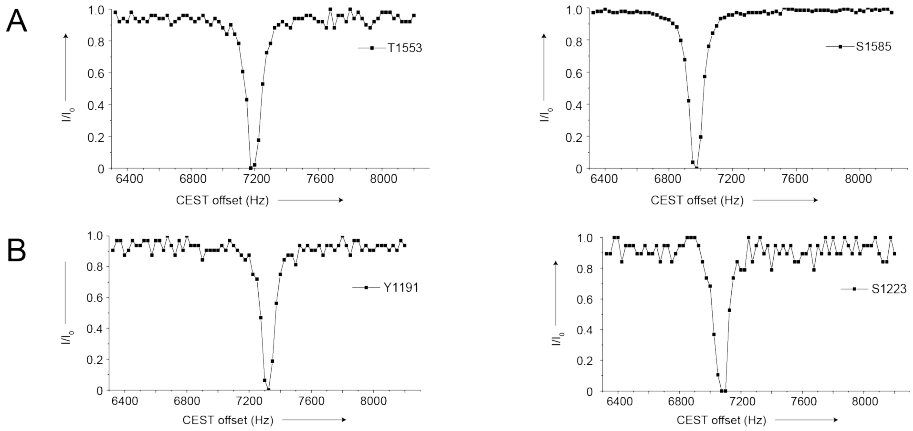

Figure 6. a) Solution CEST profiles of free CAMSAP1 N1492A CKK shown for residues T1553 and S1585, which showed significant chemical shift perturbation upon binding to MTs (see Fig. 4). b) CEST profiles of Y1191 and S1223 from CAMSAP3 CKK exhibiting similar dynamics profiles as shown for T1553 and S1585 from CAMSAP1 CKK N1492A panel a.

HsCKK remodels its binding site causing protofilament tilting and MT diameter shrinkage

The presence of CKK domains in diverse organisms presents a unique resource that can shed light on the conserved or divergent properties of these domains. Our previous analysis suggested that a CKK domain from *N. gruberi* did not exhibit MT minus-end binding preference. We confirmed this using TIRF experiments, showing that, in comparison to the well-characterised MT minus-end preference of HsCKK (Figure 7a, left panel), NgCKK strongly bound along the entire MT lattice and showed no MT minus-end preference on dynamic MTs at a range of concentrations (Figure 7a, right panels).

To investigate this distinctive behaviour further, complexes formed by either NgCKK or HsCKK and taxol-stabilized MTs were imaged using cryo-EM for structure determination. The resulting unsymmetrized (C1) reconstructions for both NgCKK and HsCKK showed distinct CKK intra-dimer, inter-protofilament densities every 8 nm along the MT axis and an absence of CKK density at the seam (Figure 7b, c), which is consistent with our previous work.

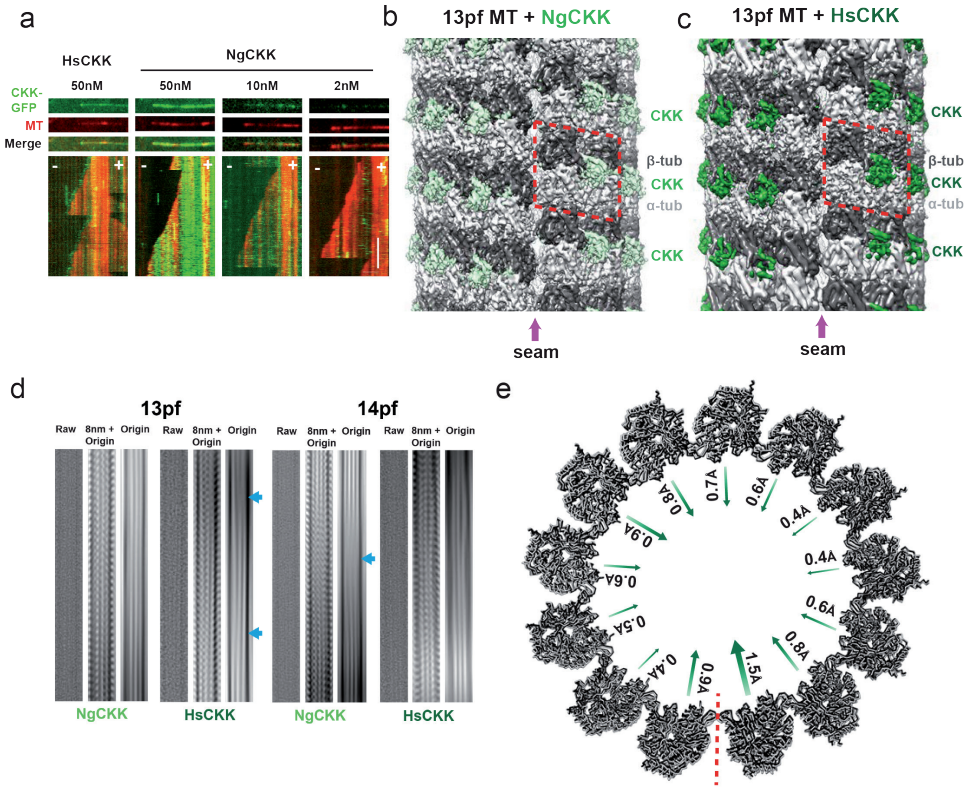

Figure 7. a) TIRF assays with dynamic MTs demonstrate that unlike HsCKK, the NgCKK domain does not have a preference for MT minus ends but binds along the whole MT lattice at a range of concentrations. Scale bars: horizontal, 2 µm; vertical, 2 min. b) C1 reconstruction of the NgCKK-bound tsA201-tubulin 13-protofilament MT at 4.3Å resolution, showing CKK density (in light green) bound every 8nm between protofilaments at the intradimer tubulin interface, except at the MT seam; the reconstruction procedure produces a resolution gradient in the density which highest in the middle and lowest at the top and bottom; c) C1 reconstruction of the HsCKK-bound tsA201-tubulin 13-protofilament MT at 4.5Å resolution, showing CKK density (in green) bound every 8nm between protofilaments at the intra-dimer tubulin interface, except at the MT seam; as above, the reconstruction procedure produces a resolution gradient in the density which highest in the middle and lowest at the top and bottom. d) Raw and Fourier filtered images of 13- (left) and 14- protofilament (right) MTs decorated by NgCKK and HsCKK. In each set of 3 panels: left, raw image; centre, filtered image to include data at, and adjacent to, the origin and the 1/8nm layer line shows density corresponding to the CKK domain every tubulin dimer; right, filtered image to include data at, and adjacent to, the origin highlights the MT moiré pattern and the effect of CKK binding on protofilament skew; blue arrows indicate variations in the moiré pattern that arise from protofilament skew. e) HsCKK MT binding is accompanied by contraction of the MT diameter; a single turn of models docked within the aligned HsCKK and NgCKK C1 reconstructions are shown viewed from the minus end; arrows indicate the irregular shift of individual protofilaments.

In addition to comparison of the NgCKK and HsCKK binding sites, the overall architecture of the decorated MTs can be compared to shed further light

on HsCKK minus-end preference. We previously described the ability of HsCKK to induce positive (right-handed) protofilament skew in MTs polymerized from mammalian brain tubulin. Raw images (Figure 7d) from our new HsCKK-MT data set support this observation on tsA201 cell tubulin MTs. 13-protofilament MTs usually have unskewed protofilaments, running straight along the MT wall, whereas HsCKK binding causes right-handed protofilament skew (Figure 7a, left panel, highlighted with blue arrows). Furthermore, 14-protofilament MTs usually have negatively skewed protofilaments but HsCKK binding caused these protofilaments to lie parallel to the MT wall with no skew (Figure 7a, right panel). In other words, we observed induction of right-handed protofilament skew in both types of MT architectures. Intriguingly - and in contrast to the HsCKK - the intrinsic protofilament skew in both 13- and 14-protofilament MTs was unperturbed by NgCKK binding (Figure 7a). This is consistent with the idea that protofilament skew induction by HsCKK correlates with MT minus-end specificity. Given the unusual rigidity of HsCKK, we wanted to know how protofilament skew was brought about by HsCKK binding and accommodated by the MT lattice. We compared the protofilaments in HsCKK-MTs and in NgCKK-MTs. The protofilaments in HsCKK-MTs are closer together (Figure 7e), giving these MTs a ~4 Å smaller diameter than NgCKK-MTs with the same protofilament number. This inward protofilament positioning is not symmetrical around the MT, with a range of 0.4-1.5Å relative shifts observed in 13-protofilament architecture, and with the biggest deviations seen at and opposite of the seam. In summary, relative to NgCKK, the rigidity of HsCKK enables it to induce protofilament tilt, shear, lateral compression and a reduction in MT diameter.

Discussion

To shed light on the MT minus-end binding preference of CAMSAPs, we have employed ssNMR for ^{1}H-detection on CAMSAP1 CKK N1492A in complex with MTs, showing that CKK N1492A is rigid and does not undergo conformational changes upon binding to MTs, which is in agreement with our previous findings. By using solution-state NMR we observed no millisecond time-scale conformational exchange of CKK, indicating that CKK itself is a remarkably rigid protein. We then structurally compared a CKK domain that does not bind

MT minus ends, NgCKK, with the CKK domain from human CAMSAP1 (HsCKK), which mediates CAMSAP1's MT minus-end binding preference. We found that HsCKK binding induces positive protofilament skew in both 13- and 14-protofilament MTs while NgCKK does not. Our reconstructions show that HsCKK brings the tubulin dimers to which it binds closer together, and the rigidity of HsCKK supports its ability to remodel its binding site.

The first new and important aspect of the MT minus-end recognition mechanism by HsCKK revealed by our current data is that the CKK domain itself does not flexibly respond to different tubulin conformations. Rather, its rigidity is consistent with its sensitivity to, and affinity for, the conformation(s) of polymerised tubulin it encounters. Second, we confirmed that the ability to induce significant protofilament skew in fully decorated MTs correlates with MT minus-end recognition activity. This was previously observed in the HsCKK-N1492A mutant but is now confirmed in the comparison of HsCKK with NgCKK. Third, we previously speculated that skew induction reflects the non-optimal geometry for HsCKK binding of tubulin dimers within the MT lattice compared to minus ends. Our new reconstructions show that this is indeed the case, and that skew arises in response to HsCKK forcing the two tubulin dimers it contacts closer together. Consistent with this idea, the CKK binding site on neighbouring tubulin dimers are predicted to be laterally closer in the transition zone to gently curved tubulin sheets near MT minus ends which HsCKK prefers. Fourth, a key prediction of our model is that end specificity by HsCKK is mediated by the asymmetric curvature of tubulin at the minus end, with the α-tubulins less laterally curved relative to the β-tubulins. Conversely, at plus ends - with the β-tubulins less laterally curved - HsCKK binding is inhibited. Altogether, this model describes how HsCKK has highest affinity for MT minus ends, some capacity to interact with the MT lattice but lowest affinity for plus ends. It is clear that small differences between HsCKK and NgCKK, and between the effects they induce on MT binding, combine to produce large effects in terms of MT end recognition properties (Figure 8).

Structural studies of MT-bound MAPs typically reveal conformational changes in the MAP on interaction with the MT lattice. In the most extreme cases, unstructured proteins such as members of the tau/MAP2 family and the mitotic regulatory protein TPX2, become at least partially ordered when in contact with

MTs[14]. A recent study on a companion of cellulose synthase 1 also showed similar interactions between its disordered N-terminus and the MTs in plants[15]. Folded MT binding domains in a number of MAPs - for example, kinesin motor domains[16], CH domains in EB proteins[17], the p150glued CAP-Gly domain[18] - often undergo some rearrangements and/or ordering of otherwise disordered loop regions on formation of the MT-bound complex. In contrast, we show that the HsCKK is sufficiently rigid that it does not undergo conformational changes on MT interaction, but rather the MT lattice is remodelled in response to HsCKK binding. In the case of HsCKK, this is because the main MT lattice is not the preferred binding substrate for CKK. However, this behaviour - in which a structurally invariant MAP is exquisitely sensitive to the precise conformation of the underlying tubulin - is likely to be shared by other proteins.

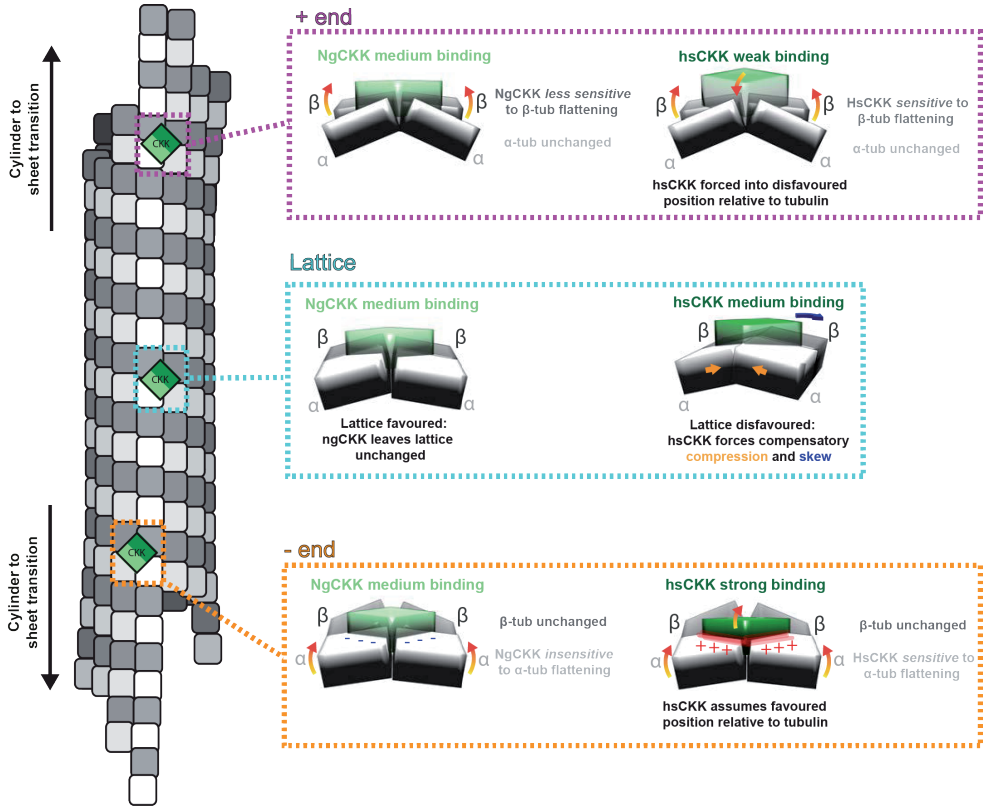

Figure 8. Comparison of MT binding properties of NgCKK and HsCKK substantiates and expands the model of CAMSAP MT minus end recognition.

Taken together, our data support the idea that MTs can act as allosteric signalling platforms, in which the precise configuration of polymerized tubulins are influenced by their dynamic state and binding partners[19]. In the case of CAMSAPs/Patronins, sensitivity to structural variations in tubulin is essential for MT minus end recognition. These insights will inform future mechanistic investigations of conformational signalling arising from the MT cytoskeleton.

References:

[1] A. Akhmanova, M. O. Steinmetz, *Nature Reviews Molecular Cell Biology* **2015**, *16*, 711.

[2] a) E. M. Mandelkow, E. Mandelkow, R. A. Milligan, *The Journal of Cell Biology* **1991**, *114*, 977; b) J. Atherton, K. Jiang, M. M. Stangier, Y. Luo, S. Hua, K. Houben, J. J. E. van Hooff, A.-P. Joseph, G. Scarabelli, B. J. Grant, A. J. Roberts, M. Topf, M. O. Steinmetz, M. Baldus, C. A. Moores, A. Akhmanova, *Nature Structural &Amp; Molecular Biology* **2017**, *24*, 931; c) J. Atherton, M. Stouffer, F. Francis, C. A. Moores, *Acta Crystallographica Section D* **2018**, *74*, 572-584; d) J. R. McIntosh, E. O'Toole, G. Morgan, J. Austin, E. Ulyanov, F. Ataullakhanov, N. Gudimchuk, *The Journal of Cell Biology* **2018**, *217*, 2691.

[3] a) A. Akhmanova, Casper C. Hoogenraad, *Current Biology* **2015**, *25*, R162-R171; b) M. Martin, A. Akhmanova, *Trends in Cell Biology* **2018**, *28*, 574-588.

[4] a) M. Chuang, A. Goncharov, S. Wang, K. Oegema, Y. Jin, Andrew D. Chisholm, *Cell Reports* **2014**, *9*, 874-883; b) Kah W. Yau, Sam F. B. van Beuningen, I. Cunha-Ferreira, Bas M. C. Cloin, Eljo Y. van Battum, L. Will, P. Schätzle, Roderick P. Tas, J. van Krugten, Eugene A. Katrukha, K. Jiang, Phebe S. Wulf, M. Mikhaylova, M. Harterink, R. J. Pasterkamp, A. Akhmanova, Lukas C. Kapitein, Casper C. Hoogenraad, *Neuron* **2014**, *82*, 1058-1073; c) M. Toya, S. Kobayashi, M. Kawasaki, G. Shioi, M. Kaneko, T. Ishiuchi, K. Misaki, W. Meng, M. Takeichi, *Proceedings of the National Academy of Sciences* **2016**, *113*, 332; d) V. Pongrakhananon, H. Saito, S. Hiver, T. Abe, G. Shioi, W. Meng, M. Takeichi, *Proceedings of the National Academy of Sciences* **2018**, *115*, 9750.

[5] K. Jiang, S. Hua, R. Mohan, I. Grigoriev, Kah W. Yau, Q. Liu, Eugene A. Katrukha, A. F. M. Altelaar, Albert J. R. Heck, Casper C. Hoogenraad, A. Akhmanova, *Developmental Cell* **2014**, *28*, 295-309.

[6] A. J. Baines, P. A. Bignone, M. D. A. King, A. M. Maggs, P. M. Bennett, J. C. Pinder, G. W. Phillips, *Molecular Biology and Evolution* **2009**, *26*, 2005-2014.

[7] a) N. Bloembergen, *Physica* **1949**, *15*, 386-426; b) N. M. Szeverenyi, M. J. Sullivan, G. E. Maciel, *Journal of Magnetic Resonance (1969)* **1982**, *47*, 462-475.

[8] M. Baldus, *Progress in Nuclear Magnetic Resonance Spectroscopy* **2002**, *41*, 1-47.

[9] M. Baldus, A. T. Petkova, J. Herzfeld, R. G. Griffin, *Molecular Physics* **1998**, *95*, 1197-1207.

[10] D. H. Zhou, A. J. Nieuwkoop, D. A. Berthold, G. Comellas, L. J. Sperling, M. Tang, G. J. Shah, E. J. Brea, L. R. Lemkau, C. M. Rienstra, *Journal of Biomolecular NMR* **2012**, *54*, 291-305.

[11] D. M. Korzhnev, L. E. Kay, *Accounts of Chemical Research* **2008**, *41*, 442-451.

[12] P. Vallurupalli, G. Bouvignies, L. E. Kay, *Journal of the American Chemical Society* **2012**, *134*, 8148-8161.

[13] M. P. Williamson, *Progress in Nuclear Magnetic Resonance Spectroscopy* **2013**, *73*, 1-16.

[14] a) R. Zhang, J. Roostalu, T. Surrey, E. Nogales, *eLife* **2017**, *6*, e30959; b) E. H. Kellogg, N. M. A. Hejab, S. Poepsel, K. H. Downing, F. DiMaio, E. Nogales, *Science* **2018**, *360*, 1242.

[15] C. Kesten, A. Wallmann, R. Schneider, H. E. McFarlane, A. Diehl, G. A. Khan, B.-J. van Rossum, E. R. Lampugnani, W. G. Szymanski, N. Cremer, P. Schmieder, K. L. Ford, F. Seiter, J. L. Heazlewood, C. Sanchez-Rodriguez, H. Oschkinat, S. Persson, *Nature Communications* **2019**, *10*, 857.

[16] J. Atherton, I. Farabella, I. M. Yu, S. S. Rosenfeld, A. Houdusse, M. Topf, C. A. Moores, *eLife* **2014**, *3*, e03680.

[17] Sebastian P. Maurer, Franck J. Fourniol, G. Bohner, Carolyn A. Moores, T. Surrey, *Cell* **2012**, *149*, 371-382.

[18] S. Yan, C. Guo, G. Hou, H. Zhang, X. Lu, J. C. Williams, T. Polenova, *Proceedings of the National Academy of Sciences* **2015**, *112*, 14611.

[19] a) G. J. Brouhard, L. M. Rice, *Nature Reviews Molecular Cell Biology* **2018**, *19*, 451-463; b) R. A. Cross, *Current Opinion in Cell Biology* **2019**, *56*, 88-93.

CHAPTER 4

Structural investigation of ensconsin (MAP7) and its interaction with microtubules

Abstract

The MAP7 protein family includes ensconsin (MAP7), MAP7 domain-containing protein 1, 2 and 3 (MAP7D1, MAP7D2 and MAP7D3 respectively). MAP7 can bind to the microtubule lattice via the N-terminal microtubule-binding domain and recruit kinesin-1 motor protein to microtubules through the kinesin-binding C-terminal domain. Here, we use NMR-based approaches to investigate the structure of the MAP7 microtubule-binding domain and its interaction with microtubules. Chemical-shift assignments of the free- and microtubule-bound-state MAP7 microtubule-binding domain (MTBD) indicate that this protein fragment is highly α-helical. Chemical-shift perturbations and differences in ssNMR signal intensity upon binding to microtubules revealed that a short hinge between two α-helices of MAP7-MTBD undergoes conformational changes upon binding to microtubules. Based on our data we proposed a model that electrostatic interaction is important for MAP7-MTBD binding to microtubules and this might lead to the competition microtubule binding with microtubule-binding protein Tau.

Introduction

MAP7 (also known as ensconsin or E-MAP-115) was first found in HeLa cells and shown to interact with microtubules (MTs)[1]. MAP7 is predominantly expressed in epithelial cells, such as HeLa cells, and known to stabilize MTs[1b]. In mammals, MAP7 protein family members include MAP7, MAP7D1, MAP7D2 and MAP7D3. All consist of a C-terminal kinesin-1-binding domain and a N-terminal microtubule-binding domain (MTBD) that binds MTs. Both domains are predicted to adopt coiled-coil structure (Figure 1a)[2]. In addition, the intrinsically disordered region in between the two domains in MAP7, which is also named P domain due to many potential phosphorylation sites in this region, has recently also been found to interact with MTs[3]. As for MAP7D3, the C-terminal tail is also identified as region with MT affinity[4]. A recent study has shown that MAP7 family protein members bind to MTs and acts as positive regulators of kinesin-1, which is an important motor protein that moves cargo such as an organelle towards the MT plus ends, by promoting kinesin-1 processivity[5]. Interestingly, another recent study showed that protein Tau competes for binding with MAP7

on the microtubule lattice[6]. This competition indicates that Tau could act as a negative regulator of kinesin-1 binding to MTs. Therefore, the competition of MAP7 and Tau binding to MTs is essential in regulating kinesin-1 recruitment in cells, and disruption of this transport process has been implicated in disease[7].

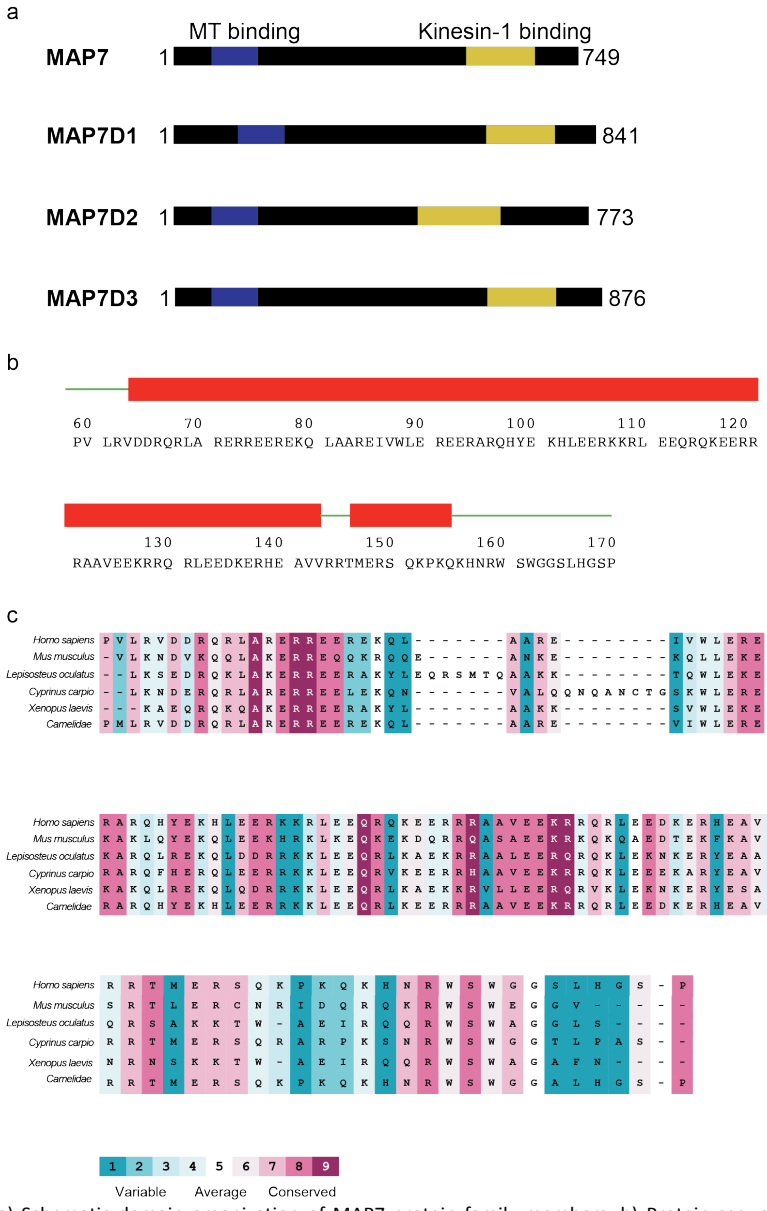

Figure 1. a) Schematic domain organization of MAP7 protein family members. b) Protein sequence of MAP7 MTBD and the secondary structural prediction performed with JPred4[8]. The secondary structural elements are

represented by red boxes (α-helix) and green lines (random coil). c) Multiple sequence alignment performed using ConSurf[9] of MAP7-MTBD. Note that 150 protein sequences were used in the alignment and 5 of them were shown as examples. The sequences were colored by the extent of amino acid conservation.

Given the importance of MAP7 in MT and kinesin-1 binding as well as the remarkable interplay with Tau binding, structural insight into the interaction of MAP7 with MTs is highly desirable. To this end, our aim has been to understand how the N-terminal MTBD of MAP7 interacts with MTs on the lattice. Previous chapters have shown the power of solid- and solution-state NMR to study the structures of proteins that bind MTs and identify the binding interface with MTs. Since the actual structure of MTBD of MAP7 is not known yet, we employed both liquid-state and solid-state NMR to characterize the structures of the MTBD in free- and MT-bound-state, respectively.

Materials and methods

Secondary structure prediction and multiple sequence alignment of MAP7-MTBD. The sequence of human MAP7-MTBD (residue 59-170) was analyzed using the JPred4 server[8] to predict the secondary structure. Multiple sequence alignment was performed by employing the ConSurf server[9].

Gene cloning. The cDNA of human MAP7-MTBD (residues 59-170) was cloned into the pLICHIS vectors with the genes encoding a N-terminal His tag-thrombin cleavage site and a N-terminal His tag-Maltose-binding protein (MBP)-thrombin cleavage site respectively by using Ligation Independent Cloning (LIC)[10].

Protein expression and purification. For the His tagged MAP7-MTBD without MBP fusion, *E. coli* Rosetta 2 cells were transformed with the plasmid. The cells were grown in 1 L M9 minimum medium supplemented with 2 g ^{13}C-glucose, 0.5 g $^{15}NH_4Cl$, 100 mg ampicillin and 35 mg chloramphenicol. Cells were induced when the OD_{600} reached 0.6 with 0.3 mM IPTG at 37 °C for 3.5 hrs. For the MBP-fused MAP7-MTBD, transformation was done with *E. coli* Rosetta 2 cells and

grown in 1 L [^{13}C, ^{15}N]-labeled (for ssNMR sample preparation and measurements) or unlabeled (for microtubule pelleting assay) M9 medium as described above. Induction of the protein was done when OD_{600} reached 0.6 with 0.3 mM IPTG at 20 °C for 16 hrs. The cultures were then centrifuged with 4,000 × g at 4°C for 20 min to harvest cells. Cell pellets were washed with 50 mM sodium phosphate buffer, pH 8, 500 mM NaCl, 1 mM β-mercaptoethanol and 20 mM imidazole and store at -80 °C.

To purify the His tagged-MAP7-MTBD, the cell pellet was washed first washed with 50 mM sodium phosphate buffer, pH 8, 500 mM NaCl, 1 mM β-mercaptoethanol and 20 mM imidazole supplemented with protease inhibitors. Cell lysis was done by sonication on ice and the cell lysate was collected by centrifugation of 40,000 × g at 4°C for 30 min. Subsequently, the proteins were purified by a ÄKTA pure system with a POROS™ MC column that was saturated with Ni^{2+}. The column was first equilibrated with the same buffer as above mentioned. The cell lysate was then loaded onto the column and the column was washed with 20 column volumes with the same buffer. Proteins were eluted with 50 mM sodium phosphate buffer, pH 8, 150 mM NaCl, 1 mM β-mercaptoethanol and 400 mM imidazole supplemented with protease inhibitors. The sample was concentrated with an Amicon® ultra-15 centrifugal filter unit (3 kDa cutoff) and exchanged in 40 mM sodium phosphate buffer, pH 6.5, 150 mM NaCl, 1 mM 1,4-dithiothreitol (DTT) supplemented with protease inhibitors.

To purify the His tagged-MBP-MAP7-MTBD, his-tag purification was performed as described above. After eluting the protein with 50 mM sodium phosphate buffer, pH 8, 150 mM NaCl, 1 mM β-mercaptoethanol and 400 mM imidazole supplemented with protease inhibitors, the sample was concentrated and then diluted with 40 mM sodium phosphate buffer, pH 6.5 to reach a final concentration of imidazole of 20-30 mM. Subsequently, a cation exchange purification was performed with the Hitrap HP SP chromatography column (GE Healthcare Life Sciences). The column was first equilibrated with buffer A (40 mM sodium phosphate buffer, pH 6.5). The sample was then loaded onto the column and washed 5 column volumes with buffer A. A gradient elution was used by combining buffer A and buffer B (40 mM sodium phosphate buffer, 1 M NaCl, pH 6.5) to elute the protein. The protein was then concentrated and stored at 4 °C.

Microtubule pelleting assay. The purified his tagged-MBP-MAP7-MTBD was incubated with 5 U thrombin at 4 °C for 16 hrs to cleave the fused MBP protein and then supplemented with protease inhibitors. 10 mg/ml porcine brain tubulin was diluted in BRB80 buffer (80mM K-PIPES, pH 6.8, 1 mM EGTA, 1 mM $MgCl_2$) to 2 mg/ml. After the addition of 1 mM GTP, the sample was incubated on ice for 5 min. MT polymerization was performed at 30 °C for 20 min. Subsequently, 20 µM taxol was added and incubated for 15 min at 30 °C. Microtubule pelleting assays in the presence of MAP7-MTBD were performed by mixing with different molar ratios of MAP7-MTBD:MTs. As control treatments, taxol-stabilized MTs or MAP7-MTBD was applied alone. All the samples were then centrifuged at 180,000 × g for 30 min at 30 °C, an aliquot was taken from the supernatant. After removal of the supernatant, the pellet was resuspended in SDS sample buffer. Samples of supernatant and pellet fractions were loaded and analyzed on Coomassie-stained 12.5% SDS gels.

Sample preparations for NMR. For solution-state NMR, [^{13}C, ^{15}N]-labeled His tagged MAP7-MTBD was purified as above described. The sample was then supplemented with 5% D_2O for solution-state NMR measurements.

Before sample preparation for ssNMR, the purified [^{13}C, ^{15}N]-labeled His tagged-MBP-MAP7-MTBD was first incubated with 5 U thrombin at 4 °C for 16 hrs to cleave the fused MBP protein. Protease inhibitors were then added to the proteins. To prepare MAP7-MTBD-MT complexes, 20 mg of lyophilized porcine tubulin was dissolved in BRB80 buffer to a final concentration of 2 mg/ml. Microtubule polymerization was done with 1 mM GTP and addition of 20 µM paclitaxel (Sigma) for 30 min at 30 °C. Paclitaxel-stabilized MTs were pelleted down at 180,000 × g (Beckman TLA-55 rotor) at 30 °C for 30 min and resuspended in warm BRB80 buffer with 20 µM paclitaxel. [^{13}C, ^{15}N]-labeled MAP7-MTBD was then added to molar ratio of 2:1 for MAP7-MTBD/MT and incubated at 30 °C for 30 min. The pellet was centrifuged down at 180,000 × g (Beckman TLA-55 rotor) at 30 °C for 30 min and washed with 40 mM phosphate buffer, pH 6.5 supplemented with protease inhibitors, without disturbing the pellet. The pellet was then transferred and packed into a 3.2 mm rotor.

NMR experiments and data analysis. Resonance assignments of MAP7-MTBD were obtained by analysis of standard solution-state NMR experiments (2D HSQCs, 3D HNCA, HNCACB, CBCA(CO)NH) on free [^{13}C, ^{15}N]-labeled MAP7-MTBD recorded on a 600 MHz spectroscopy (Bruker Biospin). ssNMR experiments were performed on a 700 MHz standard-bore spectrometer (Bruker Biospin) equipped with a 3.2 mm triple-channel MAS HCN probe. The experiments include 2D ^{13}C-^{13}C with phase-alternated recoupling irradiation scheme (PARIS)[11] recorded under short (30 ms) and long (120 ms) ^{13}C-^{13}C mixing times (set temperature 265 K, MAS rate 13 kHz).

To analyze the secondary structural elements of both the free and MT-bound MAP7-MTBD, chemical shift predictions for all amino acids in different structural elements (random coil, α helix and β strand) were generated using the FANDAS 2.0[12] web server. To translate the chemical-shift values of the assigned residues into secondary structural, a chemical shift index protocol was employed[13].

Generation of model of MAP7-MTBD. The proposed model of MT-bound MAP7-MTBD was generated from Swiss-PdbViewer[14].

Results

MAP7-MTBD is helical structured domain in solution

A previous study has found that the MTBD of MAP7 (residues 59-170) is the main region that is associated in MT binding by using both biochemical and cell biological methods[5]. We first investigated whether this segment represents a folded protein fragment. The sequence of MAP7-MTBD was first analyzed by JPred4[8] in order to obtain a prediction for secondary structure (Figure 1b). The result suggested that MAP7-MTBD domain is a highly α-helical protein fragment with unstructured termini. The first α-helix starts from D65 until V143 and is followed by a short loop from R144 to T146. The second α-helix starts from M147 to Q155 and is followed by the C-terminal tail. We then analyzed the conservation of the protein sequence by doing multiple sequence alignment with

ConSurf[9] (Figure 1c). Interestingly, we found that MAP7-MTBD is mostly conserved with glutamate, lysine, arginine residues, which might be an indication that the charged residues are important for the MTBD functioning. While the C-terminal tail showed a less conservation of amino acids, except for the fragment N158 to G164, including a WSW motif, that exhibited a relatively conserved amino acid sequence. To confirm the protein folding of MAP7 MTBD, we then produced and purified [^{13}C, ^{15}N]-labeled MAP7-MTBD in the free state. The protein was essentially pure after purification (Figure 2) and therefore we measured the sample by using solution-state NMR. An ^{15}N-HSQC experiment was first performed with the [^{13}C, ^{15}N]-labeled MAP7-MTBD (Figure 3a). The signal dispersion of the spectrum is rather limited, indicating the protein is either intrinsically disordered or α-helical, as the extent of signal dispersion in the proton dimension for these structures is much smaller than the ones for β-stranded proteins. To further characterize the secondary structures of this protein, a ^{13}C-HSQC experiment was then performed and overlaid with the chemical-shift predictions of different amino acids in different secondary structures (Figure 3b). By detailed analysis of the Cα-Hα cross peak region, we could confirm that signals from the β-strands, which usually exhibit Hα chemical shifts of more than 4.7 ppm, were absent, indicating that β-strand is indeed not present in MAP7-MTBD (Figure 3b, blue crosses). On the other hand, signals observed in the ^{13}C-HSQC are more representative for α-helical and random coil structures, which is consistent with the prediction for the secondary structure that the MTBD is partially folded and α-helical (Figure 1b).

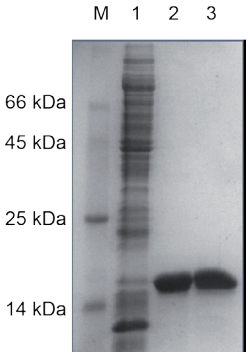

Figure 2. SDS-PAGE demonstrating the purification of His tagged MAP7-MTBD. M: protein marker; 1: unbound fraction in His-tag purification; 2: eluted protein (MAP7-MTBD); 3: MAP7-MTBD after buffer exchange.

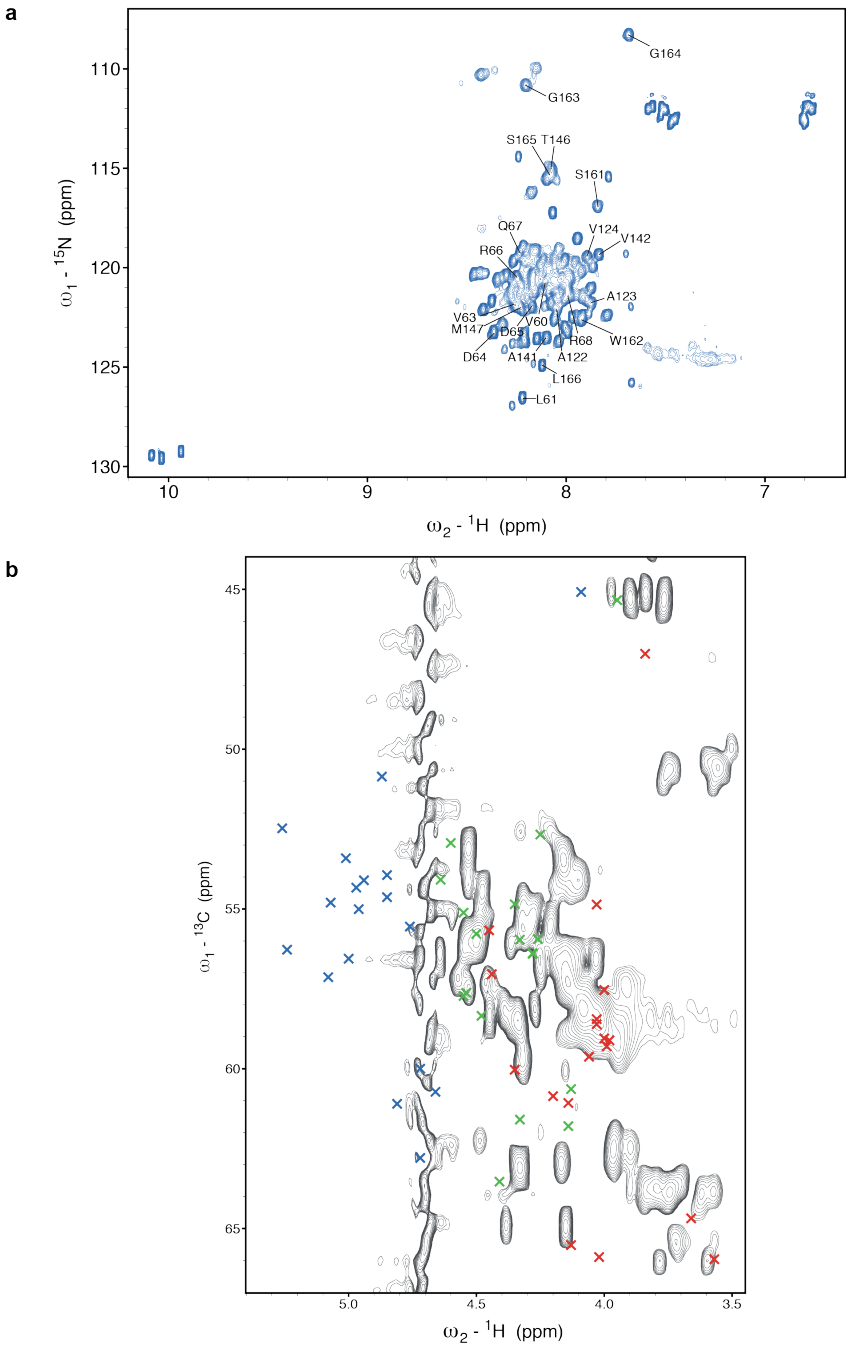

Figure 3. Structural characterization of MAP7-MTBD (residues 59-170) by NMR. a) ^{15}N-HSQC spectrum of [^{13}C, ^{15}N]-labeled, free MAP7-MTBD. The assigned peaks were indicated. b) The region of Cα-Hα cross peaks in the ^{13}C-HSQC spectrum of [^{13}C, ^{15}N]-labeled, free MAP7-MTBD overlaid with chemical-shift predictions of amino

acids in different secondary structural elements; α helix: red, β strand: blue, random coil: green. The signal observed at 4.7 ppm on proton dimension along the carbon dimension is from H_2O.

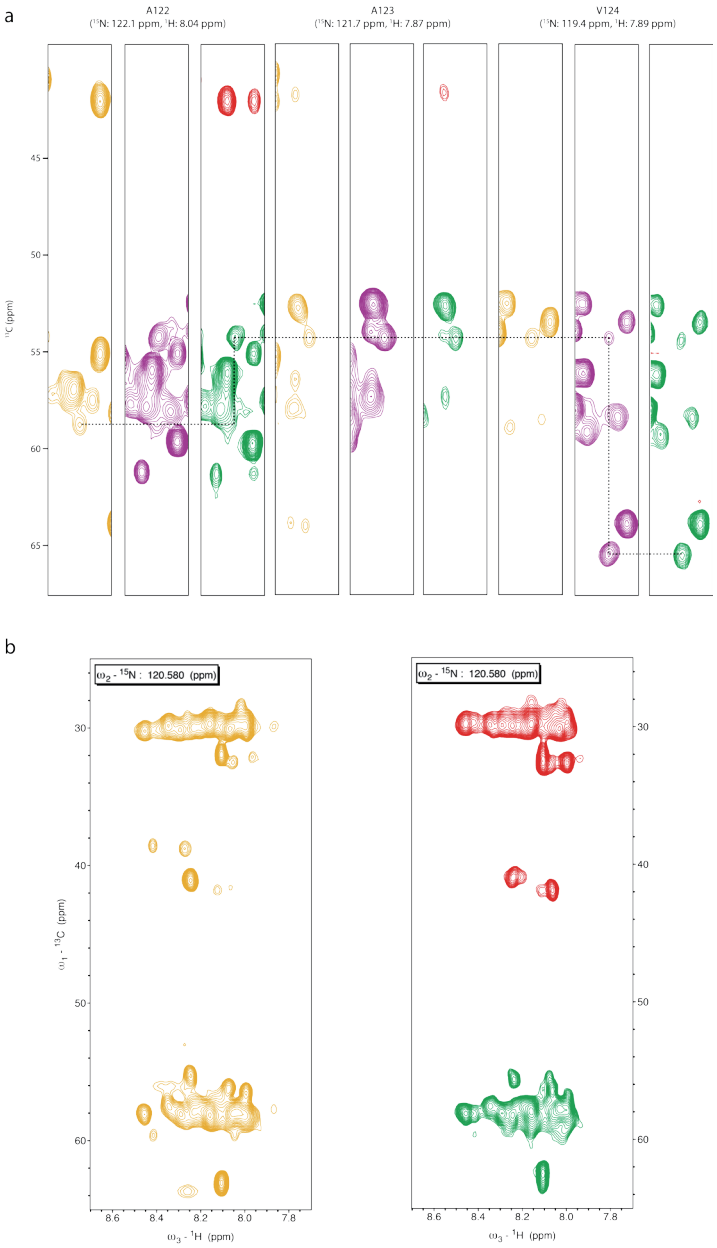

Figure 4. Solution-state assignments of free-state MAP7-MTBD. a) Strips of CBCA(CO)NH (orange), HNCA (purple) and HNCACB (green and red) of A122 to V124 are shown as examples of sequential backbone assignments of the corresponding Cα signals. b) Strips of CBCA(CO)NH (orange) and HNCACB (green and red) taken at frequency

of ^{15}N at 120.58 ppm. Note that the unresolved Cα and Cβ signals at approximately 58 and 30 ppm respectively did not allow us to retrieve complete sequential assignments for the whole MAP7-MTBD.

Residue	Cα (ppm)	Cβ (ppm)	H^N (ppm)	N (ppm)
P59	63.07	31.93	-	-
V60	62.26	32.60	8.11	120.7
L61	54.95	42.55	8.22	126.5
R62	56.14	30.62	-	-
V63	62.79	32.74	8.23	121.9
D64	54.43	41.19	8.36	123.3
D65	55.30	41.20	8.17	121.9
R66	58.26	30.03	8.24	120.5
Q67	57.58	28.64	8.23	119.3
R68	58.22	30.13	8.01	121.6
R121	58.80	30.04	-	-
A122	54.38	18.32	8.04	122.1
A123	54.39	18.34	7.87	121.7
V124	65.51	32.25	7.89	119.4
E140	57.57	29.81	-	-
A141	53.62	18.81	8.10	123.5
V142	63.95	32.33	7.83	119.3
R145	57.03	30.59	-	-
T146	62.99	69.67	8.07	115
M147	-	-	8.23	122
W160	57.19	29.45	-	-
S161	58.31	63.91	7.84	116.8
W162	57.51	29.45	7.92	122.6
G163	45.46	-	8.20	110.8
G164	45.19	-	7.68	108.2
S165	58.38	64.10	8.07	115.4
L166	53.22	41.77	8.12	124.9

Table 1. List of resonance assignments of [^{13}C, ^{15}N] labeled, free MAP7-MTBD.

To further understand the structure of MAP7-MTBD at the residue-specific level, we carried out 3D HNCA, HNCACB and CBCA(CO)NH experiments in order to obtain backbone assignments for MAP7-MTBD (Figure 4a). However, due to the particular primary and secondary structure of this protein, there are two difficulties in obtaining fully assigned data. Firstly, as shown in Figure 3, the signal dispersion among the N-H and C-H correlations is limited due to the secondary structure of MAP7-MTBD, which leads to limited spectral resolution of

within the 3D spectra (Figure 4b). Secondly, the amino distribution of MAP7-MTBD is highly redundant. Among the 112 residues, more than 50% of the entire sequence is given by three residue types, i.e., 25 arginine, 22 glutamate and 10 lysine residues (Figure 1b). Therefore, the chemical shifts of Cα and Cβ are similar and the peaks highly overlap. However, the regions that contain unique sequential residues still allowed us to obtain backbone assignments for 27 residues given in Table 1 (see also Figure 3a).

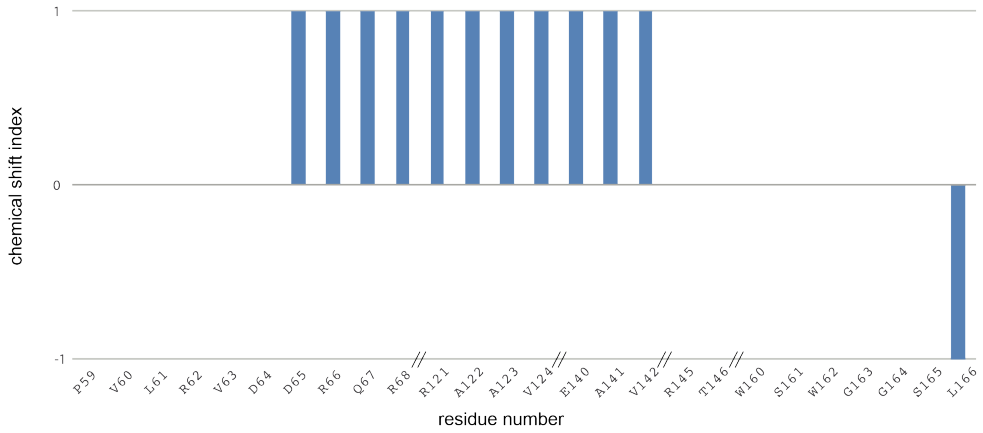

Figure 5. Chemical-shift index (CSI) for the assigned residues of MAP7-MTBD from solution-state NMR derived from ^{13}Cα chemical shifts. The CSI plot is generated based on the protocol from ref[13]. At least four consecutive CSI values of 1 indicate α helix and a minimum of three consecutive CSI values of -1 indicate β strand, remaining regions that were not identified as α helix or β strand are defined as random coil.

We then analyzed the chemical-shift values for the assigned residues. By comparing the value differences of assigned Cα chemical shifts to the reference values using the Chemical-Shift Index (CSI) protocol, we could identify and locate secondary structures for the assigned residues based on the CSI values (CSI=1: α helix; CSI=-1: β strand; CSI=0: random coil) (Figure 5). From the CSI profile we identified that both N- and C-termini of MAP7-MTBD are unstructured. For the C-terminus, we found that at least between W160 and L166 are unstructured (Figure 5 and Figure 1b). As for the N-terminus, the unstructured tail starts from P59 and until D64. The CSI profile showed that the first α helix starts at D65 that is in agreement with our secondary structural prediction (Figure 1b), while partial assignments between R121 and V124, E140 and V142 also exhibited α-helical propensity (Figure 5 and Figure 1b). Taken together, our data show MAP7-MTBD consists of unstructured terminal tails and it is a helical domain, which is in

agreement with the secondary structural predictions from previous studies (Figure 1b and ref[3-4]).

ssNMR revealed MAP7-MTBD remains highly helical but potentially adopts conformational changes upon binding MTs

Next we investigated the binding mode of MAP7-MTBD to MTs by using ssNMR. To prepare the sample for ssNMR measurements, a microtubule pelleting assay was first performed to optimize the molar ratio of MAP7-MTBD:MTs, as full decoration of MAP7-MTBD on MTs (Figure 6) would maximize sensitivity in our ssNMR experiments. Control samples with either only MTs or MAP7-MTBD clearly showed that taxol-stabilized MTs were in the pellet fraction while MAP7-MTBD did not precipitate in isolation and stayed in the supernatant. Subsequently, we used an assay with different molar ratios of MAP7-MTBD:MTs which revealed that unbound MAP7-MTBD appeared in the supernatant when a molar ratio of MAP7-MTBD:MTs=2:1 was used (Figure 6, lane 12) indicating that under this condition MTs were fully decorated with MAP7-MTBD. Hence we utilized this molar ratio to prepare the sample for ssNMR measurements.

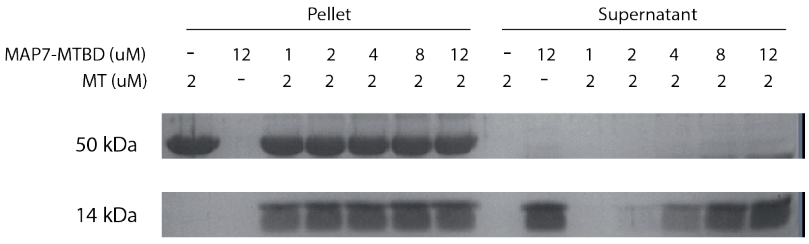

Figure 6. MT pelleting assay with MAP7-MTBD analyzed by SDS-PAGE. The MT pelleting assay was performed with different molar ratios of MAP7-MTBD:tubulin as indicated above the SDS-PAGE gel. As a result, a molar ratio of MAP7-MTBD:MTs=2:1 was used for sample preparation for ssNMR studies to allow maximum decoration of MAP7-MTBD on MTs.

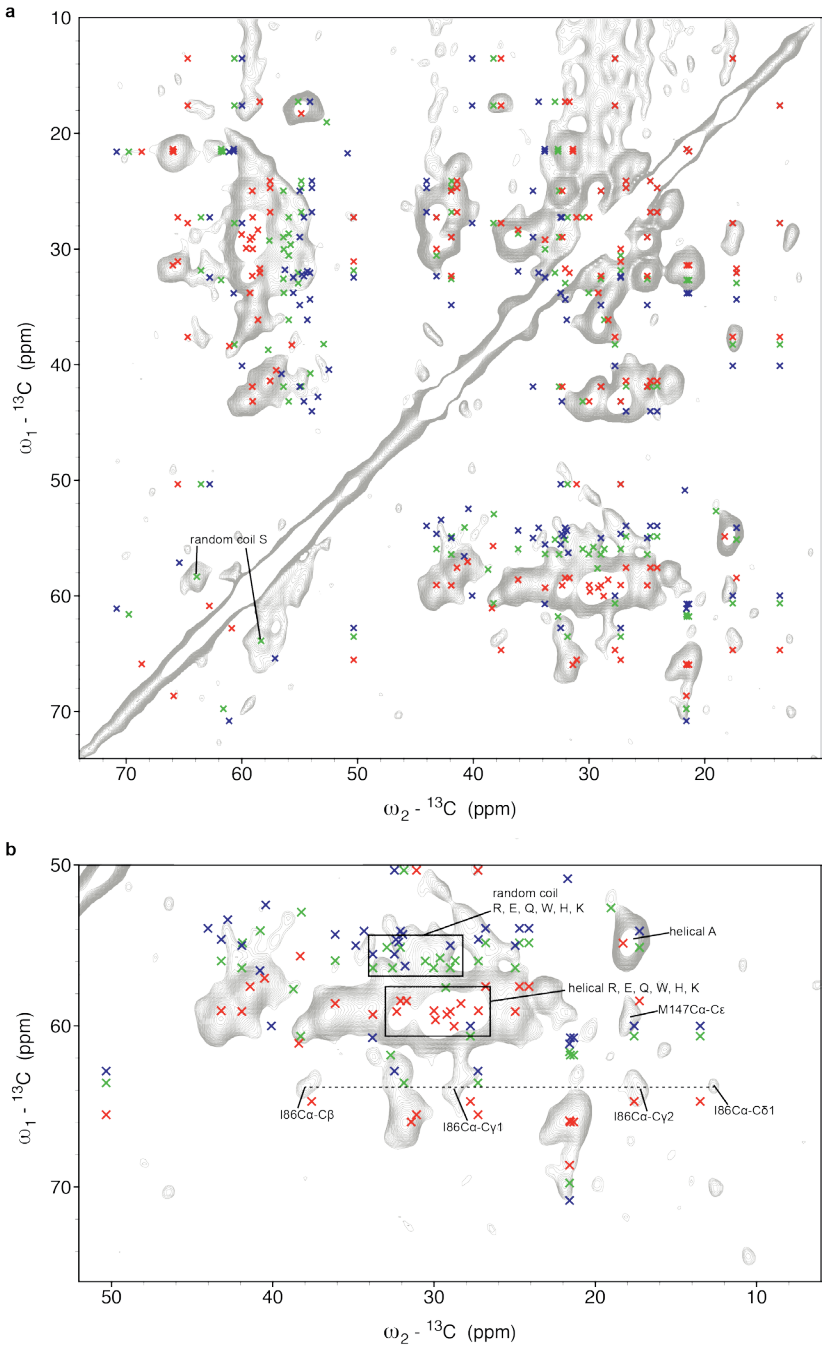

Figure 7. a) ^{13}C-^{13}C PARIS of [^{13}C, ^{15}N] labeled MAP7-MTBD in complex with MTs. The C-C mixing time was 30 ms. The chemical-shift predictions of amino acids in different secondary structural elements are overlaid onto the

spectrum; α helix: red, β strand: blue, random coil: green. b) Zoom-in on the cross peak region from panel a showing Cα atoms correlated with other aliphatic ^{13}C atoms. The helical alanine Cα-Cβ cross peak signals, helical and random coil Cα-Cβ cross peaks of arginine, glutamate, glutamine, tryptophan, histidine and lysine residues are indicated. In addition, the cross peaks of the only one isoleucine residue (I86), and the Cα-Cε cross peak of the only on methionine residue (M147) are shown.

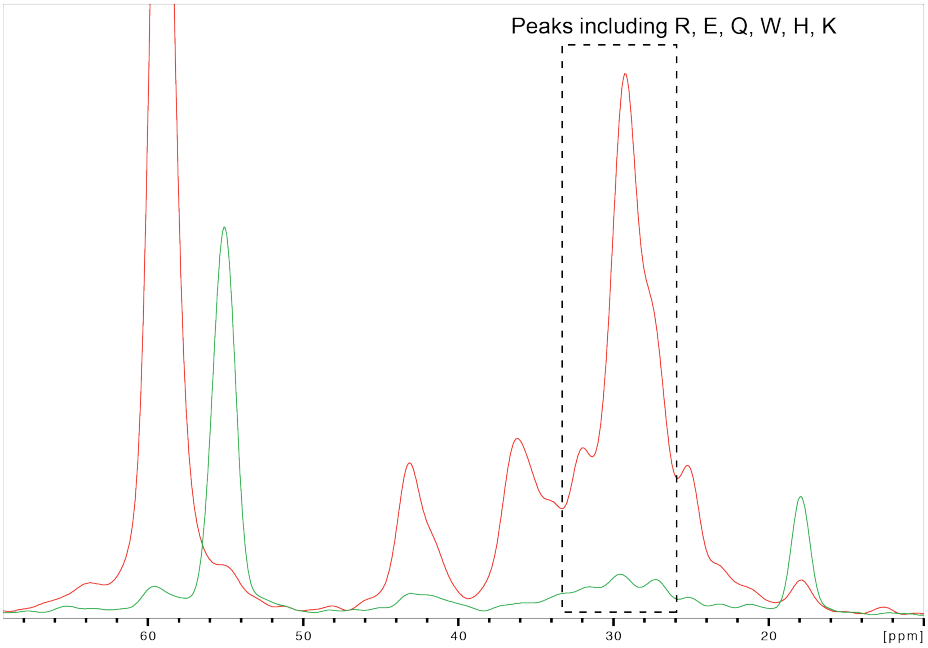

Figure 8. 1D slices on 59 ppm (red, α helical signals) and 55.6 ppm (green, random coil signals) taken from ^{13}C-^{13}C PARIS as shown in Figure 4 to compare the signal intensities of arginine, glutamate, glutamine, lysine and histidine residues in α helices and unstructured parts of the protein. MAP7-MTBD remains highly α helical upon binding to MTs.

To conduct ssNMR experiments, [^{13}C, ^{15}N]-labeled MAP7-MTBD in complex with unlabeled MTs was prepared. A ^{13}C-^{13}C PARIS experiment with 30 ms ^{13}C-^{13}C mixing time was first recorded to characterize the secondary structure of the sample (Figure 7a). To analyze the spectrum, the chemical-shift predictions of all amino acids in different secondary structures were generated from FANDAS 2.0 and overlaid onto the spectrum. Based on the predicted chemical-shift values we found that MAP7-MTBD mainly contained α-helical structures upon binding to MTs. In detail, we detected very strong signals of cross peaks at 59 ppm and around 30 ppm, which are typical for Cα and Cβ correlations related to the α-helical arginine, glutamate, glutamine, lysine and histidine residues. As mentioned before, these are the more abundant amino acids present in the

protein (Figure 7b). We also detected signals from amino acids that are located in unstructured regions. However, we found that the intensity of these signals was much weaker than the ones from the α-helices by comparing the 1D slices taken from this spectrum (Figure 8). Similarly, in the NCA spectrum, we observed most signals that are representative for α-helical regions. On the other hand, NCA backbone correlations, typically for glycine, indicated that the glycine residues that are all located in the C-terminus (Figure 1b) retained their mobility even after binding to MTs (Figure 9).

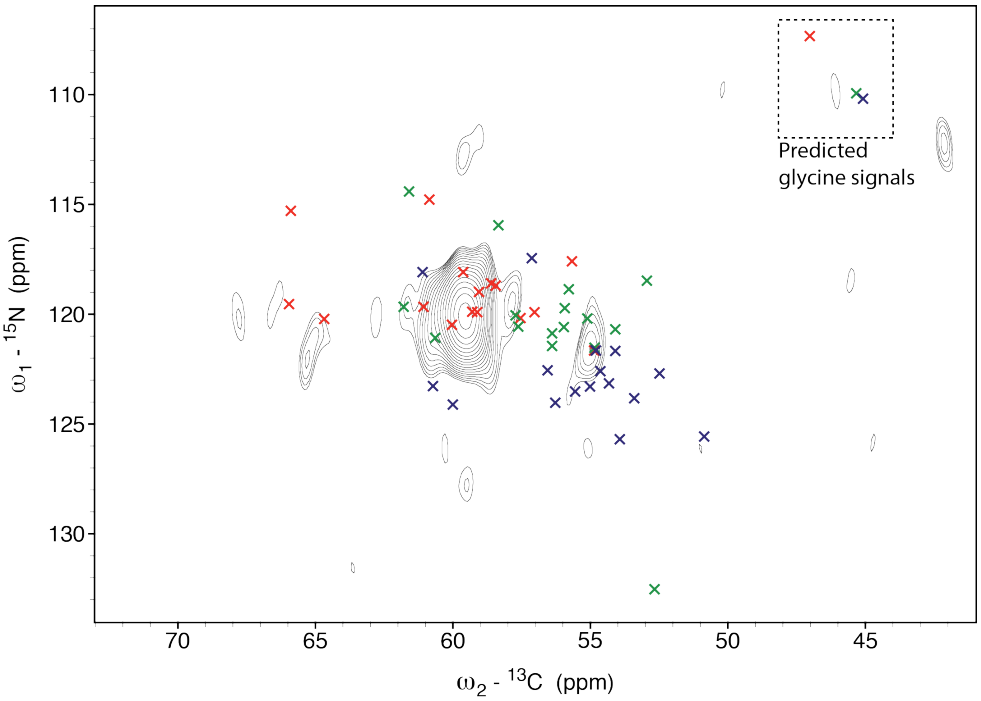

Figure 9. 2D NCA experiment of [^{13}C, ^{15}N] labeled MAP7-MTBD in complex with MTs. The chemical-shift predictions of amino acids in different secondary structural elements are overlaid onto the spectrum; α helix: red, β strand: blue, random coil: green. The predicted glycine signals are indicated in dashed-line box.

Interestingly, we obtained more information for the amino acids that are less abundant in MAP7-MTBD but exhibit enhanced spectral dispersion and reduced spectral overlap. For the alanine Cα-Cβ cross peak region, we observed strong signals at 54.8 ppm and 18 ppm that represent α-helical alanine residues (Figure 7b), while no alanine Cα-Cβ signals from β strand or random coil were detected. In addition, only one isoleucine (I86) and one methionine (M147) are present in MAP7-MTBD (Figure 1b), the ^{13}C-^{13}C correlations of this isoleucine are

clearly seen in the spectrum, indicating that it adopts an α-helical structure (Figure 7b, highlighted by a dashed line). Similarly, the Cα-Cε cross peak of the methionine is well resolved at 59.6 ppm and 17.9 ppm in the spectrum, showing that it also locates in an α-helix (Figure 7b). Moreover, there are four serine residues in MAP7-MTBD, and three of them are found in the C-terminus. In our ssNMR data we detected serine correlations at Cα-Cβ frequencies that were in good agreement with our solution-state NMR data obtained from the free MAP7-MTBD signals (Figure 7a). Given the fact that signals from glycine residues were not detected in the NCA experiment demonstrating that they are flexible (Figure 9), the observed unstructured serine signals should be related to S161 while S165 and S169 remained mobile (Figure 1b). Taken together, the findings suggest that the intrinsically disordered C-terminus of MAP7-MTBD remains partially flexible until probably S161 that was detected in the dipolar-based experiments when the MAP7-MTBD/MT complexes were formed (Figure 7a), indicating that this region became rigidified upon binding to MTs. Therefore, our ssNMR data demonstrated that the C-terminal tail of MAP7-MTBD is partially stabilized by MTs. While the spectral resolution of a fully [^{13}C, ^{15}N]-labeled sample did not allow us to retrieve sequential assignments of the protein, we could perform a global analysis of the secondary structure by zooming in distinct 1D slices (Figure 8) that are characteristic for α-helical (red) and random coil (green) residues of arginine, glutamate, glutamine, tryptophan, histidine and lysine. By simple integration of the corresponding signal regions (indicated by dashed lined box), we obtained a signal intensity ratio of random coil ($I_{r.c}$) versus α-helix ($I_{\alpha-helix}$) that is 0.118. Interestingly, based on the secondary structure prediction (Figure 1b), the ratio of the numbers of arginine, glutamate, glutamine, tryptophan, histidine and lysine residues in random coil (8) and α-helical (65) structures gave a similar value (0.123). We therefore conclude that the protein is, on the secondary structural level, characterized by a high content of α-helical segments.

Additionally, there is only one threonine residue in MAP7-MTBD (T146) (Figure 1b), which has been assigned from solution-state NMR. The chemical-shift value showed that it is likely that T146 adopts a random coil structure in the free state (Table 1 and Figure 5). As for the bound-state MAP7-MTBD, the threonine signal was not clearly detected in the ^{13}C-^{13}C PARIS with 30 ms ^{13}C-^{13}C mixing time, most likely due to low sensitivity or efficiency of the ^{13}C-^{13}C mixing. We therefore recorded another ^{13}C-^{13}C PARIS experiment using 120 ms ^{13}C-^{13}C mixing time.

Surprisingly, compared with the solution-state assignment of T146, we did not observe cross peak in the corresponding position in ssNMR experiments (Figure 10, crosses with T146Cα-Cβ and T146Cβ-Cα labels). Instead, a cross peak of 68.7 ppm and 65 ppm was detected, which indicated a helical threonine signal (Figure 10, highlighted boxes). Hence, we found a difference of approximately 2 ppm for the Cα chemical shifts between the free- and bound-state MAP7-MTBD. This chemical-shift perturbation is most likely due to the interaction with MTs, which might be an indication that MAP7-MTBD adopts conformational changes in this region upon binding to MTs, leading to an extension of the α-helical regions of this protein.

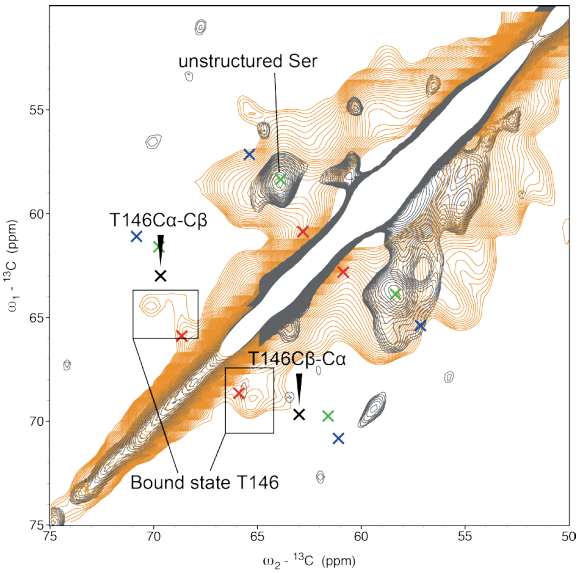

Figure 10. Zoom-in on serine and threonine Cα-Cβ regions in the ^{13}C-^{13}C PDSD spectra of [^{13}C, ^{15}N] labeled MAP7-MTBD in complex with MTs with 30 ms (gray) and 120 ms (orange) ^{13}C-^{13}C mixing times. Chemical-shift predictions of amino acids in different secondary structural elements are indicated with same color coding as Figure 7. The solution-state assignments of T146 in the unbound state were overlaid onto the spectra.

Discussion

Previous studies of MAP7 protein family members have shown their importance for MT binding, regulation of kinesin-1 and their competing role in Tau binding to MTs. In order to understand the mechanisms of the interactions between MAP7 proteins, MTs, kinesin-1 and even Tau, we here carried out an

initial study to decipher the structural elements describing human MAP7-MTBD and its binding mode to MTs. Firstly, solution-state NMR allowed us to obtain partial backbone assignments of free MAP7-MTBD and understand the structural elements of the assigned regions (Tabel 1, Figure 5 and Figure 11, upper panel). We found that MAP7-MTBD is a largely α-helical protein fragment flanked by two unstructured termini. While the C-terminal tail is unstructured until W160, the N-terminal tail starts from the N-terminus to D64 according to our data. The first α-helix starts at D65, and another region between A122 and V124 also exhibits α-helical propensity based on the backbone chemical-shift values. To further characterize the structure of MAP7-MTBD upon binding to MTs, we conducted ssNMR experiments on [^{13}C, ^{15}N]-labeled MAP7-MTBD in complex with MTs. Our ssNMR data showed that MAP7-MTBD adopts a secondary structure that shows a large extent of α-helical structure upon binding to MTs (Figure 7 and 8). For example, our data indicate that the regions from L81 to V87, R94 to R96, and E140 to V142 are α-helical (Figure 11, lower panel).


```
      60          70          80          90          100         110         120
free  PV LRVDDRQRLA RERREEREKQ LAAREIVWLE REERARQHYE KHLEERKKRL EEQRQKEERR
bound PV LRVDDRQRLA RERREEREKQ LAAREIVWLE REERARQHYE KHLEERKKRL EEQRQKEERR

              130         140         150         160         170
free  RAAVEEKRRQ RLEEDKERHE AVVRRTMERS QKPKQKHNRW SWGGSLHGSP
bound RAAVEEKRRQ RLEEDKERHE AVVRRTMERS QKPKQKHNRW SWGGSLHGSP
```

Figure 11. Secondary structural elements of free- and bound-state MAP7-MTBD as seen in NMR experiments. The residues found in α helices (red) and unstructured parts (green) are indicated. Residues with no available data due to spectral crowding are labeled in black.

Interestingly, compared to our solution-state NMR data, we also found that MAP7-MTBD behaves differently after binding to MTs. First, the C-terminal tail of MAP7-MTBD remains unstructured when it is bound to MTs. The absence of glycine signals in the NCA experiment indicated that the glycine residues in the C-terminal tail remain flexible upon binding to MTs (Figure 9). However, the presence of the serine signal from the C-terminal tail in our dipolar-based experiments indicated that most likely S161 was rigidified by MTs due to the interaction (Figure 7a and 10). Therefore, the C-terminal tail of MAP7-MTBD is likely partially involved in the MT binding. Second, we observed a significant chemical-shift difference for T146 upon interaction of MTs compared to the free MAP7-MTBD. This can be explained that T146 potentially undergoes conformational changes upon binding to MTs. Due to the unresolved peaks in the

^{15}N-HSQC spectrum, it is difficult to compare the peak intensity of T146 to the peak of its neighbor (M147) and conclude whether the chemical exchange of T146 is a slow exchange in solution. Additional experiments such as CPMG and CEST (as shown in Chapter 3) will help us to understand better the dynamical property of T146. Based on the secondary structure prediction and solution-state NMR data of MAP7-MTBD and as well as observations from the bound-state MAP7-MTBD in ssNMR, we propose a model that MAP7-MTBD adopts a structure of two α-helices with a short hinge (from R144 to T146) in between and unstructured termini in solution when MTs are not presence (Figure 12a). Upon binding to MTs, the short hinge becomes more α-helical, which leads MAP7-MTBD to adopt a one-long-α-helical structure (Figure 12b). In addition, MAP7-MTBD is abundant with charged amino acids, and the distribution of these amino acids results in one side that is more positively charged while the other side more negatively charged in the proposed bound-state structure (Figure 13a). Interestingly, the helices H12 of both tubulin subunits are highly negatively charged (Figure 13b). Therefore, this area might be a binding region for MAP7-MTBD. Notably, MAP7-MTBD competes the MT binding with Tau, while it was known that Tau binds along protofilament of MTs and interacts with both tubulin helix H12 and the C-terminal tails[15]. Therefore, the tubulin C-terminal tails might also be an important binding region for MAP7-MTBD binding and where MAP7 and Tau compete for. Moreover, as the WSW motif (W160 to W162) in the C-terminus of MAP7-MTBD is relatively conserved (Figure 1c), these two tryptophan residues might play a role in the MT binding to allow steric interactions of the aromatic rings. Further studies, for example involving amino-acid specific isotope labeling[16], mutagenesis, and isotope labeling of MTs will be needed to elucidate additional interactions between MTs and MAP7 by ssNMR.

Importantly, unlike proteins studied in the previous chapters, i.e, CAMSAP CKK domains, the primary structure of MAP7-MTBD is dominated by four amino acids and the secondary structure is largely α-helical. Both aspects complicate the structural analysis using uniformly labeled NMR samples. Therefore, to better understand the binding mechanism of MAP7-MTBD with MTs, NMR-based approaches involving tailored isotope-labeling and the use of 3D or even 4D ssNMR could be applied. In addition, such studies could be complemented by crystallographic and cryo-EM data studies to reveal further information about the structure of free MAP7-MTBD and the MAP7-MTBD/MT

complex. Tailored labeling strategies in ssNMR could also help to zoom in certain regions[17] that are close to the binding interface and probe the interaction dynamics and local structural alterations.

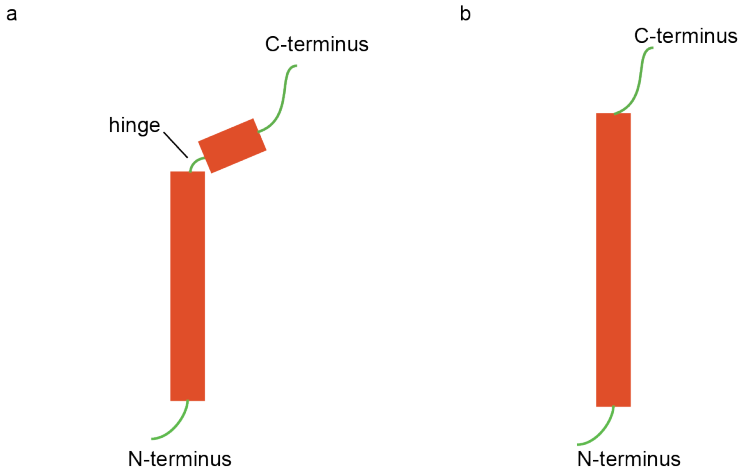

Figure 12. Proposed models for a) free-state and the b) MT-bound state MAP7-MTBD. Unstructured regions are indicated with green lines and α-helices are indicated with red boxes.

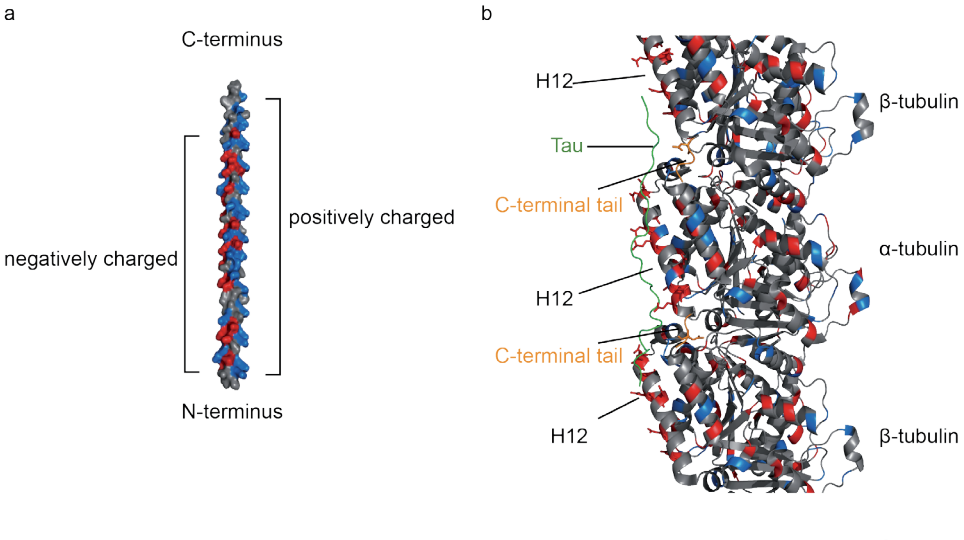

Figure 13. Charged amino acid distribution of a) proposed model of the bound-state MAP7-MTBD and b) MT-Tau complex (PDB: 6CVN). In panel b, Tau is labeled in green. The side chains of the negatively charged amino

acids in helices H12 and the C-terminal tails of tubulin are indicated. The partially seen tubulin C-terminal tails are labeled in orange.

References:

[1] a) J. C. Bulinski, A. Bossler, *Journal of Cell Science* **1994**, *107*, 2839; b) D. Masson, T. E. Kreis, *The Journal of Cell Biology* **1993**, *123*, 357.

[2] T. Metzger, V. Gache, M. Xu, B. Cadot, E. S. Folker, B. E. Richardson, E. R. Gomes, M. K. Baylies, *Nature* **2012**, *484*, 120.

[3] S. R. Tymanskyj, B. H. Yang, K. J. Verhey, L. Ma, *eLife* **2018**, *7*, e36374.

[4] S. Yadav, P. J. Verma, D. Panda, *PLOS ONE* **2014**, *9*, e99539.

[5] P. J. Hooikaas, M. Martin, T. Mühlethaler, G.-J. Kuijntjes, C. A. E. Peeters, E. A. Katrukha, L. Ferrari, R. Stucchi, D. G. F. Verhagen, W. E. van Riel, I. Grigoriev, A. F. M. Altelaar, C. C. Hoogenraad, S. G. D. Rüdiger, M. O. Steinmetz, L. C. Kapitein, A. Akhmanova, *The Journal of Cell Biology* **2019**, *218*, 1298.

[6] B. Y. Monroy, D. L. Sawyer, B. E. Ackermann, M. M. Borden, T. C. Tan, K. M. Ori-McKenney, *Nature Communications* **2018**, *9*, 1487.

[7] E. Chevalier-Larsen, E. L. F. Holzbaur, *Biochimica et Biophysica Acta (BBA) - Molecular Basis of Disease* **2006**, *1762*, 1094-1108.

[8] A. Drozdetskiy, C. Cole, J. Procter, G. J. Barton, *Nucleic Acids Research* **2015**, *43*, W389-W394.

[9] H. Ashkenazy, S. Abadi, E. Martz, O. Chay, I. Mayrose, T. Pupko, N. Ben-Tal, *Nucleic Acids Research* **2016**, *44*, W344-W350.

[10] R. N. de Jong, M. A. Daniëls, R. Kaptein, G. E. Folkers, *Journal of Structural and Functional Genomics* **2006**, *7*, 109-118.

[11] M. Weingarth, D. E. Demco, G. Bodenhausen, P. Tekely, *Chemical Physics Letters* **2009**, *469*, 342-348.

[12] S. Narasimhan, D. Mance, C. Pinto, M. Weingarth, A. M. J. J. Bonvin, M. Baldus, in *Protein NMR: Methods and Protocols* (Ed.: R. Ghose), Springer New York, New York, NY, **2018**, pp. 111-132.

[13] D. S. Wishart, B. D. Sykes, *Journal of Biomolecular NMR* **1994**, *4*, 171-180.

[14] N. Guex, M. C. Peitsch, T. Schwede, *ELECTROPHORESIS* **2009**, *30*, S162-S173.

[15] E. H. Kellogg, N. M. A. Hejab, S. Poepsel, K. H. Downing, F. DiMaio, E. Nogales, *Science* **2018**, *360*, 1242.

[16] M. Renault, A. Cukkemane, M. Baldus, *Angewandte Chemie-International Edition* **2010**, *49*, 8346-8357.

[17] M. Kaplan, A. Cukkemane, G. C. P. van Zundert, S. Narasimhan, M. Daniëls, D. Mance, G. Waksman, A. M. J. J. Bonvin, R. Fronzes, G. E. Folkers, M. Baldus, *Nature Methods* **2015**, *12*, 649.

CHAPTER 5

5

A general approach to study structure and interactions of human microtubules by solid-state NMR

Abstract

Microtubules are important components of the eukaryotic cytoskeleton. Their structural organization is regulated by nucleotide binding and many microtubule-associated proteins. Cryo-EM and X-ray crystallography have provided increasingly detailed views of microtubule structure and binding modes with different regulators. NMR carries the potential to complement such studies by probing atomic structure as well as interaction dynamics and local, time-dependent structural alterations. However, the direct NMR analysis of microtubules has so far been precluded by the low tubulin yield with current purification protocols. Here, we present a protocol that yields 1 mg pure microtubules from 1 L of HeLa cell culture for preparation of isotope enriched, functional human microtubules, suitable for solid-state NMR and potentially for solution-state NMR studies. Using fast magic angle spinning experiments and dynamic nuclear polarization, we could probe microtubules at atomic level. Our data are compatible with a rigid, well folded tubulin subunits in microtubules while the loop regions exhibit sizable dynamics. In addition, our data allowed us to directly detect the molar ratio of 1:1 for GTP and GDP which are critical for the microtubule assembly cycle and revealed disordered, flexible tubulin tails whose dynamics is changed upon binding to the MT-binding protein MAP7-MTBD.

Introduction

In eukaryotic cells, microtubules (MTs) are cytoskeletal polymers essential for many biological processes, including cell division, migration, polarization and intracellular trafficking. MTs are assembled from α/β-tubulin heterodimers and are intrinsically polarized, with the highly dynamic, β-tubulin-exposed plus end, which rapidly switches between growth and shrinkage in a process termed 'dynamic instability'[1]. The dynamic instability of MTs is caused by GTP binding and hydrolysis on tubulin dimers. Many MT-associated proteins (MAPs) regulate MT dynamics by interacting with MT lattices or MT ends[2]. In addition, the C-terminal tails of tubulin have been found to be flexible and undergo a variety of post-translational modifications (PTMs), including detyrosination, acetylation, polyglycylation and polyglutamylation, which are associated with different cellular processes and human disorders[3].

Since MTs are critical for numerous cellular processes, understanding how MTs and MAPs interact and function, especially at the atomic level, becomes very important. With recent developments in cryo-Electron Microscopy (EM), substantial progress has been made in our structural understanding of MTs and their interaction partners[4], including a recent 3.2 Å cryo-EM reconstruction of the MAP Tau interaction with MTs[5]. However, dynamic regions of tubulin, including the unstructured C-terminal tails, have remained elusive in ensemble averages due to their flexibility. X-ray crystallography can provide information on the tubulin interactions[6], yet studying the molecular mechanisms of how different MAPs bind and affect MT dynamics remains challenging due to the filamentous nature of MTs and MAP-MT assemblies. Solution-state NMR has been used to detect the PTMs on the C-terminal tubulin tails and to characterize interactions between MAPs and tubulin[7]. However, the rigid tubulin body and the intact MTs cannot be directly studied by solution-state NMR due to their molecular size. Magic angle spinning (MAS) solid-state NMR (ssNMR) can overcome this limitation potentially to provide structural and dynamical information complementary to cryo-EM and X-ray studies. This technique has been used to study MAPs and MT-binding drugs in complex with MTs at atomic resolution[8]. In addition, recent advances in dynamic nuclear polarization (DNP)[9] and ^{1}H detection have expanded the potential of ssNMR to provide detailed insight into the structure and dynamics of complex biomolecules including proteins located in native cellular membranes[10] or embedded in nucleosomes[11]. In spite of the progress in producing isotope-labeled tubulin for solution-state NMR studies[7a], extending such experiments to MTs has failed so far. Firstly, production of recombinant, functional α/β-tubulin dimers from bacteria, which are commonly used to obtain labeled proteins, has not been possible, most likely due to the lack of chaperones and cofactors for tubulin folding and dimerization[12]. In addition, existing protocols for tubulin purification from mammalian cells[13] did not provide sufficient yields to obtain isotope-labeled MTs for NMR studies.

Here, we use a modified protocol to produce milligram quantities of functional human MTs with isotope enrichment from mammalian cell culture. The combination of this approach with fast MAS, ^{1}H detection and dynamic nuclear polarization (DNP) allowed us to conduct ssNMR experiments to study structure and interactions of MTs with MAPs at the atomic level.

Materials and methods

[^{13}C, ^{15}N] labeling of HeLa S3 cells. The HeLa S3 cell line (ATCC® CCL2.2™) was used for culturing. [^{13}C, ^{15}N] labeled DMEM medium was prepared in the same way as described in a previous study[10b] except that we used 3.5 g/L glucose in order to maintain cell viability in suspension culture. The cells were first cultured in the labeled medium on 2 150 mm cell culture dishes, and then transferred into 12 dishes with the same medium. When the culture reached a confluence of ~80% on the plates, cells were trypsinized and transferred into 2 L labeled medium and cultured in 7 1L Erlenmeyer shaker flasks (Corning) until the cell density reached ~1.2-1.5 x 10^6/mL. Cells were then harvested by centrifugation at 500 x g for 20 min at 4°C. The cell pellet was collected and resuspended in PBS and centrifuged again at 500 x g for 15 min at 4°C and used for microtubule (MT) preparation.

Preparation of [^{13}C, ^{15}N] MTs for ssNMR measurement. The purification of Taxol-stabilized microtubules (MTs) was performed based on the previously published protocols[14] with minor modifications. Harvested cells were first resuspended with 1 g cell/mL lysis buffer (80 mM PIPES pH 6.8, 1 mM EGTA, 1 mM $MgCl_2$, 1 mM β-mercaptoethanol, 1 mM PMSF and protease inhibitors (Roche) and lysed on ice by passing through a French Press homogenizer 3 times at 1000 psi. Lysed cells were then spun down at 120,000 x g at 4°C for 30 min and the supernatant was collected. The supernatant was centrifuged again at 5,000 x g at 4°C for 15 min to remove the remaining cell debris and then a half volume of glycerol and 1 mM GTP were added and mixed well. MT polymerization was carried out by incubating the mixture at 30°C for 30 min. Subsequently, the crude MT pellet was spun down at 150,000 x g (Type 70.1 Ti, Beckman Coulter) at 30°C for 30 min and placed on ice. The pellet was then resuspended in BRB80 buffer (80 mM PIPES pH 6.8, 1 mM EGTA, 1 mM $MgCl_2$) supplemented with protease inhibitors and kept on ice for 30 min to allow for MT depolymerization. For a more efficient depolymerization, the solution was resuspended frequently and then centrifuged at 150,000 x g (Type 70.1 Ti, Beckman Coulter) at 4°C for 30 min, and the supernatant was collected. An equal volume of high concentration PIPES buffer (1 M PIPES pH 6.8, 10 mM $MgCl_2$, 20 mM EGTA), together with an equal volume of glycerol and 1 mM GTP were then added to the supernatant and mixed well. MT

polymerization was again performed at 30°C for 30 min. Subsequently, 20 µM Taxol (Paclitaxel, Sigma) was added to the reaction and incubated for 20 min to generate Taxol-stabilized MTs. Taxol-stabilized MTs were then spun down at 150,000 x g (TLA-55, Beckman Coulter) at 30°C for 30 min washed with BRB80 containing 20 µM Taxol and protease inhibitors.

For the DNP experiments, the MT sample was washed with BRB80 in D_2O containing 30% glycerol-d_8, 20 µM Taxol and centrifuged at 150,000 x g (TLA-55, Beckman Coulter) at 30°C for 30 min. The sample was then resuspended with the DNP radical solution, obtained by dissolving the DNP agent AMUPol[15] in 60% glycerol-d_8, 30% D_2O and 10% BRB80 with a radical concentration of 15 mM. The sample was then transferred in a Bruker 3.2 mm sapphire rotor, snap-frozen and stored in liquid nitrogen until use.

Preparation of unlabeled MAP7 MTBD in complex with [^{13}C, ^{15}N] labeled MTs. [^{13}C, ^{15}N] labeled MTs were obtained as above described. The preparation of MAP7 MTBD/MT complex was done as described in Chapter 4.

Preparation of MTs/tubulin for *in vitro* assays. Taxol-stabilized MTs were prepared in the same way as described above. Regarding the sample used in the *in vitro* dynamics assay, the preparation of tubulin was similar except that Paclitaxel was not included during the second MT polymerization. After the second MT polymerization, MTs were spun down and resuspended in ice cold BRB80 supplemented with protease inhibitors. The second depolymerization was done on ice for 30 min and then centrifuged at 150,000 x g at 4°C for 30 min. Purified tubulin was aliquoted and snap-frozen in liquid nitrogen, stored at -80°C until use.

***In vitro* assays.** MT seeds were prepared by incubating 20 µM porcine tubulin mix containing 70% unlabeled, 18% biotin-tubulin and 12% HiLyte488-tubulin with 1 mM guanylyl-(α,β)-methylenediphosphonate (GMPCPP) at 37°C for 30 min. Polymerized MTs were separated from the mix by centrifugation in an Airfuge for

5 min. MTs were subjected to one round of depolymerization and polymerization in 1 mM GMPCPP, and the final MT seeds were stored in MRB80 buffer (80 mM K-PIPES pH 6.8, 1 mM EGTA, 4 mM $MgCl_2$) containing 10% glycerol.

In vitro reconstitution assays were performed in flow chambers assembled from microscopy slides and plasma cleaned coverslips. Assays with Taxol-stabilized HeLa MTs were performed in MRB80 pre-washed chambers. The *in vitro* reaction mixture consisted of 15 µM HeLa MTs (stabilized by 20 µM Taxol) that were either before or after MAS at 44 kHz for 24 hrs, 150 nM MAP7D3-MTBD, 50 mM KCl, 0.1% Methylcellulose, 0.5 mg/ml κ-casein, 1 mM GTP, oxygen scavenging system (20 mM glucose, 200 µg/ml catalase, 400 µg/ml glucose-oxidase, 4 mM DTT). After centrifugation in an Airfuge for 5 minutes at 119,000 x g, the reaction mixture was added to the flow chamber and sealed with vacuum grease.

Dynamic MT assays were performed in above described flow chambers. The chambers were treated with 0.2 mg/ml PLL-PEG-biotin (Surface Solutions, Switzerland) in MRB80 buffer for 5 min. After washing with the assay buffer, they were incubated with 1 mg/ml NeutrAvidin for 5 min. MT seeds were attached to the biotin-NeutrAvidin links and incubated with 1 mg/ml κ-casein. The in vitro reaction mixture consisted of 15 µM HeLa tubulin (quantified using BSA standard), 20nM GFP-EB3 and 0.5 µM rhodamine-labeled porcine brain tubulin, 50 mM KCl, 0.1% Methylcellulose, 0.5 mg/ml κ-casein, 1 mM GTP, oxygen scavenging system (20 mM glucose, 200 µg/ml catalase, 400 µg/ml glucose-oxidase, 4 mM DTT). After centrifugation in an Airfuge for 5 minutes at 119,000 g, the reaction mixture was added to the flow chamber containing the HiLyte-488 MT seeds and sealed with vacuum grease. HiLyte488- and rhodamine-tubulin were purchased from Cytoskeleton Inc.

All *in vitro* experiments were conducted at 30°C. Data were collected using Total Internal Reflection Fluorescence (TIRF) microscopy on an inverted research microscope Nikon Eclipse Ti-E (Nikon) with the perfect focus system (PFS) (Nikon), equipped with Nikon CFI Apo TIRF 100 × 1.49 N.A. oil objective (Nikon, Tokyo, Japan), Photometrics Evolve 512 EMCCD (Roper Scientific) and Photometrics CoolSNAP HQ2 CCD (Roper Scientific) and controlled with MetaMorph 7.7 software (Molecular Devices, CA). The microscope was equipped

with TIRF-E motorized TIRF illuminator modified by Roper Scientific France/PICT-IBiSA, Institut Curie. For excitation lasers we used 491 nm 100 mW Stradus (Vortran), 561 nm 100 mW Jive (Cobolt) and 642 nm 110 mW Stradus (Vortran). We used an ET-GFP 49002 filter set (Chroma) for imaging of proteins tagged with GFP and an ET-mCherry 49008 filter set (Chroma) for imaging X-Rhodamine labelled tubulin amd mCherry-labeled MT-binding domain of MAP7D3. For simultaneous imaging of green and red fluorescence we used an Evolve512 EMCCD camera (Photometrics), ET-GFP/mCherry filter cube (59022, Chroma) together with an Optosplit III beamsplitter (Cairn Research Ltd) equipped with double emission filter cube configured with ET525/50m, ET630/75m and T585lprx (Chroma). To keep in vitro samples at 30°C, we used a stage top incubator (model INUBG2E-ZILCS; Tokai Hit). Images were processed using ImageJ. All images were modified by linear adjustments of brightness and contrast. Kymographs were generated using ImageJ plugin KymoResliceWide v.0.4. https://github.com/ekatrukha/KymoResliceWide; copy archived at https://github.com/elifesciences-publications/KymoResliceWide).

Transmission electron microscopy. Taxol-stabilized MTs were prepared with and without MAS spinning as described above. The protein samples were negatively stained with 2% uranyl acetate on glow-discharged carbon coated copper grids. Images were recorded on a Tecnai 20 electron microscope with a LaB6 filament, operating at 200 kV with a BM Eagle 4K CCD camera (ThermoFisher, Eindhoven, The Netherlands). Images were acquired with a defocus of approximately 5 µm. The magnification used at 19,000x resulting in an effective pixel size of 1.14 nm on the specimen level.

Solid-state NMR experiments. NMR experiments of [^{13}C, ^{15}N]-labeled MTs were performed on a standard-bore 700 MHz, a wide-bore 500 MHz as well as on 800 MHz/527 GHz DNP and a 400 MHz/263 GHz DNP systems (Bruker Biospin). NMR experiments of unlabeled MAP7 MTBD in complex with [^{13}C, ^{15}N]-labeled MTs were performed on a standard-bore 700 MHz system (Bruker Biospin). ssNMR experiments included 2D ^{13}C-^{13}C radio frequency-driven recoupling (RFDR)[16], ^{1}H-^{13}C/^{15}N HSQC and 3D ^{15}N-edited ^{1}H-^{1}H spin diffusion experiments[17] (set

temperature 270 K, MAS rate 44 kHz). The ^{13}C-^{13}C mixing was 3 ms in the RFDR experiment. The PISSARRO decoupling[18] scheme of 120 kHz was employed on the ^{1}H channel during the RFDR mixing and the detection of ^{13}C. The proton spin diffusion time was 200ms. In all proton-detected experiments, the PISSARRO decoupling scheme was applied at 11 kHz on ^{1}H, ^{13}C and ^{15}N channels. ^{31}P NMR experiment was conducted on the 500 MHz spectrometer (set temperature 290 K, MAS rate 11 kHz). The CP MAS experiment was recorded using a 100%-50% ramp on ^{1}H-channel of 95.4 kHz, and 71.7 kHz on the ^{31}P-channel, with 1.2 ms CP contact time. A SPINAL decoupling[19] of ^{1}H during the acquisition of ^{31}P was applied at 90 kHz. ^{31}P chemical shifts were referenced externally using phosphate buffer, pH 7 and set the signal at 0 ppm. The 2D ^{13}C-^{13}C proton-driven spin diffusion (PDSD)[20] was recorded on the 800 MHz/537 GHz DNP system at 100 K with MAS rate of 10.5 kHz. The ^{1}H-^{13}C CP transfers were carried out with an 80%-100% ramp on ^{1}H channel of 71.7 kHz and 52.5 kHz on the^{13}C-channel with 100 µs CP contact time. The ^{13}C-^{13}C mixing time in spin diffusion was set to 30 ms to focus on the intra-residue correlations. The SPINAL decoupling scheme was used at 81.6 kHz on protons during the evolution and acquisition of ^{13}C. 2D DQSQ was recorded on the 400 MHz/263 GHz DNP system under 8 kHz MAS. The SPC5 mixing scheme[21] was used in these experiments and a continuous-wave decoupling at 83.3 kHz on ^{1}H channel was applied during the SPC5 mixing. The ^{1}H-^{13}C CP was performed with a 90%-100% ramp of 58.8/65.5 kHz on the ^{1}H/^{13}C-channel and 100 µs CP contact time.

Results

To purify mammalian MTs we used the HeLa S3 cell line. These cells grow not only as adherent culture but also in suspension, thereby increasing the efficiency of large-scale cultures. In addition, HeLa S3 cells express only a few tubulin isotypes[22] and mostly lack PTMs compared to, for example, brain tubulin, which is widely used in the field to study MTs[23]. Therefore, our approach should result in comparatively homogeneous samples. We isolated tubulin from cell lysates by using a polymerization and depolymerization cycle to remove contaminations (Figure 1a, b). Subsequently, we polymerized tubulin into MTs with high concentration of 1,4-Piperazinediethanesulfonic acid (PIPES) to remove MAPs binding to MTs and stabilized MTs with Taxol[24]. As demonstrated by SDS-

PAGE, Taxol-stabilized MTs showed a purity of 90% (Figure 1b). To check whether these were functional MTs, we incubated them with the fluorescently tagged MT-binding domain of MAP7 domain-containing protein 3 (MAP7D3) that binds to MT lattices[25] and found that the purified MTs were decorated by this protein fragment (Figure 1c, left panel). Transmission EM and TIRF microscopy were then employed to confirm that the MT sample does not undergo any loss of function or destruction by fast MAS ssNMR experiments (Figure 1c, right panel and Figure 1d).

We also investigated whether HeLa S3-derived tubulin can polymerize without Taxol and shows dynamic instability by preparing an additional sample without Taxol, leading to soluble tubulin after a subsequent depolymerization. The resulting tubulin was used in an *in vitro* reconstitution assay where MTs are polymerized from stable MT seeds with GFP-tagged End Binding protein 3 (EB3) as a marker for growing ends. The tubulin we prepared polymerized into MTs and showed phases of growth and shortening (Figure 1e), demonstrating that it is functional. Taken together, this protocol allowed us to purify functional tubulin from mammalian cells that could form MTs, thus providing the basis for further NMR experiments.

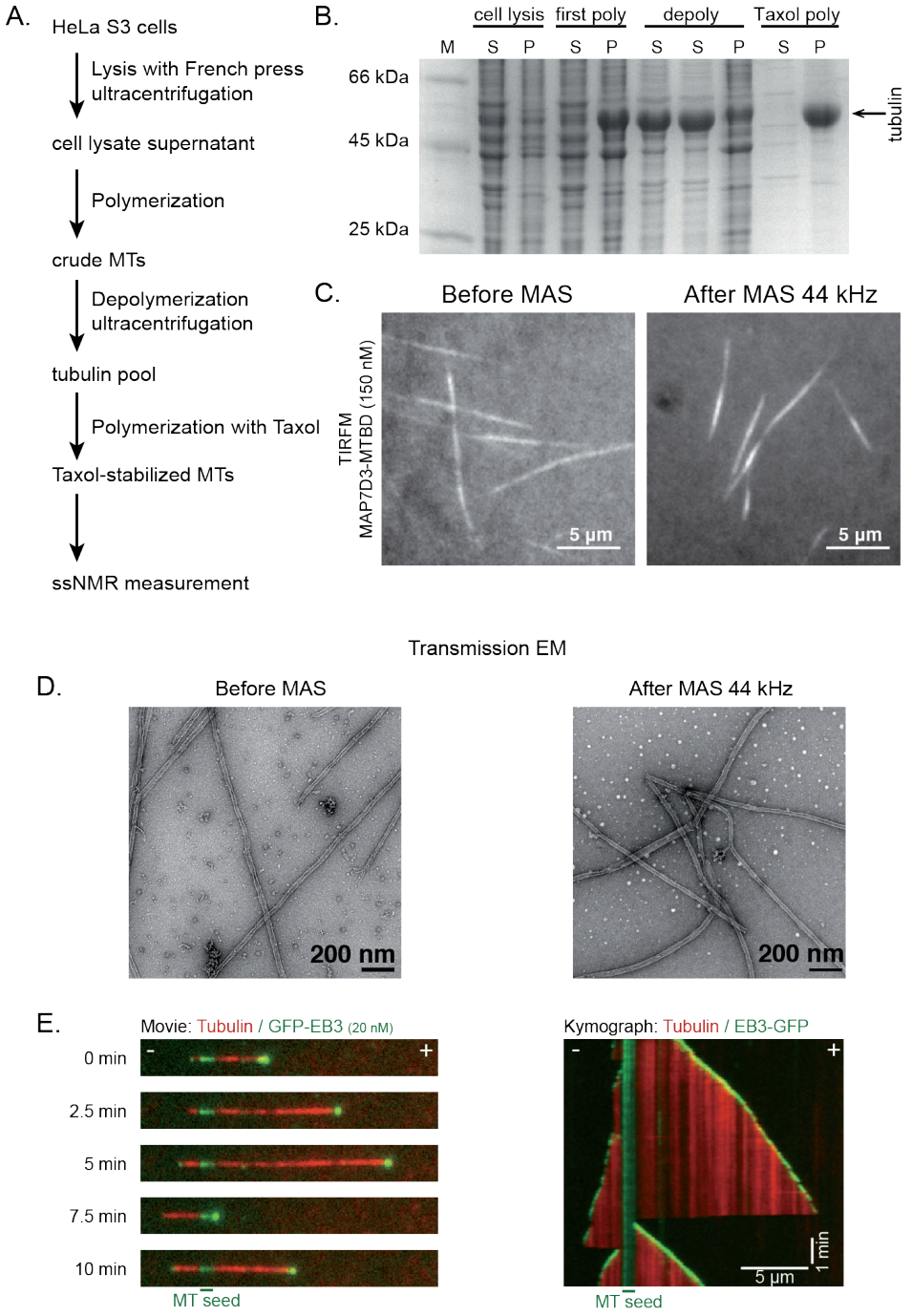

Figure 1. MT preparation from HeLa S3 cells and sample characterization. a) Schematic overview of the sample preparation. b) SDS-PAGE of samples from each purification step. M: protein marker; S: supernatant; P: pellet; first poly: first polymerization; depoly: depolymerization; Taxol poly: polymerization with Taxol. c)

Characterization of functionality of HeLa MTs after MAS NMR experiments. Taxol-stabilized MTs were incubated with purified mCherry-labeled MAP7D3-MTBD (150 nM) before or after MAS spinning and observed by TIRF microscopy. d) Characterization of morphology of HeLa MTs before and after MAS NMR experiments by EM. e) Functional characterization of purified HeLa S3 tubulin. Movie stills (left) and a kymograph (right) of an in vitro polymerized MT imaged for 10 minutes on a TIRF microscope. Time points and MT plus (+) and minus (-) ends are indicated.

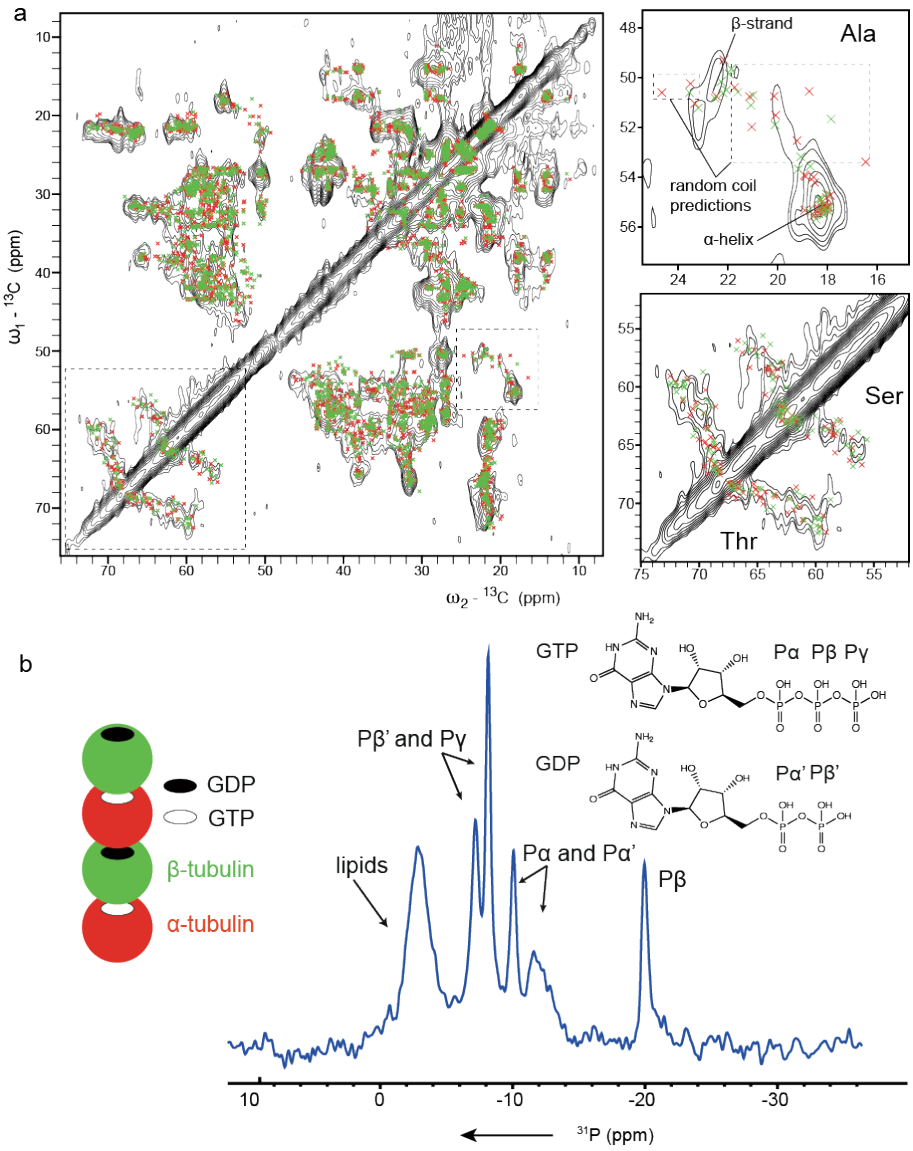

Figure 2. ssNMR spectra of [^{13}C, ^{15}N]-labeled, Taxol-MTs. a) The 2D ^{13}C-^{13}C radio frequency-driven recoupling (RFDR) experiment was performed at 270 K set temperature with a MAS rate of 44 kHz, and zoom in's on serine, threonine and alanine Cα-Cβ regions. Crosses indicate the chemical shift predictions for Taxol-MTs from

SHIFTX2[26] and FANDAS 2.0[27] based on the structure: PDB 5SYF. Red and green crosses represent predictions for α-tubulin and β-tubulin respectively. b) Schematic representation of the GTP/GDP binding to tubulin in Taxol-MTs (left), and 1D H-^{31}P CP experiment at ambient temperature with MAS rate of 11 kHz allows to observe GTP and GDP bound to MTs.

To obtain isotope-labeled MTs for ssNMR, we grew HeLa S3 cells in 2 L [^{13}C, ^{15}N]-labeled Dulbecco's Modified Eagle Medium (DMEM) and obtained approximately 2 mg isotope-labeled, Taxol-MTs using the procedure described above (Figure 1b, lane 10). The sample was then packed into a 1.3 mm MAS NMR rotor. To evaluate the sample quality, a 2D ^{13}C-^{13}C correlated spectrum was first recorded and compared to the chemical-shift predictions for Taxol-MTs (PDB ID: 5SYF) using FANDAS 2.0[27]. Overall, the spectrum agreed with *in-silico* estimates (Figure 2a, left panel). For example, in Cα-Cβ regions of serine, threonine and alanine residues, signals were observed in qualitative agreement with predictions (Figure 2a, right panel). Interestingly, alanine signals that were not observed (Figure 2a, top right) related to residues in tubulin loops, indicative of loop motion at the experimental temperature (~298 K) in our dipolar-based experiment. These observations suggested that the protein is well folded with different secondary structures. Additionally, the spectral resolution for such a large complex speaks in favor of a homogenous sample of polymerized MTs. This notion was further confirmed by ^{31}P NMR signals from nucleotides binding to MTs. In general, α/β-tubulin dimers contain two nucleotide-binding sites. The GTP molecule bound to α-tubulin is non-hydrolysable, whereas, the nucleotide bound to β-tubulin is exchangeable, and GTP is hydrolyzed to GDP upon MT polymerization[28] (Figure 2b, left). Indeed, we observed signals from both GTP and GDP in 1D ^{31}P CPMAS spectrum (Figure 2b, right) that were well resolved compared to previous results on lyophilized MTs[29]. The peak at -19.9 ppm is the signal for the Pβ of GTP. The peaks at -10.08 ppm and -11.6 ppm corresponded to Pα of GTP and GDP, while the peaks at -7.18 ppm and -8.15 ppm corresponded to the Pβ of GDP and Pγ of GTP[29-30]. By comparing the integrations of peaks of Pα of both molecules (0.659 and 0.664, respectively) and the peaks related to Pβ of GDP and Pγ of GTP (1.000 and 1.127, respectively), we can conclude that the molar ratio of GDP:GTP in our MT sample was 1:1, which is in agreement with previous studies[4a, 28] and suggested that our sample is intact. We also observed an additional broad peak at -2.7 ppm, which may result from co-purified lipids[31].

The tubulin C-terminal tails are absent in all currently available structures, presumably due to their flexible nature. To probe these flexible parts of MTs, we carried out a series of J-based NMR ^{1}H experiments as these measurements can reveal the dynamic parts within large protein complexes and aggregates[11]. A 2D ^{15}N-HSQC solid-state spectrum contained several signals with a limited spectral dispersion (Figure 3a), in line with the presence of a mobile unstructured protein region. Using additional 2D ^{13}C-HSQC (Figure 3b) and 3D ^{15}N edited ^{1}H-^{1}H spin diffusion spectra (Figure 3c, right), we could confirm that correlations observed in the ^{15}N-HSQC spectrum are mainly due to glycine, glutamate, and alanine, which are the most abundant residues in the tubulin C-terminal tails (Figure 3c, left). Specifically, on the 3D N edited ^{1}H-^{1}H spin diffusion (with 200 ms ^{1}H-^{1}H mixing time) spectrum, the cross peaks between HN and Hα are used to determine residue types and obtain sequential information. Signals of glutamate and alanine residues were confirmed by the cross peaks of HN to Hβ or Hγ. Interestingly, one glutamate NH signal showed the correlations to Hα of glycine, indicating that these residues are next to glycine residues (Figure 3c, the second strip). These are the glutamate residues in the EGE motifs as shown in the tubulin C-terminal tails, while the other glutamate peak showed no contacts to glycine Hα (Figure 3c, the third strip), demonstrating that they are the glutamate residues that are not next to glycine residues. These observations lead to a tentative assignment of E441 to E445, E447 to E449 from the C-terminal tail of α-tubulin (Figure 3c, left panel). Moreover, correlations seen in the 2D ^{13}C-HSQC experiment reflected random-coil chemical shifts of these amino acids. Taken together, these results suggest that the tubulin tails are highly mobile and disordered. We did not observe signals from PTMs of the tubulin C-terminal tails, such as polyglycylation reported before for tubulin from *T. thermophila* that showed higher ^{15}N chemical shift for modified glycine residues at approximately 116 ppm[7a]. We attribute this to the different source tissue, as HeLa tubulin mostly lacks PTMs on tubulin tails[23]. We also observed a correlation at 5.18 ppm of ^{1}H and ~42 ppm of ^{13}C (Figure 3b), which we attribute to carbon atoms in double bonds of co-purified lipids. This correlation is folded along ^{13}C dimension from its actual position ~132 ppm.

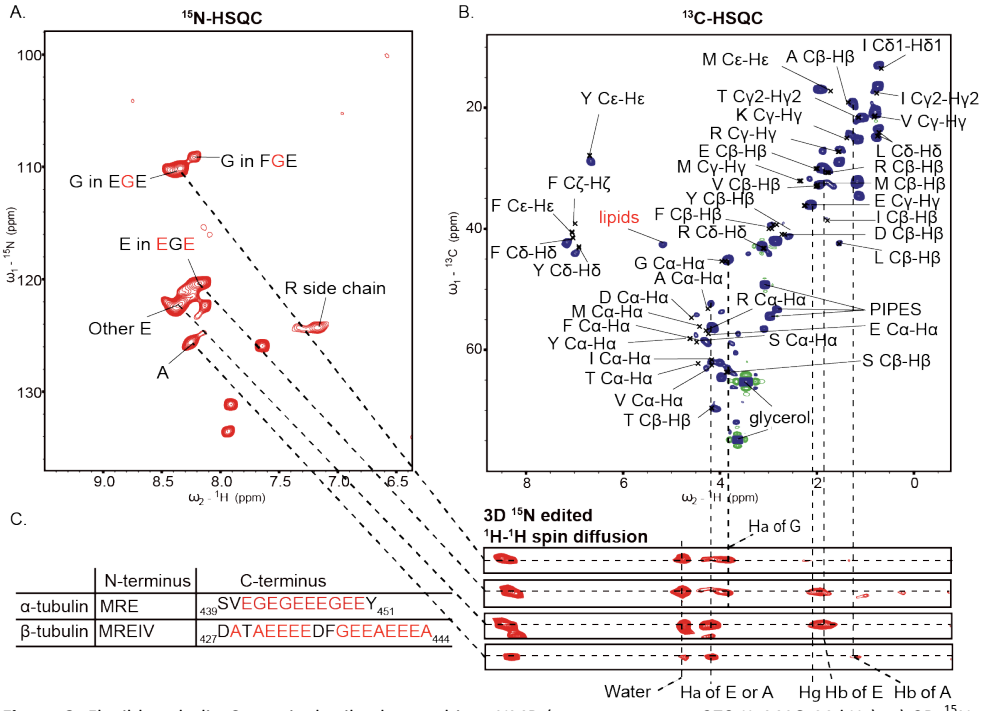

Figure 3. Flexible tubulin C-terminal tails observed in ssNMR (set temperature 270 K, MAS 44 kHz). a) 2D ^{15}N-HSQC of [^{13}C, ^{15}N]-labeled MTs showed the flexible tubulin tails. b) 2D ^{13}C-HSQC of [^{13}C, ^{15}N]-labeled MTs showing the residues present in the tubulin tails. Due to the high flexibility, the signals from the side chains of leucine, lysine, and the buffer compounds were also observed. c) The strips of 3D ^{15}N edited ^{1}H-^{1}H spin diffusion showing the connections between ^{13}C-HSQC and ^{15}N-HSQC (right) and the sequences of N- and C-terminal tails of tubulin (left). The residue number for the tubulin C-terminal tails are indicated and the residue types observed in ^{15}N-HSQC are colored in red.

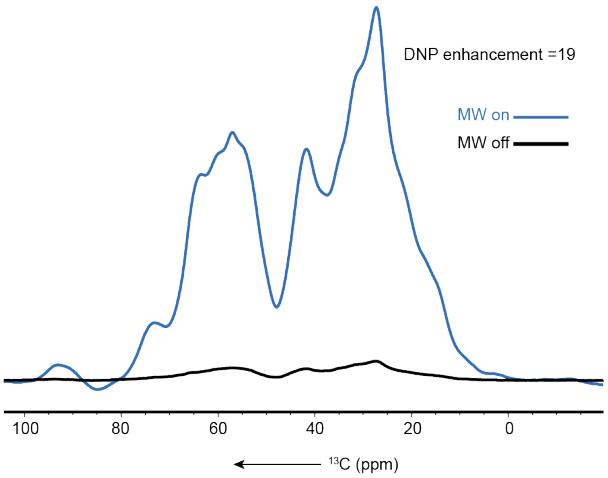

Figure 4. DNP enhancement factor obtained on 800 MHz/527 GHz system. 1D H-^{13}C CP experiments of Taxol-stabilized MTs were measured on an 800 MHz spectrometer with DNP system. The black spectrum was recorded without microwave irradiation (therefore no DNP effect) and the blue spectrum was recorded with microwave irradiation (therefore enhanced by the DNP effect). An enhancement factor of 19 was obtained under the DNP conditions.

We next investigated the use of high-sensitivity DNP experiments, which can greatly enhance the NMR spectral sensitivity by exploiting the higher electron polarization[9], for the study of isotope-labeled MTs. Using AMUPol[15] as the DNP agent, we observed a signal enhancement factor of 19 on the 800 MHz (Figure 4) and ~70 on the 400 MHz DNP instruments (data not shown), respectively. A proton-driven spin diffusion (PDSD) experiment was first recorded on the 800 MHz/527 GHz DNP system and compared with the RFDR experiment (Figure 5). Due to different sample temperature and ^{13}C-^{13}C mixing schemes, we could obtain additional cross peaks corresponding to the C-C correlations that are more than one-bond distance in PDSD. In addition, we observed additional correlations around 59 ppm and 68 ppm that were not predicted based on the cryo-EM structure (Figure 6). Instead they may reflect correlations of polar head groups of the co-purified phospholipids, which would be consistent with the observed lipid signals in the J-based and ^{31}P spectra[32]. The co-purification of phospholipids is not unexpected since previous studies using similar approaches to purify MT from brain also resulted in co-purified phospholipids[34] and tubulin can directly interact with the polar head groups of phospholipids[35]. Further studies will be needed to understand the significance of these observations.

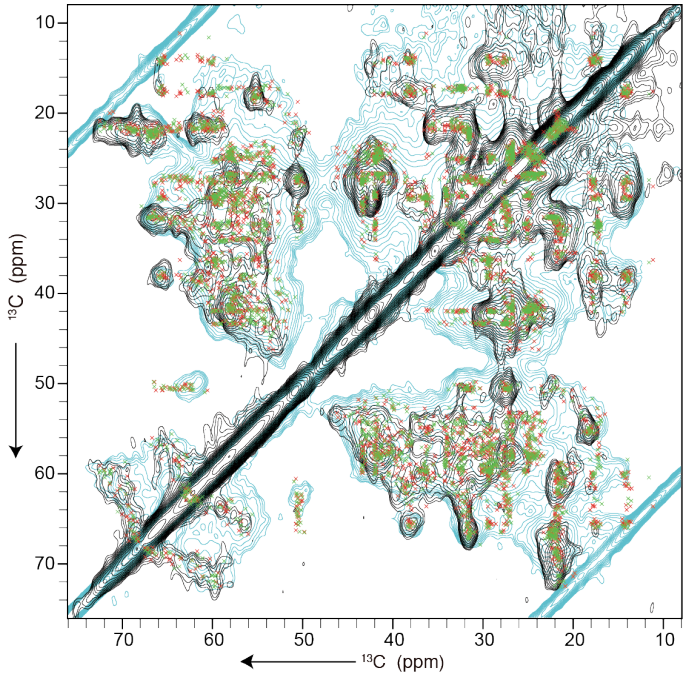

Figure 5. Comparison of ^{13}C-^{13}C PDSD in cyan recorded with DNP (at 800 MHz, 100 K and 10.5 kHz MAS) and RFDR in black (at 700 MHz, 270 K and 44 kHz MAS). Note the blue sidediagonals due to spinning sidebands. The predicted chemical shifts are labeled with same colors as Figure 2a.

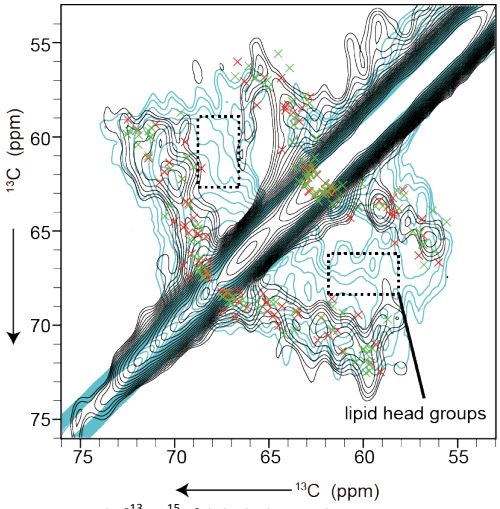

Figure 6. DNP-ssNMR experiments with [^{13}C, ^{15}N]-labeled, Taxol-MTs. Zoom-in on serine and threonine Cα-Cβ regions on the ^{13}C-^{13}C PDSD recorded with DNP at 100 K and MAS of 10.5 kHz (cyan) and RFDR at ambient temperature with MAS of 44 kHz (black). Chemical shift predictions for alanine in random coil structures are highlighted in dash-line boxes. Extra signals that do not match prediction were detected in the DNP experiment (dash-line boxes).

Dynamics of tubulin C-terminal tails was changed upon MAP7-MTBD binding to MTs

Next we investigated whether there are structural or dynamical changes of MTs upon interacting with MAP7-MTBD (see Chapter 4) using ssNMR on labeled MTs. For this purpose, we prepared a sample of unlabeled MAP7-MTBD in complex with [^{13}C, ^{15}N]-labeled MTs. To probe changes related to the dynamic MT tails, we recorded an ^{15}N-HSQC (Figure 7a, black) spectrum and compared our results to the free case (Figure 7a, red, see also Figure 3a). Interestingly, we observed no major chemical-shift changes but an overall decrease in signal intensity in this J-based experiment when MAP7-MTBD binds to MTs. This observation suggests that the dynamics of the flexible tubulin C-terminal tails were affected by the binding of MAP7 MTBD. Notably, glycine and alanine residues are distinct in the C-terminal tails of α- and β-tubulin respectively (Figure 3c, left panel). Therefore the observed decrease in signal intensity for both glycine and alanine residues indicates that both tubulin C-terminal tails may be involved in the interaction with MAP7-MTBD or become rigidified upon the formation of MAP7-MTBD/MT complex (Figure 7b). Further investigations using

ssNMR are planned to further characterize the interaction between MAP7-MTBD and MTs.

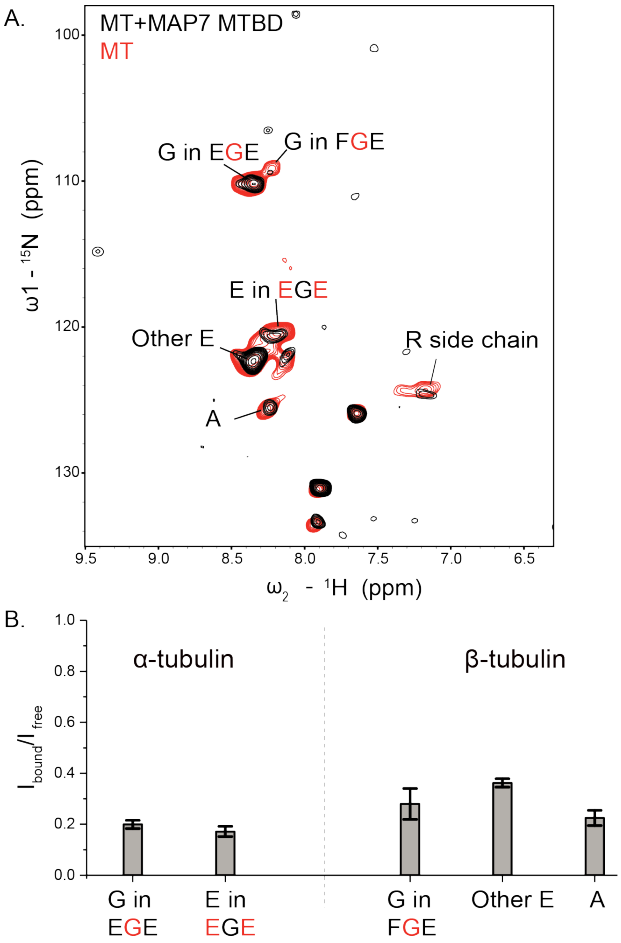

Figure 7. Dynamics of tubulin C-terminal tails are affected when MAP7 MTBD binds to MTs. a) Comparison of ^{15}N-HSQC spectra obtained from [^{13}C, ^{15}N]-labeled MTs (red) and unlabeled MAP7 MTBD in complex with [^{13}C, ^{15}N]-labeled MTs (black). b) Signal intensity ratios of resolved peaks in ^{15}N-HSQC between MAP7 MTBD bound MTs and free MTs. The error bars were calculated based on the s/n of each peak on the two spectra.

Discussion

We have shown NMR spectra recoded on [^{13}C, ^{15}N]-labeled MTs. To our knowledge, it is the first direct NMR study on mammalian MTs. The MTs were polymerized from tubulin purified from HeLa S3 cells in a functional form, as

confirmed by *in vitro* MT dynamics assays. Our biologically active preparations also exhibited narrow ^{31}P NMR signals allowing us to readily probe GDP and GTP that are critically involved in the MT polymerization cycle. Moreover, combining dipolar- and scalar-based ssNMR methods, we could probe the folded, rigid core of tubulin subunits in MTs and reveal disordered and flexible tubulin tails, which are invisible in all available high-resolution structures and are believed to be involved in MAP binding[36]. While earlier solution-state NMR studies on isotope-labeled tubulin from *T. thermophila* reported poly-glycine signals from the C-terminal tails[7a], our results confirm earlier work suggesting that PTM levels in the C-terminal tails of HeLa tubulin are low[23]. Using our novel approach, we could probe the direct interaction of MAP7-MTBD with tubulin C-terminal tails on MTs. We observed a modulation of the tail dynamics changes of MTs upon binding to MAP7-MTBD, which suggests that the tubulin C-terminal tails are involved in the interaction with MAP7-MTBD. Further experiments, including the study of MAP7-MTBD binding to subtilisin-treated MTs[8c] (which tubulin C-terminal tails are cleaved) will likely further advance our understanding for this interaction.

Taken together, our results pave the way for in-depth studies of structure and dynamics of MTs, possibly during different stages of the polymerization cycle, as well as of their interactions with MAPs and other cellular players at atomic level by ssNMR. In such experiments, advanced labeling[10b] in combination of DNP with ^{1}H ssNMR and ultra-fast MAS will further expand the potential of ssNMR to provide residue-specific insight into the role of the MTs in numerous biological processes in eukaryotic cells.

References:

[1] A. Desai, T. J. Mitchison, *Annual Review of Cell and Developmental Biology* **1997**, *13*, 83-117.

[2] a) A. Akhmanova, M. O. Steinmetz, *Nature Reviews Molecular Cell Biology* **2008**, *9*, 309-322; b) A. Akhmanova, Casper C. Hoogenraad, *Current Biology* **2015**, *25*, R162-R171.

[3] S. Gadadhar, S. Bodakuntla, K. Natarajan, C. Janke, *Journal of Cell Science* **2017**, *130*, 1347-1353.

[4] a) G. M. Alushin, G. C. Lander, E. H. Kellogg, R. Zhang, D. Baker, E. Nogales, *Cell* **2014**, *157*, 1117-1129; b) E. Nogales, R. Zhang, *Current Opinion in Structural Biology* **2016**, *37*, 90-96.

[5] E. H. Kellogg, N. M. A. Hejab, S. Poepsel, K. H. Downing, F. DiMaio, E. Nogales, *Science* **2018**, *360*, 1242-1246.

[6] H. Aldaz, L. M. Rice, T. Stearns, D. A. Agard, *Nature* **2005**, *435*, 523-527.

[7] a) K. P. Wall, M. Pagratis, G. Armstrong, J. L. Balsbaugh, E. Verbeke, C. G. Pearson, L. E. Hough, *ACS Chemical Biology* **2016**, *11*, 2981-2990; b) H. Kadavath, Y. Cabrales Fontela, M. Jaremko, Ł. Jaremko, K. Overkamp, J. Biernat, E. Mandelkow, M. Zweckstetter, *Angewandte Chemie International Edition* **2018**, *57*, 3246-3250; c) C. Kesten, A. Wallmann, R. Schneider, H. E. McFarlane, A. Diehl, G. A. Khan, B.-J. van Rossum, E. R. Lampugnani, W. G. Szymanski, N. Cremer, P. Schmieder, K. L. Ford, F. Seiter, J. L. Heazlewood, C. Sanchez-Rodriguez, H. Oschkinat, S. Persson, *Nature Communications* **2019**, *10*, 857.

[8] a) A. Kumar, H. Heise, M. J. J. Blommers, P. Krastel, E. Schmitt, F. Petersen, S. Jeganathan, E.-M. Mandelkow, T. Carlomagno, C. Griesinger, M. Baldus, *Angewandte Chemie International Edition* **2010**, *49*, 7504-7507; b) S. Yan, C. Guo, G. Hou, H. Zhang, X. Lu, J. C. Williams, T. Polenova, *Proceedings of the National Academy of Sciences* **2015**, *112*, 14611-14616; c) J. Atherton, K. Jiang, M. M. Stangier, Y. Luo, S. Hua, K. Houben, J. J. E. Van Hooff, A. P. Joseph, G. Scarabelli, B. J. Grant, A. J. Roberts, M. Topf, M. O. Steinmetz, M. Baldus, C. A. Moores, A. Akhmanova, *Nature Structural and Molecular Biology* **2017**, *24*, 931-943.

[9] Q. Z. Ni, E. Daviso, T. V. Can, E. Markhasin, S. K. Jawla, T. M. Swager, R. J. Temkin, J. Herzfeld, R. G. Griffin, *Accounts of Chemical Research* **2013**, *46*, 1933-1941.

[10] a) M. Kaplan, A. Cukkemane, G. C. P. van Zundert, S. Narasimhan, M. Daniëls, D. Mance, G. Waksman, A. M. J. J. Bonvin, R. Fronzes, G. E. Folkers, M. Baldus, *Nature Methods* **2015**, *12*, 649-652; b) M. Kaplan, S. Narasimhan, C. de Heus, D. Mance, S. van Doorn, K. Houben, D. Popov-Čeleketić, R. Damman, E. A. Katrukha, P. Jain, W. J. C. Geerts, A. J. R. Heck,

G. E. Folkers, L. C. Kapitein, S. Lemeer, P. M. P. van Bergen en Henegouwen, M. Baldus, *Cell* **2016**, *167*, 1241-1251.e1211.

[11] S. Xiang, U. B. le Paige, V. Horn, K. Houben, M. Baldus, H. van Ingen, *Angewandte Chemie International Edition* **2018**, *57*, 4571-4575.

[12] a) M. B. Yaffe, G. W. Farr, D. Miklos, A. L. Horwich, M. L. Sternlicht, H. Sternlicht, *Nature* **1992**, *358*, 245-248; b) Y. Gao, I. E. Vainberg, R. L. Chow, N. J. Cowan, *Molecular and Cellular Biology* **1993**, *13*, 2478-2485.

[13] a) A. Fourest-Lieuvin, *Protein Expression and Purification* **2006**, *45*, 183-190; b) N. Kaul, V. Soppina, Kristen J. Verhey, *Biophysical Journal* **2014**, *106*, 2636-2643.

[14] a) Jeffrey J. Nirschl, Maria M. Magiera, Jacob E. Lazarus, C. Janke, Erika L. F. Holzbaur, *Cell Reports* **2016**, *14*, 2637-2652; b) P. Guedes-Dias, J. J. Nirschl, N. Abreu, M. K. Tokito, C. Janke, M. M. Magiera, E. L. F. Holzbaur, *Current Biology* **2019**.

[15] C. Sauvée, M. Rosay, G. Casano, F. Aussenac, R. T. Weber, O. Ouari, P. Tordo, *Angewandte Chemie International Edition* **2013**, *52*, 10858-10861.

[16] a) A. E. Bennett, J. H. Ok, R. G. Griffin, S. Vega, *J. Chem. Phys.* **1992**, *96*, 8624-8627; b) A. E. Bennett, C. M. Rienstra, J. M. Griffiths, W. G. Zhen, P. T. Lansbury, R. G. Griffin, *J. Chem. Phys.* **1998**, *108*, 9463-9479.

[17] T. M. Alam, G. P. Holland, *Journal of Magnetic Resonance* **2006**, *180*, 210-221.

[18] M. Weingarth, J. Trebosc, J. P. Amoureux, G. Bodenhausen, P. Tekely, *Solid State Nucl. Magn. Reson.* **2011**, *40*, 21-26.

[19] B. M. Fung, A. K. Khitrin, K. Ermolaev, *Journal of Magnetic Resonance* **2000**, *142*, 97-101.

[20] a) N. Bloembergen, *Physica* **1949**, *15*, 386-426; b) N. M. Szeverenyi, M. J. Sullivan, G. E. Maciel, *Journal of Magnetic Resonance (1969)* **1982**, *47*, 462-475.

[21] a) M. Hohwy, C. M. Rienstra, C. P. Jaroniec, R. G. Griffin, *J. Chem. Phys.* **1999**, *110*, 7983-7992; b) M. Hong, *Journal of Magnetic Resonance* **1999**, *136*, 86-91.

[22] A. Davis, S. Martinez, D. Nelson, K. Middleton, *Methods in Cell Biology* **2010**, *95*, 331-351.

[23] M. Barisic, R. Silva e Sousa, S. K. Tripathy, M. M. Magiera, A. V. Zaytsev, A. L. Pereira, C. Janke, E. L. Grishchuk, H. Maiato, *Science* **2015**, *348*, 799.

[24] B. A. Weaver, W. Bement, *Molecular Biology of the Cell* **2014**, *25*, 2677-2681.

[25] P. J. Hooikaas, M. Martin, T. Mühlethaler, G.-J. Kuijntjes, C. A. E. Peeters, E. A. Katrukha, L. Ferrari, R. Stucchi, D. G. F. Verhagen, W. E. van Riel, I. Grigoriev, A. F. M. Altelaar, C. C. Hoogenraad, S. G. D. Rüdiger, M. O.

Steinmetz, L. C. Kapitein, A. Akhmanova, *The Journal of Cell Biology* **2019**, jcb.201808065.

[26] B. Han, Y. Liu, S. W. Ginzinger, D. S. Wishart, *Journal of Biomolecular NMR* **2011**, *50*, 43-57.

[27] S. Narasimhan, D. Mance, C. Pinto, M. Weingarth, A. M. J. J. Bonvin, M. Baldus, in *Protein NMR: Methods and Protocols* (Ed.: R. Ghose), Springer New York, New York, NY, **2018**, pp. 111-132.

[28] M. Menéndez, G. Rivas, J. F. Díaz, J. M. Andreu, *The Journal of biological chemistry* **1998**, *273*, 167-176.

[29] L. G. Hyang, O. S. Young, Y. K. Joo, F. Taslima, C. Meeyeon, P. Younkee, *Magnetic Resonance in Chemistry* **2015**, *53*, 330-336.

[30] M. Spoerner, M. Karl, P. Lopes, M. Hoering, K. Loeffel, A. Nuehs, J. Adelsberger, W. Kremer, H. R. Kalbitzer, *Journal of Biomolecular NMR* **2017**, *67*, 1-13.

[31] H. Kaur, A. Lakatos-Karoly, R. Vogel, A. Nöll, R. Tampé, C. Glaubitz, *Nature Communications* **2016**, *7*, 13864.

[32] J. M. Boettcher, R. L. Davis-Harrison, M. C. Clay, A. J. Nieuwkoop, Y. Z. Ohkubo, E. Tajkhorshid, J. H. Morrissey, C. M. Rienstra, *Biochemistry* **2011**, *50*, 2264-2273.

[33] T. Blom, P. Somerharju, E. Ikonen, *Cold Spring Harbor perspectives in biology* **2011**, *3*, a004713-a004713.

[34] A. J. Hargreaves, W. G. McLean, *International Journal of Biochemistry* **1988**, *20*, 1133-1138.

[35] D. P. Hoogerheide, S. Y. Noskov, D. Jacobs, L. Bergdoll, V. Silin, D. L. Worcester, J. Abramson, H. Nanda, T. K. Rostovtseva, S. M. Bezrukov, *Proceedings of the National Academy of Sciences* **2017**, *114*, E3622-E3631.

[36] J. Lefèvre, K. G. Chernov, V. Joshi, S. Delga, F. Toma, D. Pastré, P. A. Curmi, P. Savarin, *Journal of Biological Chemistry* **2011**, *286*, 3065-3078.

CHAPTER 6

6

Discussion and future perspectives

In recent years, ssNMR has made significant progress to study complex biomolecules at atomic resolution, making it a powerful addition to the current arsenal of structural biology methods. Compared to solution-state NMR, which requires fast tumbling of molecules and is commonly used to study smaller proteins, ssNMR can overcome the size limitation and allows to study more complicated biomolecule complexes. Over the past years ssNMR has, for example, been used to study membrane proteins and membrane protein complexes in synthetic lipid bilayers, and even recently in native membranes that is more close to their native environments[1]. More recently, the application of ssNMR extended to more protein complexes, for example, the cytoskeletons and their interactions with the associated proteins or binding compounds[2]. As an essential component of the eukaryotic cytoskeletons, microtubules (MT) have been intensively studied in order to understand the mechanisms of their dynamic instability and their interactions with the microtubule-associated proteins (MAPs), especially at the atomic level. Cryo-EM and X-ray crystallography studies have shown structural details of microtubule itself or the interactions with the dynamic regulators[3]. ssNMR, on the other hand, can provide highly complementary information for such studies as it can provide residue-specific and atomic-resolution information but also probes the local dynamics and their changes of MTs or MAPs between the unbound- and bound-state. Therefore, we set out to investigate different binding domains from MAPs in complex with MTs and for the first time developed a protocol to obtain isotope-labeled, purified MTs to directly carry out ssNMR study on MTs. The latter preparations were analyzed using advanced ssNMR techniques, including ^{1}H detected ssNMR and DNP. Our data have shown the power of ssNMR in obtaining high-resolution and residue-specific information of protein domains that bind MTs to identify the binding interface between MAPs and MTs, such as the results presented in Chapters 2, 3 and 4. In addition, our data showed the advantages of NMR to obtain atomic level information of the dynamic regions of MTs (Chapter 5), which were not seen by cryo-EM and how these regions interact with MAPs such as MAP7.

While the study of uniformly labeled wild-type CKK domain in complex with MTs allowed us to identify the binding region of CKK domain to MTs, the analysis was complicated by the comparatively low spectral resolution and sensitivity (Chapter 2). As seen in the context of other ssNMR studies of complex

biomolecules[4] we attribute the lower spectral resolution and sensitivity to the sample heterogeneity, which resulted from the minus-end selectivity of CKK domain binding to MTs that leads to protofilament skew of MTs upon binding the whole MT lattice. This conclusion was further confirmed by comparing the spectra of the CAMSAP1 CKK N1492A mutant in complex with MTs, which has better resolution and sensitivity since it reduces minus-end selectivity and protofilament skew, leading to a more homogeneous sample state. The difference in spectral resolution also again confirmed that NMR is highly sensitive to the chemical environment of each atom in our preparations. This gain in resolution seen for the mutant allowed us to also carry out ^{1}H detection ssNMR experiments and obtain resonance assignments for the CKK mutant in complex with MTs using solution-state NMR data of the free protein as a reference. These assignments allowed us to better identify the binding interface of CKK with MTs. Remarkably, this analysis also revealed that no secondary structural alternations of CKK occur upon binding to MTs as the Cα chemical shifts remained largely constant when comparing free- and bound-state CKK. Instead, the significant chemical-shift perturbations were observed on the amide protons and the ^{15}N atoms from the residues that are close to MTs, demonstrating their considerable use for probing the chemical environment for these residues in relation to the free-state CKK, which is in agreement with our cryo-EM results. In addition, NMR has the advantage to probe protein dynamics, including slow chemical exchange of protein. Under solution-state NMR conditions, we determined the CPMG and CEST dynamics profiles of CKK domains. These studies confirmed our ssNMR results and strongly suggest that these CKK domains are rigid and undergo no conformational exchange upon binding. Therefore, it is likely that MTs adopt protofilament skew to provide the preferred binding site for CKK domains. This observation also reflects that MTs are flexible polymers and the MT lattice plasticity is important for MAPs binding.

On the other hand, members of the MAP7 protein family have been discovered to interact with MTs and recruit kinesin-1 to the MT lattice, as well as compete with MAP Tau for MT binding[5]. Therefore, it is important to investigate how MAP7 proteins associate with MT and kinesin binding. Here we focused on the N-terminal MT-binding (MTBD) domain of MAP7. We first characterized the secondary structural elements by using solution-state NMR. These studies showed that the MAP7 MTBD is an alpha-helical protein fragment with an

unstructured region. ssNMR data obtained on the [^{13}C, ^{15}N]-labeled MAP7 MTBD-MT complex showed that MAP7 MTBD is highly helical upon binding to MTs. The C-terminus of MAP7 MTBD is unstructured and we found that it becomes at least partially rigidified when interacting with MTs. Interestingly, the significant chemical-shift change of T146 Cα upon binding to MTs might be an indication that MAP7 MTBD also undergoes conformational changes when interacting with MTs. Further studies are required to discover the whole binding region of MAP7 MTBD and the binding mode with MTs. However, due to the biased amino acid composition and limited signal dispersion, it is challenging to directly analyze the spectra recorded on uniformly labeled MAP7 MTBD. To overcome this problem, different selective labeling methods would be useful. One potential labeling strategy is segmental isotope labeling, which allows isotope labeling for certain regions of the proteins and reduces signal overlap[6]. Furthermore, the application of segmental labeling with different selective labeling schemes for certain amino acids should significantly improve the prospects for assigning MAP7 MTBD both in the free- and bound-state, thereby allowing us to better identify the binding interface with MTs.

Up to now, it has remained difficult to obtain milligrams amount of purify tubulin (or MTs) from mammalian cells, especially in a homogenous and isotope-labeled form. This limitation largely precludes ssNMR studies on MTs. In chapter 5, we have presented an approach that builds on a previous protocol for tubulin purification and allowed us to obtain milligrams of functional, uniformly labeled and homogeneous MTs from HeLa cells for ssNMR study. Our data on [^{13}C, ^{15}N]-labeled MTs suggested that we could not only employ ssNMR to probe the rigid tubulin bodies on MTs, but also the flexible tubulin C-terminal tails that are not seen in X-ray crystallography and cryo-EM. In addition, the tubulin C-terminal tails undergo a variety of post-translational modifications (PTMs) in cells. Pervious work suggests that PTMs of tubulin are associated in regulation of MT dynamics and human disorders, therefore it is important to understand how different modifying enzymes interact and modify the tubulin tails. With our results, ssNMR now carries the potential to resolve these questions. Since we have managed to prepare isotope-labeled MTs for ssNMR, we can now extend studies on how MTs interact with different MAPs and directly probe at the binding sites on MTs and how the tubulin tails interact with MAPs and change their dynamics, as many MAPs interactions with MTs involve the tubulin tails[7].

Moreover, with the help of DNP to enhance the spectral sensitivity, we could potentially perform NHHC correlation experiment[8] to probe the magnetization transfer from ^{15}N-labeled MTs (or MAPs, for example MAP7 MTBD) to ^{13}C-labeled MAPs (or MTs). Such experiments allow us to directly detect signals stemming from the residues of MTs and MAPs that are close in space each other, thereby providing direct information about the contact regions of MTs and MAPs at atomic scale.

Although this thesis contains the first demonstration of producing MTs for direct NMR studies, amount of the yielded protein was still limited and only enough for studies in the 1.3 mm ssNMR MAS rotors. Yet, even with this rather small amount of sample we managed to characterize the structure and dynamics of MTs with fast MAS experiments. Using the newest generation of 0.7 mm MAS rotors, which presently are the smallest commercially available NMR will further reduce the amount of sample needed for ssNMR experiments. Likewise, these rotors will enable ultra-fast MAS to 100 kHz which will further improve the spectral resolution. As a result, protein deuteration, which is still challenging for proteins produced in mammalian cells (which are sensitive to deuterium oxide) may not be required anymore. Instead, the use of ^{1}H detection and tailored 3D experiments on [^{13}C, ^{15}N]-labeled MTs without deuteration may be sufficient to study such complexes by NMR. Finally, the availability of 1.2 GHz NMR magnets in the near future will allow for measurements at higher magnetic field and thereby further improve the spectral resolution and sensitivity. Taken together, these instrumental advancements will offer unprecedented options to conduct ssNMR studies on MTs and their interactions with MAPs at highest spectral and temporal resolution.

Lastly, there has been significant progress in the field of cellular structural biology to study biomolecules and complexes at the atomic level in their native environments. In recent year, innovative NMR concepts has been developed to study protein structures and functions in bacteria and eukaryotic cells[9]. Such methods provide additional information about how proteins of interest change structure and dynamics in a cellular environment and in response to external stimuli and interaction partners. In the future, in-cell NMR might be employed in combination with high-sensitivity ssNMR approaches discussed above to study complex and time-dependent MT interactions within a functional cellular

environment, including the time-resolved competition of MAP7 and Tau binding to MTs to control distinct classes of protein motors.

References:

[1] L. A. Baker, M. Baldus, *Current Opinion in Structural Biology* **2014**, *27*, 48-55.

[2] a) A. Kumar, H. Heise, M. J. J. Blommers, P. Krastel, E. Schmitt, F. Petersen, S. Jeganathan, E.-M. Mandelkow, T. Carlomagno, C. Griesinger, M. Baldus, *Angewandte Chemie International Edition* **2010**, *49*, 7504-7507; b) S. Yan, C. Guo, G. Hou, H. Zhang, X. Lu, J. C. Williams, T. Polenova, *Proceedings of the National Academy of Sciences* **2015**, *112*, 14611; c) J. Atherton, K. Jiang, M. M. Stangier, Y. Luo, S. Hua, K. Houben, J. J. E. van Hooff, A.-P. Joseph, G. Scarabelli, B. J. Grant, A. J. Roberts, M. Topf, M. O. Steinmetz, M. Baldus, C. A. Moores, A. Akhmanova, *Nature Structural &Amp; Molecular Biology* **2017**, *24*, 931; d) J. Yehl, E. Kudryashova, E. Reisler, D. Kudryashov, T. Polenova, *Scientific Reports* **2017**, *7*, 44506.

[3] a) E. Nogales, E. H. Kellogg, *Current Opinion in Structural Biology* **2017**, *46*, 65-70; b) M. O. Steinmetz, A. E. Prota, *Trends in Cell Biology* **2018**, *28*, 776-792.

[4] M. Renault, A. Cukkemane, M. Baldus, *Angewandte Chemie-International Edition* **2010**, *49*, 8346-8357.

[5] B. Y. Monroy, D. L. Sawyer, B. E. Ackermann, M. M. Borden, T. C. Tan, K. M. Ori-McKenney, *Nature Communications* **2018**, *9*, 1487.

[6] a) D. Liu, R. Xu, D. Cowburn, in *Methods in Enzymology, Vol. 462* (Eds.: T. W. Muir, J. N. Abelson), Academic Press, **2009**, pp. 151-175; b) T. Schubeis, M. Nagaraj, C. Ritter, in *Split Inteins: Methods and Protocols* (Ed.: H. D. Mootz), Springer New York, New York, NY, **2017**, pp. 147-160.

[7] J. Lefèvre, K. G. Chernov, V. Joshi, S. Delga, F. Toma, D. Pastré, P. A. Curmi, P. Savarin, *The Journal of biological chemistry* **2011**, *286*, 3065-3078.

[8] A. Lange, S. Luca, M. Baldus, *Journal of the American Chemical Society* **2002**, *124*, 9704-9705.

[9] a) E. Luchinat, L. Banci, *IUCrJ* **2017**, *4*, 108-118; b) D. I. Freedberg, P. Selenko, *Annual Review of Biophysics* **2014**, *43*, 171-192.

APPENDICES

A

Appendices

Summary

The dynamic instability of microtubules (MT) is an essential feature in eukaryotic cells and related to basic cellular processes such as intracellular transport, cell division, migration, or polarization. Microtubule-associated proteins (MAPs) are critically involved in such MT dynamics by binding to MTs and reshaping the molecular and structural organization. Although the structure and dynamics of MTs, as well as the MT interactomic network have been intensively studied over the past decades, a detailed understanding on how different MAPs interact with MTs and how they jointly contribute to MT functioning in the cell remains largely elusive. For this reason, atomic level knowledge about the structural organization of MT-MAPs complexes is indispensable for understanding the mechanistic details of the MT interactome and its dynamic features. In this thesis, my goal was to study the binding modes of specific MAPs to MTs, and on the other hand investigate structural and dynamical alternations of MTs that occur upon MAP binding. The studies presented in this thesis relied on the advancements in solid-state NMR (ssNMR) spectroscopy to study large protein complexes, including the use of ^{1}H-detected ssNMR and dynamic nuclear polarization (DNP).

In **Chapter 2** we investigated the binding mode of the CKK domain from mammalian CAMSAP proteins to MTs. By analyzing the solution- and solid-state NMR data on free- and MT-bound CKK, respectively, and combining these findings with other structural biology techniques including cryo-EM and x-ray crystallography, the high-resolution structure of CKK domain in complex with MTs was obtained. These structural findings led to a better understanding of how CAMSAP proteins protect the noncentrosomal MT minus ends from depolymerization.

In **Chapter 3** we further studied the structural determinants of CKK domain binding to MTs. We employed ^{1}H ssNMR on the N1492A mutant of CAMSAP1 CKK that showed reduced minus-end selectivity and the ability to generate protofilament skew of MTs. The ssNMR data obtained on this CKK mutant was characterized by improved spectral sensitivity and resolution. To shed light on the MT minus-end recognition of CAMSAPs, we carried out CPMG and CEST experiments using solution-state NMR to probe millisecond time-scale chemical exchange of the mammalian CKK domains. Our results showed that CKK

domains investigated are remarkably rigid and undergo no slow conformational exchange in solution, thus supporting the idea that CKK rigidity is critical to induce protofilament skew of MTs. On the other hand, our data reveal that MTs are flexible and able to undergo conformational changes. The plasticity of MTs may be an important feature for MAPs-MT binding and recognition.

We then studied the MT-binding domain (MTBD) of MAP7 in **Chapter 4**. The structural elements of MAP7 were first investigated using solution-state NMR and the MT-bound MAP7 MTBD was then examined by solid-state NMR. By comparing the chemical-shift values of free- and bound-state MAP7 MTBD, we obtained preliminary results showing that MAP7 MTBD adopts a largely α-helical fold and with unstructured termini. The binding mode of MAP7 MTBD is still under investigation and will be potentially be revealed by integrating our NMR results with findings obtained using x-ray crystallography and cryo-EM.

Direct ssNMR studies on MT studies so far were precluded due to the absence of appropriate methods yielding sufficient amounts of isotope-labeled MTs. In **Chapter 5**, we developed and applied a protocol for MT preparation for direct ssNMR studies. By using fast MAS, ^{1}H ssNMR and DNP techniques, we were able to probe the rigid folded parts of MTs and the flexible tubulin C-terminal tails. In addition, we could detect the dynamical changes of MTs upon interaction with MAPs. Our data showed that the flexibility of both tubulin C-terminal tails are affected upon binding to MAP7 MTBD, leading to a more stable state of the C-termini of α- and β-tubulin subunits. In a further stage, this study could be continued by employing DNP to directly study the binding mode of MAP7 MTBD in complex with MTs to further identify other regions that are involved in this interaction.

Taken together, the work presented in this thesis paves the way for in-depth studies of MT structures and dynamics, as well as their interactions with proteins or small molecules. Using ssNMR spectroscopy, atomic-level information can be obtained and the approaches described here can complement other structural or cell biology techniques.

Samenvatting

De dynamische instabiliteit van microtubuli (MTs) is een essentieel kenmerk van eukaryote cellen en gerelateerd aan basale cellulaire processen zoals intracellulair transport, celdeling, migratie of polarisatie. Microtubulus-geassocieerde eiwitten (MAPs) zijn kritisch betrokken bij dergelijke MT-dynamica door binding aan MTs en het hervormen van de moleculaire en structurele organisatie. Hoewel de structuur en dynamiek van MTs, evenals het MT-interactomisch netwerk de afgelopen decennia intensief zijn bestudeerd, blijft een gedetailleerd inzicht in hoe MAPs en MTs interacteren en hoe ze gezamenlijk bijdragen aan het functioneren van MT in de cel grotendeels ongrijpbaar. Om deze reden is kennis op atomair niveau over de structurele organisatie van MT-MAPs-complexen cruciaal voor het begrijpen van de mechanistische details van het MT-interactoom en zijn dynamische kenmerken. In dit proefschrift was het mijn doel om de bindingswijzen van specifieke MAPs aan MTs te bestuderen en aan de andere kant ook structurele en dynamische veranderingen van MTs te onderzoeken die optreden na MAP-binding. De studies gepresenteerd in dit proefschrift waren gebaseerd op de ontwikkelingen in vaste-fase NMR (ssNMR) spectroscopie om grote eiwitcomplexen te bestuderen, waaronder het gebruik van ^{1}H-gedetecteerde ssNMR en dynamische nucleaire polarisatie (DNP).

In **Hoofdstuk 2** hebben we de bindingsmodus van het CKK domein van CAMSAP-eiwitten van zoogdieren aan MTs onderzocht. Op basis van NMR gegevens van vrij- en gebonden CKK, gerealiseerd met respectievelijk CKK in oplossing en in de vaste stof fase, en in combinatie met andere structuur biologische technieken zoals cryo-EM en röntgenkristallografie, was de structuur met hoge resolutie verkrgen van het CKK domein in complex met MTs. Deze structurele bevindingen leidden tot een beter begrip van hoe CAMSAP eiwitten de niet-centrosomale MT-minus-uiteinden beschermen tegen depolymerisatie.

In **Hoofdstuk 3** hebben we de structurele determinanties van CKK domeinbinding aan MTs verder bestudeerd. We gebruikten ^{1}H ssNMR op de N1492A mutant van CAMSAP1 CKK die verminderde minusuiteinde-selectiviteit vertoonde en het vermogen om protofilament van MTs scheef te trekken. De ssNMR gegevens verkregen van deze CKK mutant werd gekenmerkt door een verbeterde spectrale gevoeligheid en resolutie. Om licht te werpen op de MT-

minus-einde-herkenning van CAMSAP's, hebben we CPMG- en CEST-experimenten uitgevoerd met behulp van vloeibare fase-NMR om op een milliseconde tijdschaal chemische uitwisseling van de zoogdier-CKK-domeinen te onderzoeken. Onze resultaten toonden aan dat de onderzochte CKK-domeinen opmerkelijk rigide zijn en geen trage conformationele uitwisseling in oplossing ondergaan, wat het idee ondersteunt dat CKK-rigiditeit van cruciaal belang is om het scheef trekken van MTs protofilament te induceren. Aan de andere kant onthullen onze gegevens dat MTs flexibel zijn en conformationele veranderingen kunnen ondergaan. De plasticiteit van MTs kan een belangrijke functie zijn voor binding en herkenning van MAPs-MT.

Vervolgens bestudeerden we het MT-bindingsdomein (MTBD) van MAP7 in **Hoofdstuk 4**. De structurele elementen van MAP7 werden eerst onderzocht met NMR in de vloeibare fase en vervolgens werd de MT-gebonden MAP7 MTBD onderzocht met ssNMR. Door de waarden van de chemische verschuiving van MAP7 MTBD in de vrije- en gebonden toestand te vergelijken, hebben we voorlopige resultaten verkregen die aantonen dat MAP7 MTBD een grotendeels α-helicale vouwing heeft met ongestructureerde termini. De bindingswijze van MAP7 MTBD wordt nog onderzocht en zal mogelijk worden onthuld door onze NMR-resultaten te integreren met bevindingen die zijn verkregen met behulp van röntgenkristallografie en cryo-EM.

Gerichte ssNMR studies van MTs werden tot dusverre uitgesloten vanwege de het ontbreken van geschikte methoden die voldoende hoeveelheden met isotoop-gemerkte MTs opleveren. In **Hoofdstuk 5** hebben we een protocol voor MT monsters voor gerichte ssNMR studies ontwikkeld en toegepast. Door hoge snelheid MAS, ^{1}H ssNMR en DNP technieken te gebruiken, konden we de rigide gevouwen delen van MTs en de flexibele C-terminale staarten van tubuline onderzoeken. Bovendien konden we de dynamische veranderingen van MTs detecteren na binden van MAPs. Onze gegevens toonden aan dat de flexibiliteit van beide tubuline C-terminale staarten wordt beïnvloed door binding aan MAP7 MTBD, wat leidt tot een stabielere toestand van de C-terminale staarten van α- en β-tubulinesubeenheden. In een volgende fase zou dit onderzoek kunnen worden voortgezet door DNP te gebruiken om de bindingsmodus van MAP7 MTBD in complex met MTs rechtstreeks te bestuderen om andere regio's die betrokken zijn bij deze interactie verder te identificeren.

Samenvattend, maakt het in dit proefschrift gepresenteerde werk de weg vrij voor diepgaande studies van MT structuren en dynamica, evenals hun interacties met eiwitten en kleine moleculen. Met behulp van ssNMR spectroscopie kan atoomniveau informatie worden verkregen en de hier beschreven benaderingen kunnen andere structurele of celbiologische technieken aanvullen.

Acknowledgements

First of all, I would like to express my gratitude to my supervisor, Prof. Marc Baldus for offering me the opportunity to join the group to do my PhD and work on the challenging and nice research projects, also for his enthusiasm in science and the work discussions I was involved in for the past four years of my PhD.

Besides, I would like to thank Gert Folkers and Mark Daniëls for the nice discussions and helpful suggestions in the wet lab during my master and PhD time.

I would like to thank Prof. Anna Akhmanova, Dr. Carsten Janke and Prof. Friedrich Förster for the nice discussions about the microtubule projects I was involved in. Also I am grateful to Dr. Kai Jiang and Peter Jan Hooikaas for all these fruitful collaborations.

Klaartje, it was nice to work with you at the beginning of my PhD and I appreciate your help and teaching me setting up solid-state and solution-state NMR experiments. Deni, Markus and Shengqi, thank you for the nice time we spent in front of the NMR machines and for improving my NMR knowledge.

I would like to thank Hugo for the nice discussions and data analysis for the collaborative project with the group of Prof. Bert Poolman.

Cecilia, it was a pleasure to have you as officemate during my master internship and the first two years of my PhD. We had many fun discussions and thank you for your help. Sid and Reinier, it was very nice that we started at the same time from our master study and our PhD. Thank you both for helpful work discussions and pleasant conversations throughout these years. Alessandra, Miranda, João and all other people from the NMR department, thanks for being nice colleagues and all your help. Agnes, I wish you all the best with taking over the microtubule projects, I am sure you will bring the projects to a higher level.

Finally, I would express my unlimited gratitude to my family. I would thank my parents, as well as my aunts and uncles in Belgium. Many special thanks go to my wife, Jingyi Wu. I am grateful for having you in my life. Thank you for your help and always supporting me unconditionally, encouraging me with your best wishes during my PhD time.

List of Publications

J. Atherton, K. Jiang, M. M. Stangier, **Y. Luo**, S. Hua, K. Houben, J. J. E. van Hooff, A. P. Joseph, G. Scarabelli, B. J. Grant, A. J. Roberts, M. Topf, M. O. Steinmetz, M. Baldus, C. A. Moores, A. Akhmanova. A structural model for microtubule minus-end recognition and protection by CAMSAP proteins. *Nature Structural and Molecular Biology* 2017, *24*, 931-943.

J. Atherton, **Y. Luo**, S. Xiang, C. Yang, K. Jiang, M. M. Stangier, A. Vemu, A. Cook, S. Wang, A. Roll-Mecak, M. O. Steinmetz, A. Akhmanova, M. Baldus, C. A. Moores. Structural determinants of microtubule minus end preference in CAMSAP CKK domains. *Under revision*.

R. Damman, S. Schütz, **Y. Luo**, M. Weingarth, R. Sprangers, M. Baldus. Atomic-level insight into mRNA processing bodies by combining solid and solution-state NMR spectroscopy. *Nature Communications* 2019. *Accepted*.

Y. Luo, S. Xiang, P. J. Hooikaas, L. van Bezouwen, J. A. S., C. Janke, F. Förster, A. Akhmanova, M. Baldus. Direct observation of dynamic protein interactions involving human microtubules using solid-state NMR spectroscopy. *Submitted*.

Curriculum Vitae

Yanzhang Luo was born October 30, 1990 in Guangzhou, China. He did his Bachelor in Bioengineering at South China University of Technology, Guangzhou, China. Afterwards he went to Utrecht, the Netherlands in 2013, to study his Master in Molecular and Cellular Sciences. At Utrecht University, he worked in the group of Dr. Paul van Bergen en Henegouwen on nanobodies targeting human complement decay-accelerating factor. Afterwards he went to the solid-state NMR group of Prof. Dr. Marc Baldus to start a structural study on interactions of microtubules and microtubule-associated proteins. In 2015, he started his PhD in the same group at the Bijvoet Center for Biomolecular Research at Utrecht University, where he continued the same study and developed methods to obtain isotope-labeled human microtubules and study the structural as well as dynamics changes of microtubules and microtubule-associated proteins in their interactions. The work of his PhD is described in this thesis.

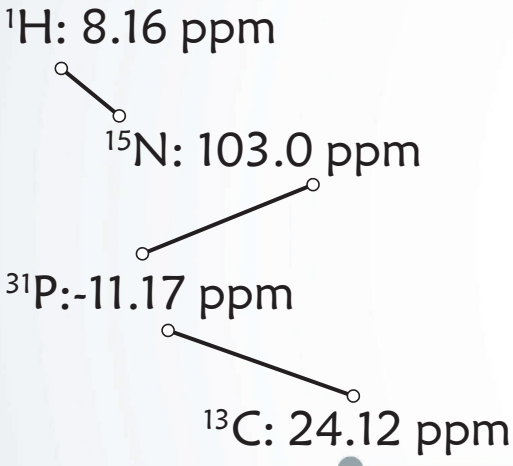
^{1}H: 8.16 ppm
^{15}N: 103.0 ppm
^{31}P:-11.17 ppm
^{13}C: 24.12 ppm